GRAIN REFINEMENT OF MAGNESIUM ALLOY AZ91E

by

Amit Azad

A THESIS SUBMITTED IN PARTIAL FULFILLMENT OF
THE REQUIREMENTS FOR THE DEGREE OF

MASTER OF APPLIED SCIENCE

in

The College of Graduate Studies

(Mechanical Engineering)

THE UNIVERSITY OF BRITISH COLUMBIA
(Okanagan)

April 2012

Abstract

Spark Plasma Sintering (SPS) process has been used to develop a novel grain refiner Al-SiC master alloy for AZ91E Mg alloys. When the Al-SiC master alloy was added to molten AZ91E alloy, the Al matrix melted and allowed the SiC particles to distribute homogeneously throughout the molten AZ91E alloy. After addition of 0.1 wt.% Al-SiC master alloy to AZ91E alloy, the mean grain size decreased from 227.5 ± 5.0 µm to 197.5 ± 5.0 µm; however, the mean grain size increased when the amount of added Al-SiC exceeded 0.1 wt.%. The grain refining and coarsening mechanisms were investigated using scanning electron microscope (SEM), energy dispersive spectroscopy (XEDS) and differential scanning calorimetry (DSC).

It is proposed that the binary carbides (e.g., MgC), possibly acted as heterogeneous nucleation sites for grain refinement. The formation of ineffective nuclei $AlCMn_3$ with the increased amount of grain refiner exceeding 0.1 wt.% Al-SiC has inhibited formation of MgC, resulting in grain coarsening. The effect of Al-SiC on the mean area percentage of β-$Mg_{17}Al_{12}$ phase and porosity were investigated using optical microscopy, while hardness was measured using a Rockwell hardness tester. It was found that increasing the addition of Al-SiC had an effect on β-phase and porosity. The highest mean area percentage of β-phase was found 6.6 ± 1.3 % with the addition of 1 wt.% Al-SiC, while the lowest mean area percentage of porosity was 1.9 ± 0.5 % with the addition of 0.1wt.% Al-SiC. It was found that adding the Al-SiC master alloy to AZ91E alloy had no influence on hardness.

Table of Contents

Abstract ..... **ii**

Table of Contents ..... **iii**

List of Tables ..... **vi**

List of Figures ..... **viii**

Acknowledgements ..... **xi**

Dedication ..... **xii**

1 Introduction **1**

2 Literature Review **4**

2.1 History of magnesium production 4

2.2 Properties of magnesium 5

2.3 Advantages of magnesium and magnesium alloys 6

2.4 Disadvantages of magnesium and magnesium alloys 8

2.5 Typical applications of magnesium alloys 9

2.6 Alloying of magnesium 11

2.6.1 Effect of alloying constituents 11

2.6.2 Properties of AZ91E magnesium alloy 18

2.7 Gravity permanent mold casting process 19

2.8 Grain refinement of magnesium alloys 20

2.8.1 Mechanisms of grain growth 21

2.8.1.1 Nucleation 21

2.8.1.1.1 Homogeneous nucleation 22

2.8.1.1.2 Heterogeneous nucleation 25
2.8.1.1.3 Constitutional undercooling 27
2.8.1.2 Growth restriction 29
2.8.2 Grain refinement methods 31
2.8.2.1 Carbon inoculation 33
2.8.2.2 Adding other additives 40
2.9 Spark plasma sintering technique 41
3 Experimental Procedure 43
3.1 Preparation of Al-SiC master alloy 43
3.2 Grain refinement of AZ91E magnesium alloy 44
3.3 Metallography sample preparation 45
3.4 Optical microscopy 47
3.5 Scanning electron microscope and energy dispersive spectroscopy 51
3.6 Rockwell hardness testing 51
3.7 Differential scanning calorimetry 51
3.8 Possible sources of error 53
4 Results and Discussion 54
4.1 Effect of Al-SiC master alloy on the structure of AZ91E alloy 54
4.1.1 Effect of Al-SiC on average grain size 54
4.1.2 Effect of Al-SiC on β-$Mg_{17}Al_{12}$ phase 56
4.1.3 Effect of Al-SiC on hardness 59
4.1.4 Effect of Al-SiC on porosity 60
4.1.5 Effect of Al-SiC on solidus and liquidus temperature and enthalpy of liquidus reaction 62
4.2 Microstructure analysis of Al-SiC master alloy and grain refined alloys 66
4.2.1 Microstructure of Al-SiC master alloy 66

4.2.2 Microstructure of grain-refined AZ91E alloys 68
4.2.3 Grain refinement mechanisms 72
4.2.3.1 Heterogeneous nucleation 72
4.2.3.2 Growth restriction effect 79
4.2.4 Grain coarsening mechanism 82

5 Conclusions 85

5.1 Future work 86

Bibliography 87

Appendices 93

Appendix A: Paired t-test on mean grain size 93

Appendix B: Single factor ANOVA on mean grain size 95

Appendix C: Paired t-test on mean area percentage of β-phase 96

Appendix D: Single factor ANOVA on mean area percentage of β-phase 98

Appendix E: Paired t-test on mean area percentage of porosity 99

Appendix F: Single factor ANOVA on mean area percentage of porosity 101

List of Tables

Table 1: Typical mechanical properties of magnesium at 20 °C 5
Table 2: Physical and mechanical properties of Mg alloys and other structural materials at room temperature 6
Table 3: Machinability of structural materials 8
Table 4: Standard electron potential of elements 9
Table 5: Chemical composition (wt.%) of AZ91E alloy 18
Table 6: Room-temperature mechanical properties of AZ91E alloy castings 18
Table 7: Slope of the liquidus line, partition coefficient and growth restriction parameter for various alloying elements in magnesium 30
Table 8: Summary of grain refiners and grain refinement mechanisms for Mg and Mg alloys 32
Table 9: Summary of carbon inoculation techniques 34
Table 10: Chemical composition of AZ91E alloy used in this research 44
Table 11: Metallographic etchants for AZ91E alloy 47
Table 12: Microscope set-up for analysis 47
Table 13: Number of grains measured for casting trial 1 and trial 2 48
Table 14: Possible source of error and error value 53
Table 15: Mean grain size of grain refined alloys 54
Table 16: Mean area percentage of β-$Mg_{17}Al_{12}$ phase of grain refined alloys 57
Table 17: Mean area percentage of interdendritic porosity of grain refined alloys 61
Table 18: Solidus and liquidus temperatures and enthalpy of liquidus reaction of selected alloys 63
Table 19: XEDS analysis of Al-SiC master alloy 67
Table 20: XEDS analysis of features in Figure 39 71
Table 21: XEDS analysis of features in Figure 41 73
Table 22: XEDS analysis of features in Figure 42 74
Table 23: XEDS analysis of features in Figure 46 76
Table 24: Reduced chemical composition of particles in Figure 41 83

Table 25: Reduced chemical composition of particles in Figure 42 83
Table 26: XEDS analysis of features in Figure 50 84
Table 27: Paired *t*-test of AZ91E alloy without Al-SiC 93
Table 28: Paired *t*-test of AZ91E + 0.1 wt.% Al-SiC 93
Table 29: Paired *t*-test of AZ91E + 0.2 wt.% Al-SiC 94
Table 30: Paired *t*-test of AZ91E + 0.5 wt.% Al-SiC 94
Table 31: Paired *t*-test of AZ91E + 1 wt.% Al-SiC 94
Table 32: Single factor ANOVA on mean grain size 95
Table 33: Paired $\boldsymbol{t}$ -test on mean area percentage of $\boldsymbol{\beta}$-phase of base alloy 96
Table 34: Paired $\boldsymbol{t}$ -test on mean area percentage of $\boldsymbol{\beta}$-phase of AZ91E + 0.1 wt.% Al-SiC 96
Table 35: Paired $\boldsymbol{t}$ -test on mean area percentage of $\boldsymbol{\beta}$-phase of AZ91E + 0.2 wt.% Al-SiC 96
Table 36: Paired $\boldsymbol{t}$ -test on mean area percentage of $\boldsymbol{\beta}$-phase of AZ91E + 0.5 wt.% Al-SiC 97
Table 37: Paired $\boldsymbol{t}$ -test on mean area percentage of $\boldsymbol{\beta}$-phase of AZ91E + 1 wt.% Al-SiC 97
Table 38: Single factor ANOVA on mean area percentage of $\boldsymbol{\beta}$-phase 98
Table 39: Paired *t*-test on mean area percentage of porosity of base alloy 99
Table 40: Paired *t*-test on mean area percentage of porosity of AZ91E + 0.1 wt.% Al-SiC 99
Table 41: Paired *t*-test on mean area percentage of porosity of AZ91E + 0.2 wt.% Al-SiC 99
Table 42: Paired *t*-test on mean area percentage of porosity of AZ91E + 0.5 wt.% Al-SiC 100
Table 43: Paired *t*-test on mean area percentage of porosity of AZ91E + 1 wt.% Al-SiC 100
Table 44: Single factor ANOVA on mean area percentage of porosity 101

List of Figures

Figure 1: Fuel economy as a function of automobile weight 10
Figure 2: Mg-Al equilibrium phase diagram 12
Figure 3: Effect of Al addition on the grain size of pure Mg 13
Figure 4: Micrographs of pure Mg and Mg –Al alloys 14
Figure 5: Effect of Si addition on the grain size of pure Mg 16
Figure 6: Optical micrograph of pure Mg with the addition of 0.07, 0.15 and 0.5 wt.% Si 16
Figure 7: Gravity permanent mould casting process 19
Figure 8: Schematic of a homogeneous nucleation 22
Figure 9: Surface, volume and net energies change with particle (nucleus) radius 24
Figure 10: Schematic of heterogeneous nucleation 26
Figure 11: Binary equilibrium phase diagram when $\boldsymbol{Ko} < 1$ 27
Figure 12: Solute concentration and equilibrium freezing temperature profile ahead of a solid-liquid interface 28
Figure 13: Constitutional undercooling 29
Figure 14: Grain structure of as-cast AZ63 alloy with Al_4C_3-SiC/Al master alloy: a) Base alloy; b) 0.5 wt. % Al_4C_3-SiC/Al; c) 1 wt. % Al_4C_3-SiC/Al 38
Figure 15: Grain structure of as-cast Mg-3 wt. % alloy with Al-SiC master alloy: a) Base alloy; b) 0.3 wt.% Al-SiC; c) 10 wt. % Al-SiC 40
Figure 16: Schematic of a spark plasma sintering machine 41
Figure 17: Current flow through powder particles 42
Figure 18: Optical micrograph of a SPS processed Al-SiC master alloy 43
Figure 19: Dimensions of as-cast specimens 46
Figure 20: Example of grain size measurement in AZ91E alloy: a) Without Al-SiC; b) 0.1 wt.% Al-SiC; c) 0.2 wt.% Al-SiC; d) 0.5 wt.% Al-SiC; e) 1 wt.% Al-SiC 49
Figure 21: Sample regions for grain size and hardness measurements 49
Figure 22: Optical micrograph: a) Intermetallic compound ($Mg_{17}Al_{12}$); b) routine analysis for measurement of area percentage of $Mg_{17}Al_{12}$ 50

Figure 23: Optical micrograph: a) Porosity; b) routine analysis for area percentage of porosity 50
Figure 24: A screen shot from "NETZSCH Proteus Thermal Analysis" software 52
Figure 25: Final mean grain size of AZ91E alloy at various wt.% of Al-SiC 55
Figure 26: As-cast grain structure of AZ91E alloys after 4 min etching: a) Without Al- SiC; b) 0.1 wt.% Al-SiC; c) 0.2 wt.% Al-SiC; d) 0.5 wt.% Al-SiC; e) 1 wt.% Al-SiC. The diameter of each sample is 3.4 cm. 55
Figure 27: $\boldsymbol{\beta}$-$Mg_{17}Al_{12}$ phase in AZ91E alloy with 1 wt.% Al-SiC 57
Figure 28: Final mean area percentage of $\boldsymbol{\beta}$-$Mg_{17}Al_{12}$ phase for the studied alloy composition 58
Figure 29: Average hardness of grain refined alloys 59
Figure 30: Interdendritc porosity AZ91E alloys: a) Without Al- SiC; b) 0.1 wt.% Al-SiC; c) 0.2 wt.% Al-SiC 60
Figure 31: Mean area percentage of interdendritic porosity in AZ91E alloy and grain refined alloys 61
Figure 32: Fraction of solid versus temperature 64
Figure 33: DSC curve of AZ91E alloy with the addition of 0.1 wt.% Al-SiC 65
Figure 34: DSC curve of AZ91E alloy with the addition of 1 wt.% Al-SiC 66
Figure 35: Microstructure of Al-SiC master alloy 67
Figure 36: Si-C equilibrium binary phase diagram 68
Figure 37: X-ray maps for grain refined (AZ91E+ 0.1 wt.% Al-SiC alloy): a) SEM image; b) Mg; c)Al; d) Si; e) Al; f) Zn 69
Figure 38: General microstructure of each alloy composition: a) Without Al-SiC; b) 0.1 wt.% Al-SiC; c) 0.2 wt.% Al-SiC; d) 0.5 wt.% Al-SiC; e) 1 wt.% Al-SiC 70
Figure 39: SE image of interdendritic region of AZ91E alloy with 0.1 wt.% Al-SiC 71
Figure 40: Optical micrograph of interdendritic region of AZ91E alloy with 0.1 wt.% Al-SiC 72
Figure 41: Microstructure of AZ91E alloy with 0.1wt.% Al-SiC for location A 73
Figure 42: Microstructure of AZ91E alloy with 0.1wt.% Al-SiC for location B 74
Figure 43: Al-Mn binary phase diagram 75

Figure 44: Microstructure of AZ91E alloy with 0.1wt.% Al-SiC, showing heterogeneous nuclei substrates 76
Figure 45: Mg-C binary phase diagram 77
Figure 46: MgC (particle 1- Figure 44) at higher magnification 78
Figure 47: XEDS line scan for AZ91E alloy with 0.1 wt.% Al-SiC 80
Figure 48: XEDS line scan, showing the comparison of Al and Mg concentration along the line AB 81
Figure 49: Al-Mn-C ternary phase diagram 82
Figure 50: Microstructure of AZ91E alloy with 1 wt.% Al-SiC 84

Acknowledgements

I offer my deepest gratitude to my supervisor, Dr. Lukas Bichler, for his most appreciated supervision, guidance and helping me to follow the right path for my research work when even I didn't know where the path was.

I would like to thank Dr. Comondore Ravindran and Mr. Abdallah Elsayed for their contribution in casting experiment at Ryerson University. I would also like to thank Dr. Mathieu Brochu for preparing the grain refiner Al-SiC master alloy using spark plasma sintering technique at McGill University.

I would like to express my enduring gratitude to my research committee members, Dr. Ray Taheri and Dr. Vladan Prodanovic, for their penetrating questions and guideline to reach the answer for those questions. Thank you Dr. Andre Phillion for valuable suggestion for using differential scanning calorimety. Thank you Mr. Alex Willer and Mr. David Arkinstall for great assistance in the machine shop and SEM Lab respectively.

Finally, I would like to express my personal thanks to my dear parents and my wife for their understanding, passion and love.

To my parents.

1 Introduction

This chapter provides an overview of the application of magnesium alloys in automotive and aerospace industries, followed by a discussion of the grain refinement techniques of magnesium alloys.

For the last 20 years, automotive and aerospace manufacturers have been seeking to reduce vehicle weight in order to increase fuel efficiency and reduce green house gas emissions. As a result, designers consider magnesium alloys to cast structural components due to its low density (1.738 g/cm^3) and its resulting high specific strength, which allows magnesium based alloys to replace denser materials like cast iron (7.87 g/cm^3), copper (8.94 g/cm^3) and aluminum (2.70 g/cm^3). Due to good castability, good ductility and moderately high strength at temperatures up to approximately 120 °C, the Aluminum-Magnesium based alloys represent a majority of commercial alloys [1]. For example: wheels, valve and cam covers, accessory drive brackets, clutch housings and steering column, to name just a few [2]. Of the Al-Mg based alloys, the AZ91E alloy has become important, because of its excellent corrosion resistance. In AZ91E alloy, harmful impurities for corrosion such as iron, nickel and copper are controlled to very low levels [3]. Thus, AZ91E alloy was successfully used at room temperature and in low pressure applications [4]. Further improvement of mechanical properties (e.g., yield strength and hardness), chemical properties (e.g., corrosion resistance) and manufacturing properties (e.g., hot tearing susceptibility) can be achieved and controlled by grain refinement [5,6,7,8]. Clearly, successful grain refinement of AZ91E alloy has a very significant industrial impact. However, grain refinement of AZ91E alloy has not been achieved successfully yet.

Grain refinement of cast magnesium alloys can be achieved by two methods: i) increasing the cooling rate during solidification [9] and ii) adding chemical grain refiner into molten alloy during casting [9]. In this research, the cooling rates were maintained constant, and only the effect of adding a chemical grain refiner was investigated. In the past, minor addition of solutes (e.g., Al, Si, Sr, Ca) and carbon inoculation were the most commonly used chemical grain refinement methods [10,11,12]. In the carbon innoculation method, carbon was added to the

molten magnesium in the form of graphite, carbon powder, carbonaceous gases and a wide range of carbon containing agents such as hexachlorobenzene, hexachloroethane [10,13,14] silicon carbide (SiC) [15], aluminum carbide (Al_4C_3) [16] and master alloys such as Al_4C_3-SiC/Al [17] and Al-SiC [18]. Due to some practical advantages, such as addition of grain refiners at lower melt temperature, less fading for long holding time and refinement of large melt volume, the carbon inoculation method has become major industrial grain refining technique [10,11]. Although several investigations have been carried out to achieve grain refinement in magnesium alloys, the grain refinement mechanisms are not yet fully understood.

In the current research, Al-SiC master alloy was studied as a potential chemical grain refiner for AZ91E magnesium alloy. The main objectives of this research were to determine the optimal addition level of the grain refiner to achieve maximum grain refinement effect and to indentify the grain refinement mechanism.

A novel master alloy of Al-SiC (50 wt.% Al and 50 wt.% SiC) was prepared and added as a chemical grain refiner to molten AZ91E magnesium alloy at four different weight fractions: 0.1, 0.2, 0.5 and 1 wt.%. The mean grain size, mean area percentage of β-$Mg_{17}Al_{12}$ phase and mean area percentage of porosity of the resulting alloys was measured using optical microscope. The lowest mean grain size was found to be 197.5 ± 5.0 μm with the addition of 0.1 wt.% Al-SiC. Further increase of the grain refiner amount inhibited the grain refinement process and the mean grain size increased to 360.9 ± 10.6 μm with the addition of 0.2 wt.% Al-SiC. The highest mean area percentage of β-$Mg_{17}Al_{12}$ phase was found to be 6.6 ± 1.3 % with the addition of 1 wt.% Al-SiC. The lowest mean area percentage of porosity was found 1.9 ± 0.5 % with the addition of 0.1 wt.% Al-SiC. It was also found that the Al-SiC additions had no influence on the alloy hardness.

SEM and XEDS analyses were carried on the grain refined alloys to indentify the mechanisms of grain refinement and coarsening of AZ91E alloy treated with Al-SiC. Two possible mechanisms were identified. First, magnesium carbide (MgC) intermetallic compound possibly acted as heterogeneous nucleation site. Second, microsegregration of aluminum was promoted, which enabled the growth restriction effect. In the case of high wt.% additions (> 0.1 wt.% Al-SiC), a

direct reaction of C, Al and Mn or C and Al-Mn particles possibly formed $AlCMn_3$ intermetallic compounds. Formation of $AlCMn_3$ reduced the probability to form MgC. Since the $AlCMn_3$ intermetallic compound was ineffective nuclei site for α-Mg due to its face centered cubic crystal structure, grain coarsening occurred.

A differential scanning calorimetry (DSC) analysis was carried out on the selected grain refined alloys to identify the effect of grain refiner on solidus and liquidus temperatures, fraction of solid development and to verify the mechanism found in SEM-XEDS analysis for grain refinement and grain coarsening. The average solidus temperatures were found to be 428.5 and 430.6 °C and the average liquidus temperatures were found to be 589.3 and 589.6 °C with the addition of 0.1 and 1 wt% Al-SiC, respectively. The enthalpy of liquidus reaction was found 317.2 J/g with the addition of 0.1 wt.% Al-SiC. This enthalpy was decreased to 204.9 J/g with the addition of 1 wt.% Al-SiC. Higher enthalpy of liquidus reaction indicated that a greater number of grains formed from heterogeneous nucleation during solidification with the addition of 0.1 wt.% Al-SiC.

2 Literature Review

In this chapter, a brief discussion on magnesium extraction, atomic, physical and mechanical properties, advantages and disadvantages of pure magnesium and its alloys, typical applications, alloying elements and their effect will be discussed. Then, the overview of casting methods for Mg alloys, grain refinement techniques, alloy nucleation and solidification and the results of published research on chemical grain refinement of magnesium alloys will be presented.

2.1 History of magnesium production

Magnesium was first isolated by the British scientist Sir Humphrey Davy by decomposing wet magnesium sulphate using an electrolytic voltaic cell. In 1828 Antoine Alexandre Brutun Bussy isolated the metal by fusing dehydrated magnesium chloride with potassium at elevated temperatures. In 1868, magnesium was used as powder or ribbon for flashlights and as a reducing agent in the production of aluminum [19].

Worldwide magnesium production was only 10 tonnes per annum by 1900. As the demand for magnesium had increased in military, aerospace and automobile industries, the production had climbed to 32,000 tonnes per annum by 1939. Total production in western world has reached 250,000 tonnes per annum by 1990 [3]. Magnesium production had reached to 810,000 tonnes per annum in the year 2010 [20].

Magnesium can be produced from six different sources: magnesite ($MgCO_3$), dolomite ($MgCO_3.CaCO_3$), bischofite ($MgCl_2.6H_2O$), carnallite ($MgCl_2.KCl.6H_2O$), serpentine ($3MgO.2SiO_2.2H_2O$) and sea water ($Mg^{2+}_{(aq)}$) which contains 0.13% of magnesium [3]. The carbonates dolomite ($MgCO_3.CaCO_3$) and magnesite ($MgCO_3$) are the most common ores. The natural brines from Great Salt lake and the Dead Sea are the sources for the double chloride carnellite ($MgCl_2.\ KCl.\ 6H_2O$).

There are two methods for magnesium production: i) electrolysis of molten magnesium chloride and ii) thermal reduction of magnesium oxide. The major production of magnesium is done by the "Pidgeon Process", which is a thermal reduction method [3,10]. The Pidgeon process was developed by L. M. Pidgeon in 1941, where dolomite ore is used as the source of Mg, while ferrosilicon is used as a reducing agent. In this process, magnesium evolves as vapour and then is distilled in a water cooled container [19].

2.2 Properties of magnesium

Magnesium is found in Group 2 of the periodic table of elements as an alkaline earth metal. Under atmospheric pressure, the crystal structure of pure magnesium is hexagonal close packed. At room temperature, the lattice parameters of pure magnesium are: a = 0.32092 nm and c = 0.52105 nm [3]. The c/a ratio for magnesium is 1.6236. As shown in Table 1, mechanical properties of magnesium vary with production technique such as casting, extrusion and forging.

Table 1: Typical mechanical properties of magnesium at 20 °C [21]

Production technique	Tensile strength, MPa	0.2 % tensile yield strength, MPa	0.2% compressive yield stress, MPa	Elongation in 50 mm (2 in)%	Rockwell hardness HRE
Sand cast	90	21	21	2-6	16
Extrusion	165-205	69-105	34-55	5-8	26
Hard rolled sheet	180-220	115-140	105-115	2-10	48-54

2.3 Advantages of magnesium and magnesium alloys

The advantages of magnesium and magnesium alloys are discussed in the following text:

i. Density and specific strength

Presently, the main concern of automotive and aerospace industries is to increase the fuel efficiency of automobiles and aircrafts. The fuel efficiency can be increased by decreasing the weight of vehicles. Because of the low density (1.738 g/cm^3), high specific strength (175.69 MPa/g/cm^3) and high tensile strength of cast Mg alloys, they are important material in these industries. Table 2 provides a comparison of Mg alloys with other structural materials.

Table 2: Physical and mechanical properties of Mg alloys and other structural materials at room temperature [22,3]

As-cast alloy	Density, g/cm^3	Tensile strength, MPa	Specific strength, MPa/g/cm^3	Modulus of elasticity, MPa
Copper alloy C 93200	8.93	240	27	100
Cast iron grade 1800	7.30	124	17	66
Aluminum alloy 356	2.69	164	61	72
Magnesium alloy AZ91E	1.81	318	176	45

ii. Castability

Castability implies ease of producing a casting, minimising cost, defects and lead-time. Magnesium has a good castability [23,26]. A magnesium alloy can be easily cast with a relatively low tooling cost and energy due to the alloy's high fluidity. Magnesium alloys are suitable for casting due to following advantages [3]:

- Casting of thin walled parts (2 mm) is possible, because of the high fluidity of most magnesium alloys.
- Magnesium castings experience high cooling rate due to Mg's low volumetric specific heat compared with aluminum and zinc. Thus, magnesium castings allow faster cycle times.
- High gate pressures can be achieved at moderate ram pressures due to Mg's low density.
- Steel dies used for magnesium alloy casting last two or three times longer than with aluminum alloys because of two factors: i) low solubility of iron in liquid magnesium and ii) less heat per volume of magnesium die-casting alloys.

iii. Damping capacity

The damping capacity of a metal is characterised by the ability to dissipate elastic energy. Because of excellent damping capacity of magnesium and magnesium alloys, they are used to decrease vibration and noise in many applications such as vibration testing fixtures and mounting brackets for electronic equipment [21]. Damping capacity increases with the decrease in grain size of the material, because of the homogenous distribution of elastic energy. According to Sugimoto et al., average alloy grain size should be greater than 10 μm for keeping high damping capacity [24].

iv. Machinability

Magnesium and its alloys have a lower resistance against cutting than other structural metallic materials. Higher speeds and feed rates and greater depths of cut are thus possible and a lower power is required to remove a given amount of Mg in comparison to other commonly machined metals [21]. Table 3 shows the relative power requirements of various metals that are calculated based on the volume of metal removed per minute.

Table 3: Machinability of structural materials [21]

Alloy	Relative Power
Magnesium alloy	1
Aluminum alloy	1.8
Brass	2.3
Cast iron	3.5

2.4 Disadvantages of magnesium and magnesium alloys

As the result of the poor mechanical properties of Mg and Mg alloys at temperatures above 120 °C and relatively poor corrosion resistance of Mg, the uses of Mg and Mg alloys are limited to room temperature applications. Research and development are required to improve these properties. The poor properties of Mg and Mg alloys are discussed in the following text:

i. Pure magnesium is highly corrosive and chemically reactive, because of its lowest standard electrode potential of all the structural metals, as presented in Table 4. Therefore, magnesium acts as an anode in the electrochemical cell when electrically connected with other metal of higher electrode potential (cathode). This property limits the use of magnesium in corrosive environements.

Table 4: Standard electron potential of elements [22]

Elements	Standard potential (Volt)
Au	1.42
Cu	0.34
Pb	-0.126
Sn	-0.136
Ni	-0.25
Co	-0.277
Cd	-0.403
Fe	-0.44
Cr	-0.744
Zn	-0.763
Al	-1.662
Mg	-2.363

ii. The mechanical properties of Mg alloys including modulus of elasticity, strength, hardness, creep resistance of commercial magnesium alloys (Mg-Al-Zn-Mn) decrease at temperature above 120 °C due to the loss of grain boundary strength. This temperature is relatively low compared to other structural materials.

iii. Mg and its alloys have limited cold workability and toughness due to Mg's hexagonal closed packed crystal structure with a limited number of slip systems [23].

2.5 Typical applications of magnesium alloys

Magnesium alloys are used in various structural and non-structural applications. Structural applications include automotive, aeronautic, industrial and office machinery, consumer products, etc. Non-structural applications include alloying with other metals and anodes for cathodic protection, etc. [10]. The structural uses of magnesium alloys are discussed in the following text.

It has been studied that about 27% of Canada's total greenhouse emissions come from the transportation sector [25]. Figure 1 shows that fuel efficiency increases with the decrease of vehicle weight. Light weight and high strength to weight ratio make Mg alloys attractive for automotive and aerospace application.

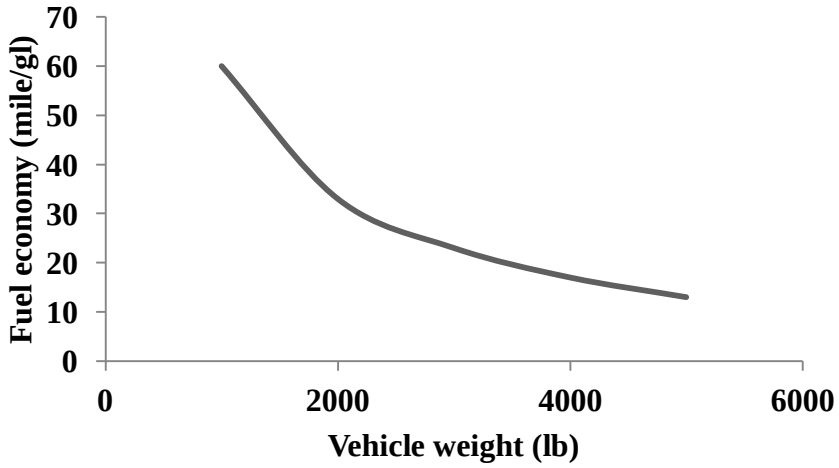

Figure 1: Fuel economy as a function of automobile weight [24]

The most common automotive Mg alloys include: AZ91, AM60, AM50 and AS41. AZ91 is used to make automobile's wheel, clutch pedal, brake pedal, accessory drive bracket, clutch housing, door mirror bracket, headlamp retainer, power window regulator housing, valve and cam covers, oil pan, steering columns [2,26]; AM60 is used for seat frames, upper and lower intake manifolds; AM50 is used for steering wheel armature and AS41 is used to make automatic transmission clutch pistons and stators [26]

In the aerospace industry, Mg alloys are used to cast landing wheel components, diffuser ring, gear box, engine air intake, compressor housing, aircraft starter motor, etc. [3,27]. The most commonly used Mg alloys for aerospace applications include: ZE41, QE22, and WE43 due to their improved corrosion and creep resistance [26].

Magnesium alloys are used in the industrial machinery, such as textile wrap beams and electric-motor end bells. They have also been used in household items, such as sewing machines, and

sporting goods such as archery bow handles, badminton and lawn tennis racquets [3,23]. Due to electromagnetic shielding, magnesium is also used in computer and mobile telephone cases [21].

2.6 Alloying of magnesium

In most structural applications, magnesium is alloyed with other elements. The following observations have been made for general guidelines for alloying [10,28]:

i. Hexagonal close packed metals such as: zinc, cadmium, beryllium, titanium and zirconium form a continuous solid solution with magnesium.
ii. Solid solution formation is possible with elements with atomic size within ± 15% atomic diameter size with respect to magnesium.
iii. As a result of highly electropositive nature of magnesium, less electropositive elements such as those in periods IVb-VIb, as well as carbon and silicon, form intermetallic compounds with magnesium.

2.6.1 Effect of alloying constituents

Molten metal reactivity, castability, grain structure, mechanical properties, chemical properties, physical properties, machinability, formability, weldability etc. of magnesium can be manipulated by adding alloying elements. Effects of some selected elements which are related to the current research are discussed in the following [3, 10]:

Aluminum

Aluminum (Al) refines the as cast grain size of magnesium, because of growth restriction effect caused by constitutional undercooling and micro segregation effect in the interdendritic region as will be discussed in Sections 2.8.1.2 and 2.8.1.3 [11]. Al improves hardness of Mg alloys, because Al forms β- $Mg_{17}Al_{12}$ phase along the grain boundaries. This phase is very hard and brittle [29]. Al also increases corrosion resistance of Mg alloys, because the β phase is cathodic and acts as a barrier to corrosion [7]. Further, Al improves castability, because it

increases the freezing range of Mg alloys thus making the alloy liquid / semi-solid for a longer period of time [3,10].

The maximum solid solubility limit of aluminum for binary magnesium alloy is 12.7 wt. %; however, AZ91 is currently the highest Al containing (9 wt.%) of Mg–Al alloys in commercial applications. The binary Mg-Al equilibrium phase diagram is shown in Figure 2. The Mg-9 wt.% Al alloy system is completely liquid at above 600 °C. As it cools below the liquidus temperature, α-Mg phase begins to form. Further cooling along the vertical line increases the mass fraction α-Mg phase. At 350 °C the vertical line intersects the solvus line. Just above the solvus intersection, the microstructure consists of completely α-Mg phase. Upon crossing the solvus line, the solid solubility of Al in Mg is exceeded, which results in the formation of β-phase particles.

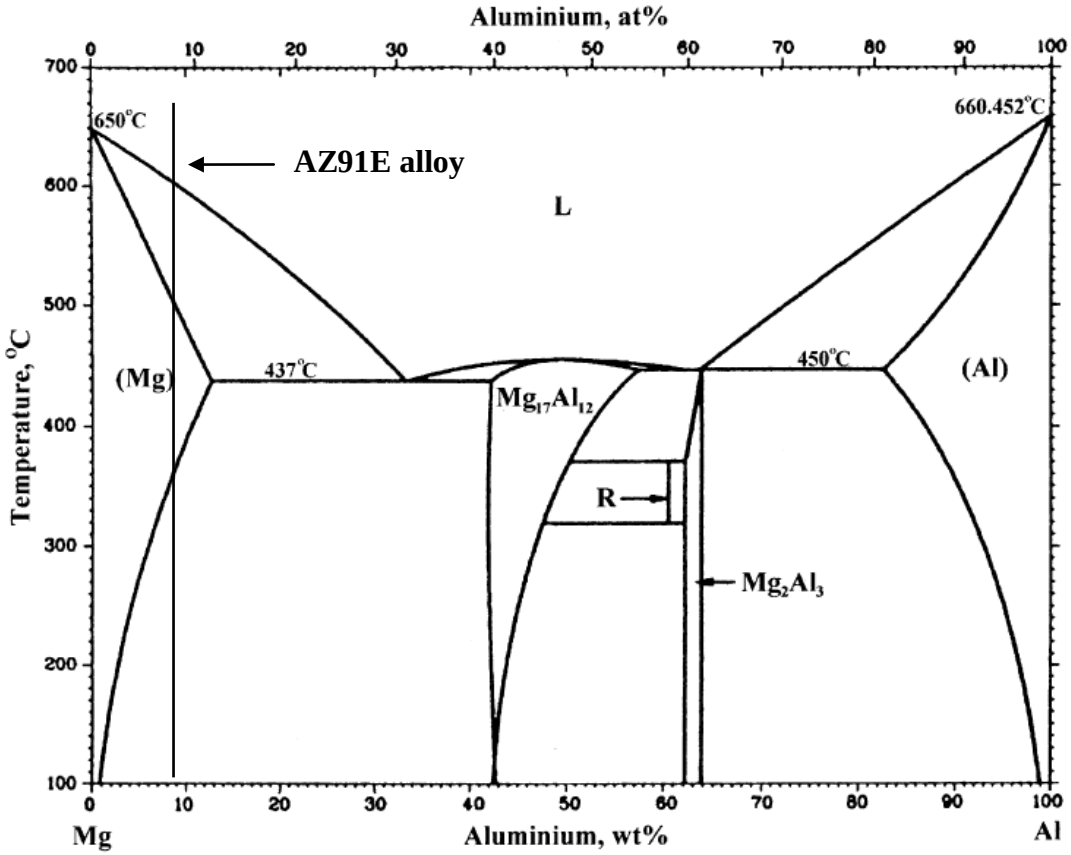

Figure 2: Mg-Al equilibrium phase diagram [30]

During solidification α-Mg dendrites push the solutes (e.g., Al) to the interdentritic region. As a result, the weight fraction of Al increases gradually from the middle of the grain towards the grain boundary. Thus, a very high concentration of solutes is found along the grain boundaries, which promotes the formation of lamellar β-phase

Figure 3 shows that the grain size of magnesium alloy reduces with the increase of aluminum content. This grain refining effect of aluminum continues up to 5wt. % Al. Thereafter, further increase of Al concentration has no effect. Micrographs of pure Mg and Mg-Al alloys are shown in Figure 4.

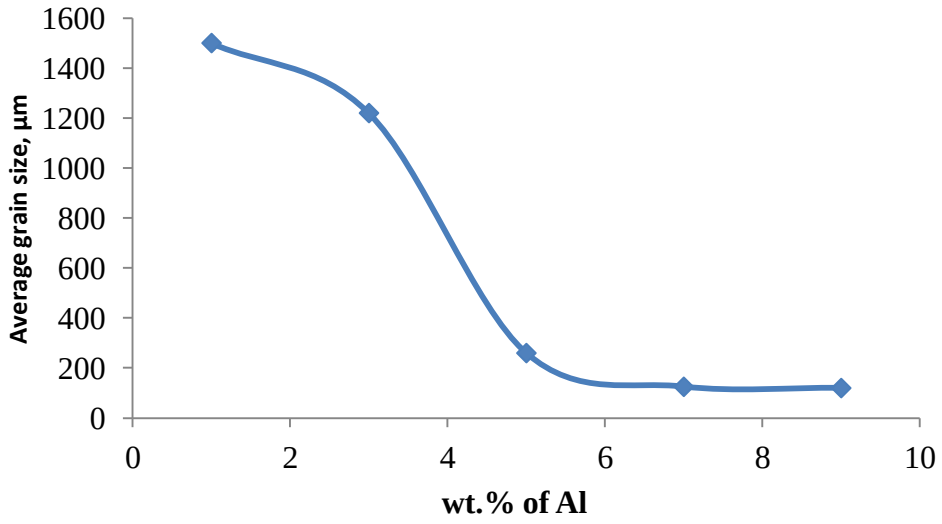

Figure 3: Effect of Al addition on the grain size of pure Mg [11]

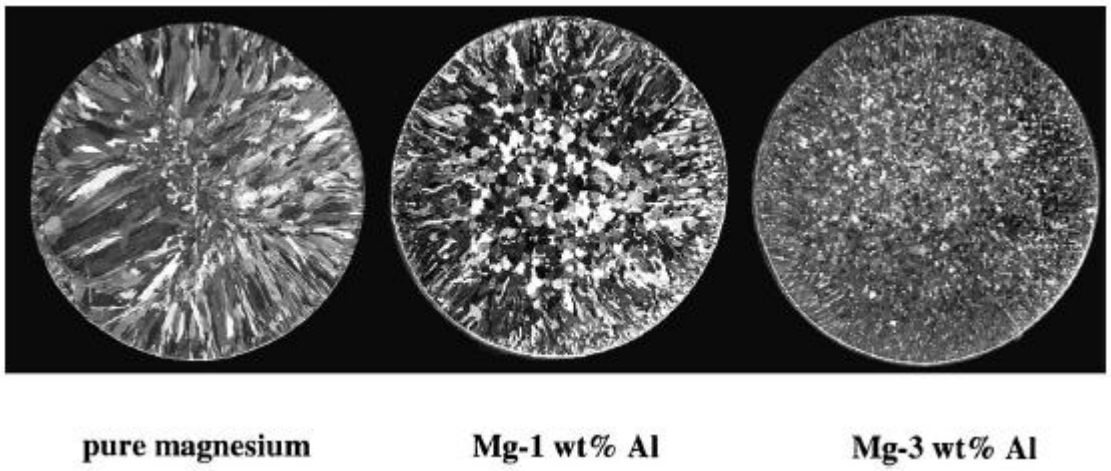

Figure 4: Micrographs of pure Mg and Mg –Al alloys [11]

Copper

According to Mg-Cu binary phase diagram [30], the solubility of Cu is very low (<0.05%) in α-Mg solid solution. Cu improves the high temperature strength of Mg alloys due to precipitation hardening. As shown in Table 4, Cu is more cathodic than Mg and so high additions of copper may accelerate the corrosion of Mg alloys [3,10].

Iron

Iron (Fe) accelerates the corrosion of magnesium by galvanic corrosion. As shown in Table 4, Mg has a greater electronegative potential than Fe. As a result, Mg acts as sacrificial anode when connected with Fe and immersed in electrolyte. The maximum amount of iron that can be present in commercial grade alloys (Mg-Al-Zn-Mn) is 0.01 to 0.03 wt. % [3].

Manganese

Manganese (Mn) increases the tensile strength of Mg alloys, because Mn addition causes grain refinement of magnesium. Due to the increased volume of grain boundaries, dislocation movement is hindered and alloy strength is improved [31].

Mn addition to Mg alloy also transforms harmful impurities such as Fe into relatively harmless intermetallic compounds of Al-Mn-Fe [32]. As a result, it can be said that the Mn improves the corrosion resistance of Mg alloys. The solubility of manganese is relatively low, about 1.5 wt. % for commercial alloys (Mg-Al-Zn-Mn). The solid solubility of manganese is further reduced to 0.3 wt. % in the presence of aluminum [3].

Silicon

The addition of Silicon (Si) to magnesium alloys enables the formation of Mg_2Si phase, which has a high melting point (1085 °C) [33] and high heat of fusion (80 kJ mol^{-1} compared to 8.9 kJ mol^{-1} of Mg). As a result, Si increases the fluidity of magnesium alloys by reducing the solidification rate, due to the latent heat release of Mg-Si phases. Up to 1.5 wt.% Si can be added to Mg alloys. Mg_2Si phase has high hardness (460 HV), high modulus of elasticity (120 GPa), low thermal expansion (7.5 X 10^{-6} K^{-1}) [33] and is very stable, and can thus obstruct grain boundary sliding at elevated temperatures. As a result, addition of Si improves the creep properties of Mg alloys [34].

Silicon is also sometime added to refine the grain structure of magnesium alloys. Figure 5 shows that the grain size of magnesium alloy reduces with the increase of Si content. It can be seen from Figure 6, that a small amount (0.07 wt.%) of silicon addition to pure magnesium has a strong effect on grain refinement. A dramatic reduction on grain size of pure magnesium was observed at 0.15 wt. % Si. The main mechanism to grain refining by silicon is similar to that of aluminum, (i.e., growth restriction effect) due to the increase of constitutional undercooling and microsegregation in the interdendritic regions [11].

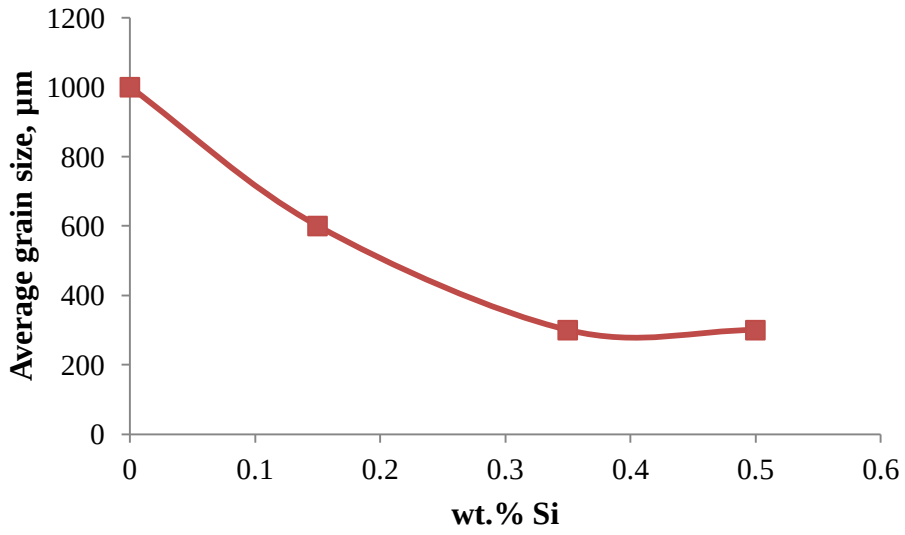

Figure 5: Effect of Si addition on the grain size of pure Mg [11]

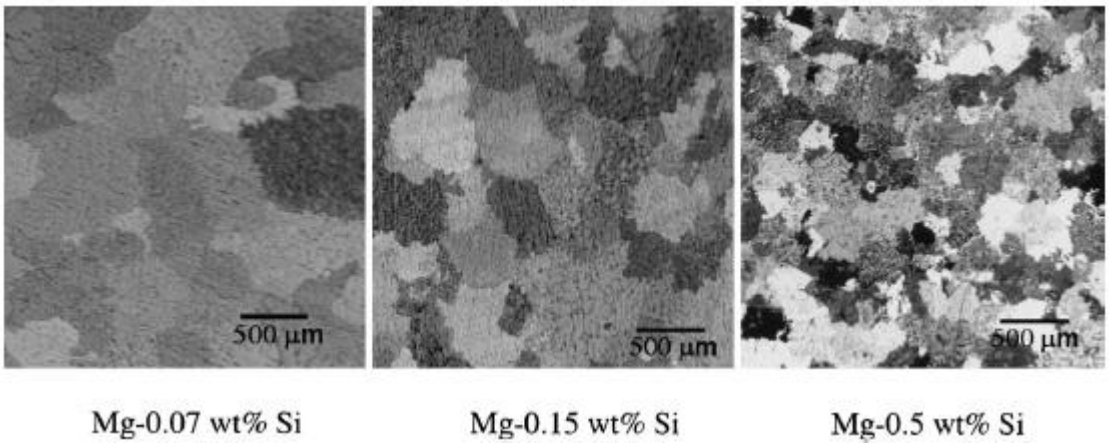

Figure 6: Optical micrograph of pure Mg with the addition of 0.07, 0.15 and 0.5 wt.% Si [11]

Zinc

Zinc (Zn) increases the room temperature strength of Mg-Al alloys, because the solid solubility of Al in Mg decreases with the addition of Zn. Decreasing the solid solubility of Al increases the formation of eutectic β-$Mg_{17}Al_{12}$ phase. This hard and brittle β-phase can act as a barrier for dislocation movement during deformation [35]. Zinc also counteracts the harmful corrosive effect of some impurities such as iron and nickel by increasing the tolerance limit for each impurity [6]. Solid solubility of Zn in Mg alloy is 6.2 wt.% [30]; however, maximum of 1 wt.% Zn is added in commercial Mg-Al-Zn alloys.

Nickel

Mg-Ni binary phase diagram shows that the solid solubility of Ni in Mg is very low (close to zero) [30]. As a result, Ni intermetallics form when Ni is added to Mg. Nickel is more harmful than iron in terms of degrading corrosion properties. As shown in Table 4, Ni (standard electron potential is -0.25) acts as a cathode to the Mg matrix. The average nickel content is 0.01-0.03 wt. % in commercial grade alloys [3].

Commercially used Mg casting alloys include Mg-Al-Zn-Mn (AZ-series), Mg-Al-Mn (AM-series) and Mg-Al-Si-Mn (AS-series). Among these alloy groups, the magnesium sand and permanent mold casting alloys such as AM100A, AZ63A, AZ81A, AZ91C, AZ91E and AZ92A exhibit good castability, good ductility and moderately high yield strength at temperatures up to approximately 120 °C. Of these alloys, AZ91E has superior corrosion resistance as the harmful impurities for corrosion such as the iron, nickel and copper are controlled to very low levels. As a result, AZ91E alloy exhibits excellent saltwater corrosion resistance [21]. The chemical compositions, physical and mechanical properties of AZ91E alloy are discussed in the following section.

2.6.2 Properties of AZ91E magnesium alloy

The density of AZ91E alloy is 1.81 g/cm^3 which is 4.6% greater than the pure Mg (1.73 g/cm^3). Liquidus temperature of AZ91E decreases to 598 °C from 650 °C of pure magnesium due to the addition of 8.1 to 9.3 wt.% of Al (Figure 2). The chemical composition limits of AZ91E alloy are provided in Table 5 and typical room-temperature mechanical properties of AZ91E alloy castings are provided in Table 6.

Table 5: Chemical composition (wt.%) of AZ91E alloy [3, 21]

Al	Zn	Mn	Si	Fe	Cu	Ni	Other	Balance
8.1 to 9.3	0.4 to 1	0.17 to 0.35	0.2 max	0.005 max	0.015 max	0.001 max	0.3	Mg

Table 6: Room-temperature mechanical properties of AZ91E alloy castings [21]

Production technique	**Tensile strength, MPa**	**Tensile yield strength, MPa**	**Compressive yield stress, MPa**	**Elongation in 50 mm %**	**Rockwell hardness HRB**
Sand and permanent mold casting	165	97	97	2.5	66

AZ91E alloy can be used in both sand and permanent mold casting processes; however, gravity permanent mold casting is most frequently used for automotive castings.

2.7 Gravity permanent mold casting process

Excellent surface finish and dimensional accuracy of magnesium alloys can be achieved in gravity permanent mould casting compared with sand castings. In permanent mold casting, the molds are made of cast iron, alloy steel or copper.

The permanent mould casting set-up is schematically illustrated in Figure 7. The molten metal is poured into the cavity of the mould and after solidification of the casting, the two halves of the mold are disassembled to remove the casting. In magnesium casting, the mould is usually pre-heated to 200 to 550 °C before the liquid magnesium is poured. The pre-heating temperature of the mold is an important parameter for controlling the cooling rate of solidification, as the microstructure of casting varies with the cooling rate of solidification [9,36].

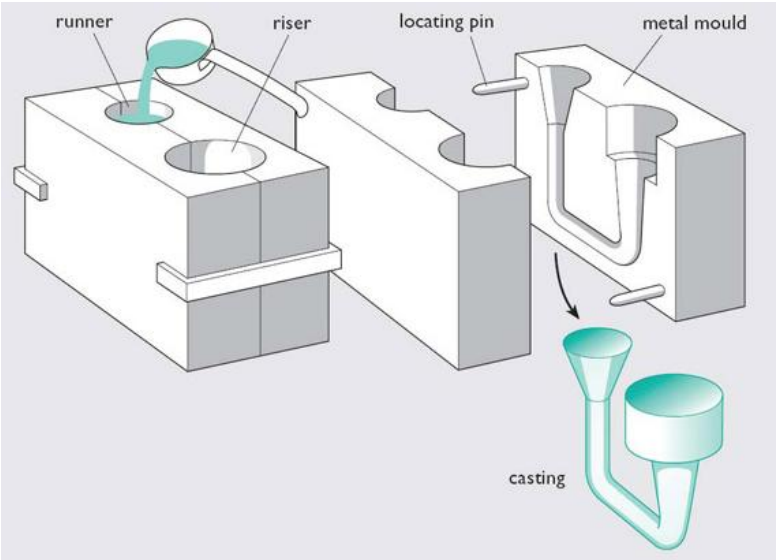

Figure 7: Gravity permanent mould casting process [37]

During solidification, the volume of the casting decreases as the metal density increases, which forces metal to flow from hotter sections that are still in a liquid state to the cooler shrinking sections. After some time the metal can't flow any more to compensate the decreased volume. This moment occurs at "critical solid fraction", where shrinkage porosity readily forms. Risers

are placed in the last areas to solidify. The risers then continue to feed metal into the thicker, slow solidifying sections of the casting [36].

The cooling rate can also be controlled by placing chills in different sections of the casting. It is well established the high cooling rate refines the grain size of the alloy and thus improves the strength and toughness of the casting [9,38]. Cast iron chills are used in magnesium casting to minimize or eliminate formation of shrink porosity in the thinner sections as well as to accelerate solidification in the relatively thicker sections. Chills are often placed in the casting to assist in establishing the desired temperature gradient for directional solidification [10,36].

In this research, graphite permanent molds were used. To avoid a chilling effect by these molds, they were preheated to elevated temperatures, as will be discussed in the Experimental Procedure section of this thesis. However, it is of interest to note, that the cooling rate of the castings prepared in this research was intended to be comparable to the cooling rates experienced in industrial permanent mold or sand casting processes.

2.8 Grain refinement of magnesium alloys

It is well established that grain refinement of polycrystalline materials can improve mechanical properties (e.g., yield strength and hardness [5]), chemical properties (e.g., corrosion resistance of Mg-Al alloys [6, 7]), and improve manufacture ability (e.g., reduce hot tearing susceptibility during casting [39]). However, large grain structure of magnesium alloys are also required in order to improve the creep resistance and use at high (above 150 °C) temperature applications. The mechanisms for methods of manipulating mechanical, chemical and manufacturing properties by refining the grains of magnesium alloys are discussed in the following text.

i. Mechanical properties

According to the Hall-Petch relationship (Equation 1), the yield strength, σ_y, increases with the reduction of average grain size, *d*, (σ_o and k_y are constants for a specific material).

$$\sigma_y = \sigma_o + k_y d^{-1/2} \qquad (1)$$

Since dislocation movement is restricted by grain boundaries, a fine-grained material has greater grain boundary area than one that is coarsely grained. As a result, grain refined materials have greater resistance to plastic deformation and thus have a higher strength [5].

ii. Corrosion resistance

Grain refined Mg-Al alloys have greater corrosion resistance compared to unrefined Mg-Al alloys. β-$Mg_{17}Al_{12}$ phase is precipitated along the grain boundaries during solidification of Mg-Al alloys. Grain refined Mg-Al alloys have greater grain boundary area, which results more β-phase to precipitate along the grain boundary. This β-phase is cathodic and acts as barrier to α-Mg corrosion [6,7].

iii. Manufacturing properties

Hot tears are cracks which form during solidification of alloys. Hot tears can form in any location of a casting due to the non-uniform temperature distribution or complex shape of the casting, which results in undesirable thermo-mechanical and residual stresses. These stresses can be homogenized with fine equiaxed grain structure [39].

In order to understand the grain refinement of Mg alloys it is important to understand the mechanism of grain formation and grain growth.

2.8.1 Mechanisms of grain growth

There are two main mechanisms which control the grain size: nucleation and growth restriction. Manipulation of both mechanisms determines the final grain structure of an alloy [15,40,41]

2.8.1.1 Nucleation

Nucleation is the first step in the transformation of liquid phase to solid phase, upon casting solidification. During this transformation of liquid to solid, a minute solid appears, which can

further grow and form a solid grain. This initial minute solid is known as a nucleus. Each grain grows from its own nucleus. Therefore, the number of nuclei determines the number of grains [9].

There are two types of nucleation processes: homogeneous and heterogeneous. In a homogenous nucleation process, the nucleus arises from the bulk of the liquid. In heterogeneous nucleation, a foreign particle present in the liquid acts as the nucleus [9]. The details of the nucleation processes are discussed next.

2.8.1.1.1 Homogeneous nucleation

The main consideration in homogenous nucleation is the energy involved in forming a minute solid particle from the bulk liquid. The particle begins to form at a temperature, T, which is below the equilibrium freezing temperature, T_E. As illustrated in Figure 8, the homogenous nucleus exhibits a spherical shape of radius, r. This nucleus has the same composition as the bulk liquid. Energies associated with the formation of the spherical nucleus include [9]:

- Net free energy, ΔG_v, required to transform the liquid into solid, and
- Energy to create a surface associated with interfacial energy, $\gamma_{N\text{-}L}$, per unit area of surface.

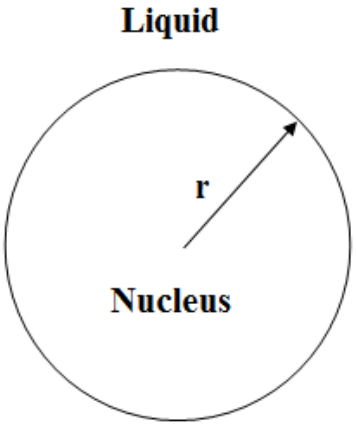

Figure 8: Schematic of a homogeneous nucleation [9]

The net bulk free energy during formation of a spherical nucleus is given by:

$$\Delta G_v = \Delta H - T\Delta S \quad (2)$$

Where,

ΔH= change in enthalpy = latent heat of fusion per unit volume, L_V

ΔS = change in entropy= $\frac{L_v}{T_E}$

Equation 2 can be modified as:

$$\Delta G_v = L_v - T\frac{L_v}{T_E} \quad (3)$$

at $T < T_E$, the value of ΔG_v is negative, which shows the spontaneous transformation of a liquid to a solid.

For the entire sphere the bulk free energy change, ΔG_v, is:

$$\Delta G_v = -\Delta T\frac{L_v}{T_E} \times \frac{4}{3}\pi r^3 \quad (4)$$

Where, $\Delta T = T_E - T$

The surface energy ΔG_S is positive as it receives energy to create a surface. This surface energy can be expressed as:

$$\Delta G_S = 4\pi r^2 \gamma_{N-L} \quad (5)$$

Therefore, the net energy to form spherical particle is the sum of the net bulk free energy, ΔG_v and surface energy ΔG_S:

$$\Delta G_{T(r)} = -\Delta G_v \times \frac{4}{3}\pi r^3 + 4\pi r^2 \gamma_{N-L} \qquad (6)$$

Equation 6 shows the relationship between the total free energy change $\Delta G_{T(r)}$ and particle size, r. As shown in Figure 9, $\Delta G_{T(r)}$ increases positively over a range of small particle size. ΔG_T reaches its maximum positive value at $r = r_c$, which is the critical radius of the nucleus. With further increases in particle size ($r > r_c$), $\Delta G_{T(r)}$ decreases and becomes negative. At $r < r_c$, a positive change occurs in the total free energy. This change causes a thermodynamically unfavourable situation as transformation of liquid to solid is not spontaneous. Particles of a size less than critical radius ($r < r_c$) cannot survive in the melt, while particles larger than the critical radius ($r > r_c$) are able to grow. Therefore, in order to become a stable nucleus for solidification, particles must exceed a critical radius [9,42].

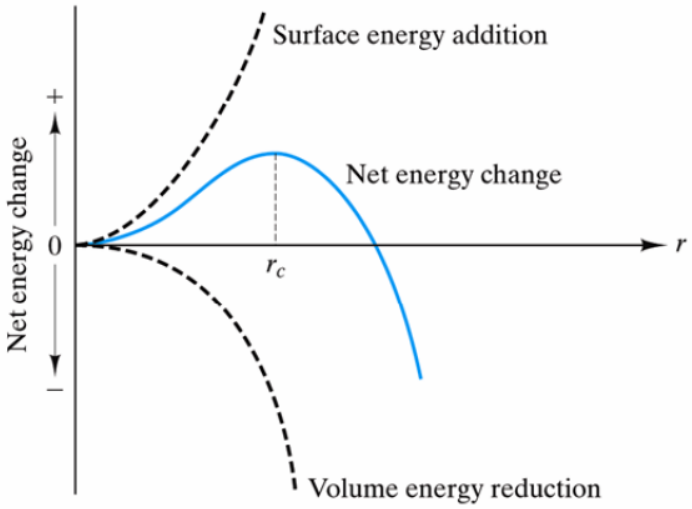

Figure 9: Surface, volume and net energies change with particle (nucleus) radius

The critical radius corresponds to the maximum value of net energy, ΔG_T, in the net energy change vs. particle radius curve (Figure 9). Differentiation on both sites of Equation 6 with respect to r gives the following expression for critical radius, r_c:

$$r_c = \frac{2\gamma_{N-L}T_E}{L_v\Delta T} = \frac{2\gamma_{N-L}}{\Delta G_v} \quad (7)$$

The energy associated for homogeneous nucleation, ΔG^*_{homo}, by substituting r_c in Equation 6 [42]:

$$\Delta G^*_{homo} = \frac{16\pi\gamma^3_{N-L}}{3\Delta G^2_v} \quad (8)$$

2.8.1.1.2 Heterogeneous nucleation

In a heterogeneous nucleation process, preferred sites enable grain nucleation. These sites include mould wall, grain refiners and metal oxide inclusions.

As illustrated in Figure 10, a nucleus of critical radius is formed on the preferential site in the shape of a spherical cap. The number of atoms required to form a spherical cap for heterogeneous nucleation is lower than that of full sphere for homogenous nucleation. Therefore, heterogeneous nucleation is more feasible and more likely to take place than homogenous nucleation. The most effective heterogeneous nucleus is that which has a maximum radius of curvature with a minimum number of atoms. As illustrated in Figure 10, the size of the spherical cap can be described in terms of a contact angle, θ. As expressed in Equation 9, the contact angle is a function of interfacial surface energies (tensions) between nucleus to liquid interfacial energy, $\gamma_{N\text{-}L}$, nucleus to substrate interfacial energy, $\gamma_{N\text{-}S}$, and the liquid to substrate interfacial energy, $\gamma_{L\text{-}S}$ [9].

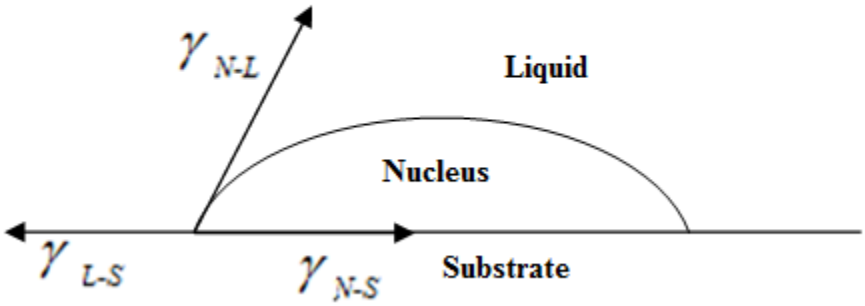

Figure 10: Schematic of heterogeneous nucleation [9]

$$Cos\theta = \frac{\gamma_{L-S} - \gamma_{N-S}}{\gamma_{N-L}} \quad (9)$$

The maximum radius of curvature of a nucleus is formed when $\theta = 0°$, $Cos\ \theta = 1$ and $r = \infty$. This is the most favourable scenario for heterogeneous nucleation. At this condition, the nucleus is completely wetted with the substrate. As θ increases, the nucleus becomes partially wetted with the substrate. When θ becomes 180°, the spherical cap becomes a complete sphere and homogenous nucleation occurs. Complete wetting of the nucleus depends on the relative value of the interfacial energies. When both the substrate and the material to be nucleated have the same crystal structure and lattice parameter, heterogeneous nucleation is most effective [9].

In the case of chemical grain refinement, the inoculant particles introduced into the molten metal must act as heterogeneous nucleation sites [43]. In many cases, very few of the added grain refiner particles actually nucleate a grain, because of their segregation effect and poor surface contact with the parent phase. In order to enhance heterogeneous nucleation, the nucleus size should be large enough so that it becomes stable in the melt. With a large number of nucleating particles, the grain size of the resulting alloy becomes smaller. The heterogeneous nucleation due to constitutional undercooling is discussed in the following section. Constitutional undercooling is often seen as the driving force for grain refinement.

2.8.1.1.3 Constitutional undercooling

The addition of solute to a solvent can either increase or decrease the liquidus temperature of the alloy system. For example in Mg-Al binary phase diagram (Figure 2), the liquidus temperature of the alloy system decreases with the addition of solute, Al.

When an alloy system rejects solute from a solid phase to a liquid phase during solidification, the concentration of solute in the solid, C_S, becomes less than that of liquid, C_L, at any temperature at the solid liquid interface, as shown in Figure 11. The ratio of C_S and C_L is known as the partition coefficient or equilibrium distribution coefficient, K_o, of the solute between the solid and liquid. K_o is less than unity in the case of solute rejection.

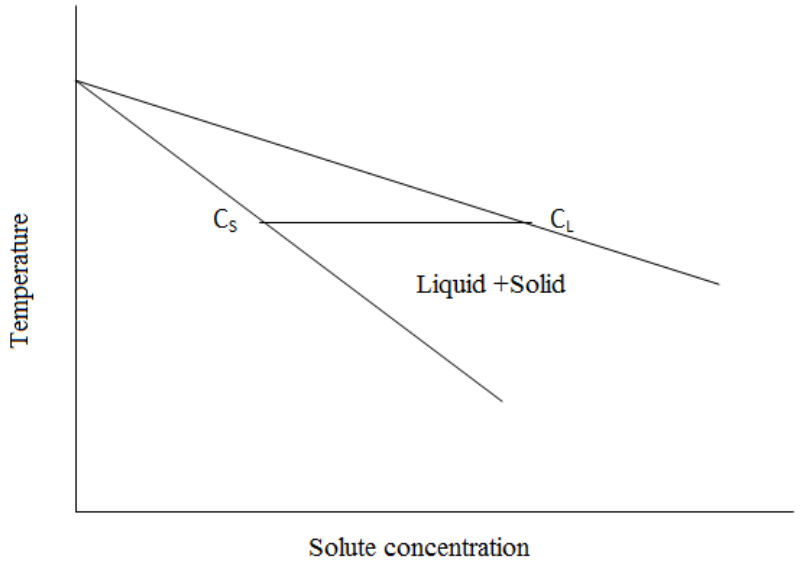

Figure 11: Binary equilibrium phase diagram when $K_o < 1$

Due to solute rejection from the α-phase during freezing, a concentration gradient of solute develops in front of the solid-liquid interface. The concentration of solute becomes highest at the solid liquid interface, which is defined as $\frac{C_o}{k_o}$, where C_o is the overall alloy composition. According to hypoeutectic phase diagram (Figure 11), the equilibrium freezing point decreases with the increase of solute concentration. The relation between solute concentration and equilibrium freezing temperature for a case of K_o<1 is shown in Figure 12. The equilibrium

freezing temperature is lowest at the interface, rising continuously until it reaches the liquidus temperature of the alloy in the bulk liquid. In addition to the distribution of both alloy element concentration and equilibrium freezing temperature, an actual or real positive temperature gradient also exists for a certain distance ahead of the solid-liquid interface. This actual temperature gradient is a function of heat flow, while the gradient of equilibrium freezing temperature depends mainly on the concentration gradient of the solute element. Figure 13 shows a case where K_o <1 (solute is rejected to liquid phase during freezing) in which the liquid, for a certain distance ahead of the interface, is at a temperature lower than the equilibrium freezing temperature. This liquid is undercooled and this phenomenon is known as constitutional undercooling. Constitutional undercooling is a major driving force for heterogeneous nucleation, because nucleants in the melt are more likely to survive and be activated in the constitutionally undercooled zone. The constitutional undercooling may also restrict the grain growth because of slow diffusion of the solute, which limits the rate of grain growth [9].

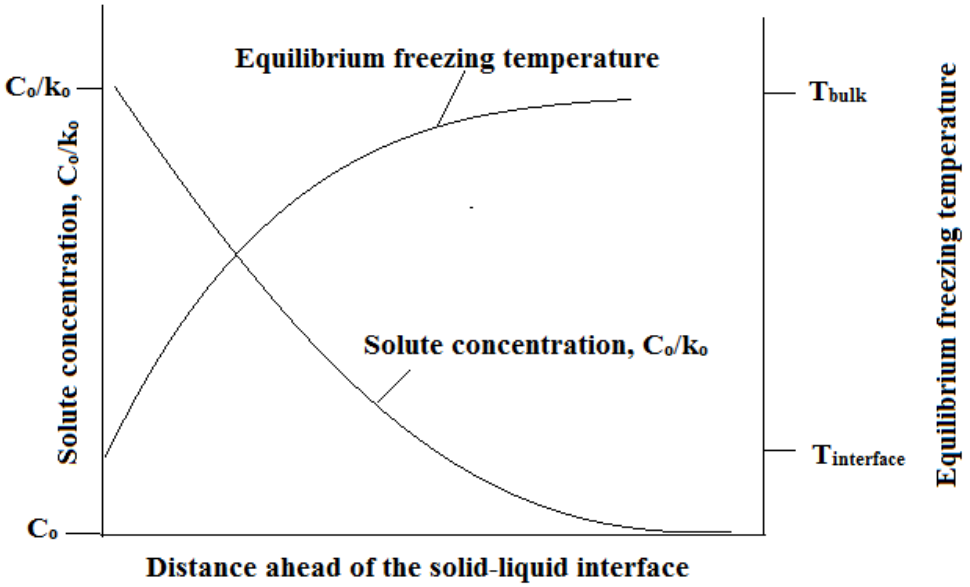

Figure 12: Solute concentration and equilibrium freezing temperature profile ahead of a solid-liquid interface

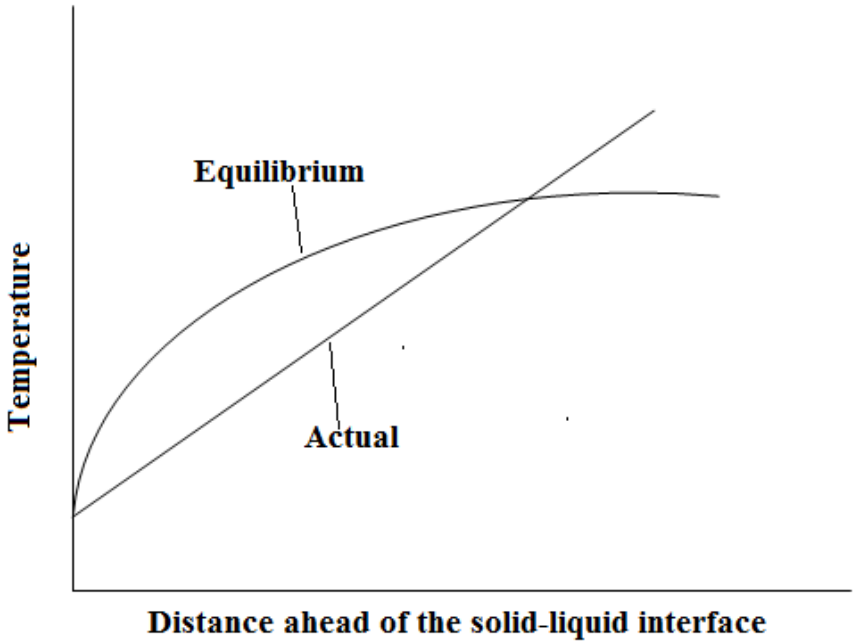

Figure 13: Constitutional undercooling

2.8.1.2 Growth restriction

Addition of solute elements into a matrix alloy controls the growth of the nucleated grains in two ways: first, microsegregation of solute in the interdendritic region can restrict the grain growth. During dendritic solidification, the dendrites push solute elements towards the interdendritic regions, where the solute elements act as barrier to grain growth. Second, generating constitutional undercooling in a diffusion layer ahead of the advancing solid liquid interface slows down the diffusion of solute due to the lower freezing point at the interface. Thus, the diffusion of solute also limits the rate of grain growth [16,41,44,45]

The solute segregation effect can be quantified by the growth restriction factor (GRF), Q, defined as [46].

$$Q = m_l C_o (K_o - 1) \qquad (10)$$

where m_l is the slope of the liquidus line.

Data obtained from binary phase diagrams were used to calculate the GRF values for various alloying elements in magnesium alloys and are shown in Table 7. A solute with a higher value of GRF is expected to have a stronger grain refining effect [11].

Table 7: Slope of the liquidus line, partition coefficient and growth restriction parameter for various alloying elements in magnesium [11]

Element	*m*	*K*	*m(K-1)*	Reaction type
Zr	6.90	6.55	38.29	peritectic
Ca	-12.67	0.06	11.94	eutectic
Si	-9.25	0.00	9.25	eutectic
Ni	-6.13	0.00	6.13	eutectic
Zn	-6.04	0.12	5.31	eutectic
Cu	-5.37	0.02	5.28	eutectic
Ge	-4.41	0.00	4.41	eutectic
Al	-6.87	0.37	4.32	eutectic
Sc	4.02	1.99	3.96	peritectic
Sr	-3.53	0.01	3.51	eutectic
Ce	-2.86	0.04	2.74	eutectic
Yb	-3.07	0.17	2.53	eutectic
Y	-3.40	0.50	1.70	eutectic
Sn	-2.41	0.39	1.47	eutectic
Pb	-2.75	0.62	1.03	eutectic

2.8.2 Grain refinement methods

There are two major methods which are widely used to refine the grain structure of Mg alloys [9, 12]:

i. **Rapid cooling of liquid metal during solidification:**
   Rapid cooling prevents the diffusion of atoms from liquid phase to solid phase, which promotes establishment of constitutional undercooling.

ii. **Chemical grain refinement method:**
   This method involves adding elements or compounds to the melt to promote heterogeneous nucleation.

In the present research, grain refinement of magnesium alloy AZ91E using the chemical grain refinement method was studied. Chemical grain refinement of magnesium alloys can be done by dividing the magnesium alloys into two groups: those alloys with aluminum and those without aluminum [12]. The grain refinement of aluminum free magnesium alloys such as: ZE41, ZK60, WE43 and ML10 can be accomplished by adding zirconium. This method is well established, because the powerful grain refining effect of zirconium is due to the similarity in crystal structure and lattice parameters with magnesium (a=0.320 nm, c= 0.520 nm) and α-zirconium (a=0.330 nm, c= 0.514 nm). This similarity in crystal structure creates smaller wetting angle, which decreases the barrier energy for heterogeneous nucleation [3,10]. However, the grain refining ability of zirconium is ineffective for aluminum based magnesium alloys, as the zirconium readily forms intermetallic compounds with aluminum. Consequently no zirconium is available for refining the grains [10,12,47].

According to Table 8, a variety of chemical grain refinement methods have been developed to refine Mg-Al alloys, such as Elfinal process [48], carbon inoculation [10,12,13,14,15,16,17,49,50,51,52,53,54] and addition of other solutes such as strontium, silicon, calcium and aluminum [11].

Table 8: Summary of grain refiners and grain refinement mechanisms for Mg and Mg alloys [10, 11]

Alloys	Methods of grain refinement	Proposed Mechanism
Mg	Al, Zn, RE, Th, Si, Zr addition	growth restriction by solute effect and/or nucleant particles
Mg-Al-(-Zn-Mn)	C inoculation	nucleation by Al_4C_3
	Sr addition	growth restriction
	SiC addition	nucleation by SiC paticles and/or restriction of growth
Mg-Al-Mn(-Zn)	Elfinal process	nucleation by Fe-Mn-Al compounds
Mg-Al-Mn (-RE-Mn)	Elfinal process	nucleation by Fe compounds
Mg-Y (-Zn)	Zr addition	nucleation by Zr particles
	Ca + Zr	growth restriction / nucleation by Zr particles

In the Elfinal process, anhydrous ferric chloride ($FeCl_3$) is added to the molten magnesium alloy at a temperature range of 740 to 780 °C. According to Cao et al. [48], Fe-Al-Mn particles act as potential nuclei for α-Mg. The main disadvantage of this process is that due to the addition of iron, it increases the risk of corrosion.

The addition of other solutes (e.g., Sr, Si, Ca, Al) refines the grains, because of the microsegregation and constitutional undercooling effects. However, addition of these solutes works effectively on grain refinement for lower wt.% Al (up to 3 wt.% Al) alloys [11].

Among the above mentioned methods, addition of carbon containing agents is the most effective chemical grain refinement method. Carbon containing agents can be added to Mg-Al alloys at lower temperatures (700 °C), and the grain refiners experience less fading with long holding time. Also, a large melt volume of Mg-Al alloys can be refined [10,11]. In addition to this, carbon containing agents can refine Mg-Al alloys up to 9 wt.% Al.

2.8.2.1 Carbon inoculation

This process involves the introduction of carbon into the molten magnesium at 700-800 °C. Carbon can be added into the molten magnesium in the form of pure carbon such as graphite and carbon powder [54], carbonaceous gases (CO, CO_2, CH_4) [10], wide range of carbon containing agents such as hexachlorobenzene (C_6Cl_6), hexachloroethane (C_2Cl_6) [10,13,49], silicon carbide (SiC) [15,18,55], aluminum carbide (Al_4C_3) [16], calcium carbide (CaC_2) [10,56] and master alloys such as Al_4C_3-SiC/Al [17] and Al-1.5C [51].

The grain refining mechanisms by carbon inoculation are not yet fully understood. According to Emley [10], when carbon is added into the molten Mg-Al alloys, it reacts with aluminum in the melt and forms a large number of Al_4C_3 particles, which can act as effective heterogeneous nucleation sites for primary magnesium (α -Mg). Al_4C_3 phases act as effective nucleation sites, because the crystal structures of both Al_4C_3 and α-Mg are hexagonal close packed. Furthermore, the lattice parameters of Al_4C_3 are very close to α-Mg (a = 0.33310 nm, c = 0.49900 nm for Al_4C_3 and a = 0.32030 nm, c = 0.52002 nm for α -Mg, respectively) [57]. The elements Zr, Be, Ti and some rare earth elements interfere with the carbon innoculation process as they form much more stable carbides [10]. These carbides include zirconium carbide (ZrC), titanium carbide (TiC) and beryllium carbide (Be_2C). Crystal structure of these carbides are face centered cubic (FCC) which has very low wettability with hexagonal close packed α-Mg. As a result, these carbides are not effective nuclei and lead to grain coarsening.

The results of studies on carbon inoculation of Mg-Al alloys are presented in Table 9. Al_4C_3 hypothesis was also proposed by some other investigations [15,40,16,50,54], which were done based on microscopic examination using optical and electron microscopes. As Al_4C_3 particle forms by the interaction of carbon and aluminum, it was suggested that for effective grain refinement by carbon inoculation, magnesium alloys must contain more than 2 wt. % Al in order to form Al_4C_3 [15,50]. Although Al_4C_3 hypothesis was the most accepted hypothesis, it ignored the role of carbon as a solute (micro segregation effect). According to Kim et al. [49], the introduction of carbon into the molten Mg-Al alloy may also have strong segregating power for constitutional undercooling and consequently restrict grain growth.

C_2Cl_6 was reported as the most useful grain refiner for Mg-Al alloys [13,45,49]. The only disadvantage is that the refining process by C_2Cl_6 usually releases toxic gases, which cause serious environmental and workplace health and safety concerns [11,58]. As a result, SiC particles have been selected by many researchers as an alternative to C_2Cl_6 for grain refinement of Mg-Al alloys. In addition, SiC particles are relatively inexpensive and easily available. Early investigations [45,59,60] reported that the crystal structure and lattice parameters of SiC are very close to that of α-Mg. Thus, SiC particles may act as heterogeneous nucleation sites for grain refinement.

Table 9: Summary of carbon inoculation techniques

Alloy	Grain refiner (wt. %)	Addition temp. (°C)	Average grain size		Grain refinement mechanism	Ref.
			Base alloy (µm)	Refined alloy (µm)		
Mg-3Al	0.3% Al-SiC	700	417	128	Heterogeneous nucleation by Al_2MgC_2 phase.	[18]
	10% Al-SiC			120		
AZ31	0.25% SiC	700	1150	425	Heterogeneous nucleation by Al_2MgC_2	[63]
	0.5% SiC			375		
	1% SiC			385		
	2%SiC			380		
Mg-3 Al	0.2 % C as carbon powder	750	520	180	Heterogeneous nucleation by Al-C-O phase.	[14]
Pure Mg	0.12% CaC_2	710	2400	1700	Heterogeneous nucleation by CaC_2. CaC_2 also increases constitutional undercooling and restrict grain growth.	[56]
	0.15% CaC_2			1400		
	0.18% CaC_2			1000		
	0.26% CaC_2			125		
	0.4% CaC_2			200		
Mg-9 Al	0.6% C_2Cl_6	740	489	340	Duplex heterogeneous nucleation by Al_4C_3 and $Al_8(Mn,Fe)_5$	[49]
AZ91			460	97		

Alloy	Grain refiner (wt. %)	Addition temp. (°C)	Average grain size		Grain refinement mechanism	Ref.
			Base alloy (µm)	Refined alloy (µm)		
Mg-1 Al	0.15% SiC	700	710	330	Heterogeneous nucleation by Al_4C_3 formed by the reaction between SiC and Mg-Al alloy	[15]
	0.3% SiC			300		
	0.3% SiC and 0.3% Mn			245		
Mg-2 Al	0.15% SiC		260	220		
	0.3% SiC			120		
	0.3% SiC and 0.3% Mn			180		
Mg-3 Al	0.15% SiC		200	175		
	0.3% SiC			120		
	0.3% SiC and 0.3% Mn			227		
Mg-6 Al	0.15% SiC		150	140	Heterogeneous nucleation by Al_4C_3 formed by the reaction between SiC and Mg-Al alloy	
	0.3% SiC			130		
	0.3% SiC and 0.3% Mn			205		
Mg-9 Al	0.15% SiC		130	105		
	0.3% SiC			95		
	0.3% SiC and 0.3% Mn			100		

Alloy	Grain refiner (wt. %)	Addition temp. (°C)	Average grain size		Grain refinement mechanism	Ref.
			Base alloy (μm)	Refined alloy (μm)		
Mg-3Al	Synthetic Graphite	735	380	175	Heterogeneous nucleation by Al_4C_3	[40]
	SiC			180		
AZ63B	1% Al-1.5C	800	270	50	Heterogeneous nucleation on the Al-,C-, O-, Fe- and Mn-rich particles	[51]
Mg-3Al	1% Al_4C3	735	480	190	Heterogeneous nucleation by Al_4C_3	[16]
		785		185		
Mg-3Zn	0.6 wt.% C as nucleant 5000	750	450	500	No grain refinement effect to Mg alloys that do not contain Al	[50]
Mg-3Al			400	170	Heterogeneous nucleation by Al_4C_3	
AZ91E	0.02 wt. % C as carbon powder	750	300	300	Heterogeneous nucleation by Al_4C_3	[61]
	0.04 wt. % C as carbon powder			140		
	0.06 wt. % C as carbon powder			77		
	0.08 wt. % C as carbon powder			75		

Alloy	Grain refiner (wt. %)	Addition temp. (°C)	Average grain size		Grain refinement mechanism	Ref.
			Base alloy (μm)	Refined alloy (μm)		
AZ31	0.2% Al_4C_3-SiC/Al	700	1300	270	Heterogeneous nucleation by Al_4C_3 and SiC or by duplex phase which is composed of Al_4C_3 and SiC.	[17]
	0.5% Al_4C_3-SiC/Al			225		
	1% Al_4C_3-SiC/Al			270		
AZ63	0.5% Al_4C_3-SiC/Al		300	200		
	1% Al_4C_3-SiC/Al			180		
AZ91	0.5% Al_4C_3-SiC/Al		170	No variation		
	1% Al_4C_3-SiC/Al			No variation		
AZ31	0.6% C_2C_{l6}	780	400	120	Strong segregating power of carbon increase constitutional undercooling and restrict grain growth.	[13]

As shown in Table 9, Liu et al. [17] added Al_4C_3-SiC/Al to the AZ31, AZ63 and AZ91. The grain refiner (Al_4C_3-SiC/Al) was prepared from SiC powder of 10 μm particle size and commercially pure Al. The SiC was added to molten Al and then heated up to 950°C in an electric furnace. The mixture of SiC and Al was poured into a permanent mould. According to Equation 11, Al reacted with SiC and formed Al_4C_3 [15,62]. Thus the grain refiner consisted of two effective heterogeneous nucleant sites. The average grain size of AZ31 after grain refinement was drastically reduced from 1300 μm to 270 and 225 μm with addition of 0.2 and 0.5 wt.% Al_4C_3-SiC/Al. The grain size of AZ63 was reduced from about 300 to about 200 μm

with the addition of 0.5 wt. % Al_4C_3-SiC/Al master alloy and to about 180 µm with the addition of 1 wt. % Al_4C_3-SiC/Al. The relative grain structure of AZ63 with the addition of Al_4C_3-SiC/Al is shown in Figure 14. It was found that the addition of Al_4C_3-SiC/Al above 0.5 wt.% had little influence on further refinement of the grain size of both AZ31 and AZ63.

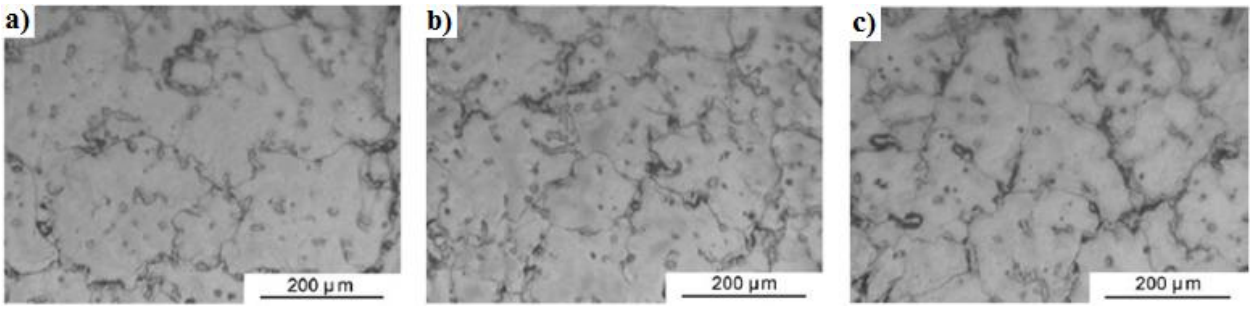

Figure 14: Grain structure of as-cast AZ63 alloy with Al_4C_3-SiC/Al master alloy: a) Base alloy; b) 0.5 wt. % Al_4C_3-SiC/Al; c) 1 wt. % Al_4C_3-SiC/Al [17]

Addition of Al_4C_3-SiC/Al to the AZ91 had no influence on the alloy's mean grain size. Because of the high Al content in AZ91 alloy, the grains are already refined due to microsegregration effect of Al. The grain refinement of AZ31 and AZ63 with the addition of Al_4C_3-SiC/Al was due to the presence of heterogeneous nucleation sites of Al_4C_3 and SiC. The addition of extra Al may have enhanced nucleation by generating a solute diffusion layer ahead of advancing solid-liquid interface during growth.

As shown in Table 9, Easton et al. [15] added master alloys of 0.15 and 0.3 wt.% SiC with pure Mg to the molten Mg-Al alloys. The grain size of Mg-1 wt.% Al was drastically reduced with the addition of 0.15 wt.% SiC. No significant grain refinement was observed with the addition of 0.15 wt.% SiC to higher Al content Mg-Al alloys. After further increase of SiC to 0.3 wt.%, a small reduction in grain size was observed for Mg-Al alloys. It was found that the Mg-Al alloys with lower content of Al were much more effectively grain refined by the addition of SiC. Because the lower Al content Mg-Al alloys had lower growth restriction effect, Q, which depends on wt.% of solute, C_o. Due to the lower Q value, Mg-1 wt.% Al alloy had a tendency to form relatively bigger grains compared to Mg-Al alloys with higher wt.% Al. As a result, adding SiC particles to Mg-1 wt.% Al had led to significant reduction in grain size. According to Easton

et al. the grain refinement of Mg-Al alloys with the addition of SiC was due to the heterogeneous nuclei sites of Al_4C_3, which formed based on the reaction of Equation 11.

$$Al + SiC \rightarrow Al_4C_3 + Si \quad (11)$$

0.3 wt.% Mn with 0.3 wt.% SiC was added by Easton et al.[15] to Mg-Al alloys. Easton et al. proposed that addition of Mn with SiC formed ternary carbide, $AlCMn_3$. The crystal structure of $AlCMn_3$ is face centered cubic, which has very poor wettability with the hexagonal close packed α-Mg matrix. As a result, $AlCMn_3$ was ineffective site for α-Mg and resulted in grain coarsening.

As shown in Table 9, the SiC was also added to molten AZ31 alloy during casting process by Schiffl and Easton [63]. The average grain size of AZ31 alloy reduced form 1150 μm to 425 μm with the addition of 0.25 wt.% SiC. Increasing the addition level of SiC exceeding 0.5 wt.% had very little influence on grain size. Schiffl and Easton suggested that the grain refinement mechanism was possibly from the heterogeneous nucleation by ternary carbides Al_2MgC_2. The ternary carbides were formed from the reaction of dissolved SiC and molten Mg-Al alloy.

In a more recent study, SiC was added in the form of Al-SiC master alloy consisting of 56 wt.% Al and 44 wt.% SiC to the molten Mg-3 wt.% Al alloy by Huang et al. [18]. It was observed that the grain size significantly reduced and became uniform. As shown in Figure 15, the grain size of Mg–3 wt.% Al alloy was reduced from 417 μm to 128 μm by the addition of 0.3 wt.% Al-SiC and to 120 μm by the addition of 10 wt. % Al-SiC, respectively. Therefore, Huang et al. suggested that increasing the amount of SiC from 0.3 wt.% to 10 wt.% had a little influence on the grain size of Mg–Al alloys. Three different phases were indentified from X-ray diffraction patterns and include: Al_2MgC_2, Mg_2Si and $Mg_{17}Al_{12}$. The formation of the β- $Mg_{17}Al_{12}$ phase was due to the high Al content along the grain boundaries, Mg_2Si and Al_2MgC_2 phases formed due to the reaction between of SiC and Mg-Al matrix. Instead of Al_4C_3, ternary carbide Al_2MgC_2 phase was found. Due to similarity in crystal structure between Al_2MgC_2 and the α-Mg, the ternary carbide was proposed as the heterogeneous nuclei site.

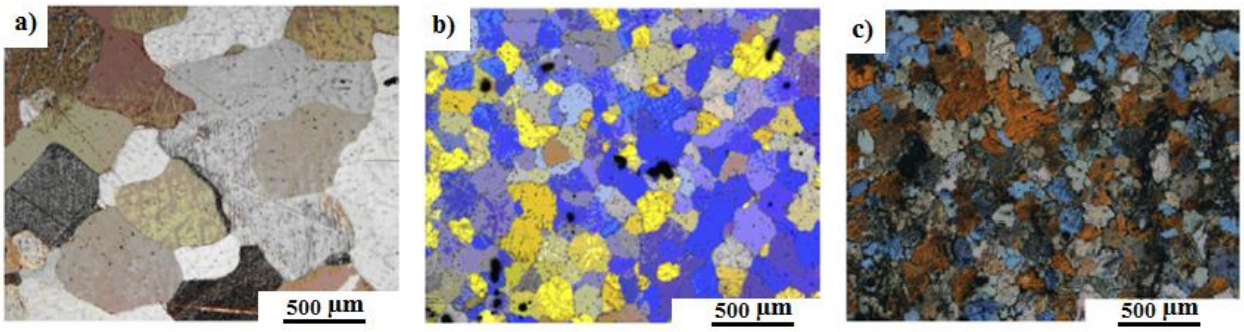

Figure 15: Grain structure of as-cast Mg-3 wt. % alloy with Al-SiC master alloy: a) Base alloy; b) 0.3 wt.% Al-SiC; c) 10 wt. % Al-SiC [18]

2.8.2.2 Adding other additives

Lee et al. [11] tried several additives to achieve grain refinement in their investigation. These were Al, Si, Sr and Ca. The effects of these solutes have already been discussed in Section 2.7.1. Master alloys including Al–4Ti–5B [52] and Mg–10Sr [64] were also added in Mg alloys to improve on grain refinement efficiency of Mg alloys.

It was shown by Wang et al.[52] that the optimum addition level of master alloy Al–4Ti–5B was 0.3 wt. % for an effective reduction in grain size of AZ31, where the average grain size was reduced to 80 µm from 1100 µm. Wang et al. observed the sample under SEM and proposed that the grain refinement was due to the heterogeneous nucleation by TiB_2. According to Yang et al., the addition of Mg-10Sr into AZ31 had grain growth restriction effect, which has led to grain refinement of AZ31.

Recently, Elsayed et al. [65] examined Al-5Ti-1B and Al-1Ti-3B master alloys as grain refiners for AZ91E. They found 1.0 wt.% addition of Al-1Ti-3B reduced the grain size of the base alloy of AZ91E from 1000 ± 131 µm to 361 ± 67 µm and 0.1 wt.% Al-5Ti-1B reduced the grain size to 323 ± 59.

In this current research, a new technique called “Spark Plasma Sintering” (SPS) process was used to prepare the grain refiner of Al-SiC master alloy. None of the previous studies have used

SPS to prepare a grain refiner for AZ91E alloy. The spark plasma sintering technique is discussed in the following section.

2.9 Spark plasma sintering technique

In spark plasma sintering (SPS), powders of materials are introduced into a sintering die. SPS simultaneously applies pressure and electric current directly on the powder. Figure 16 illustrates a schematic of SPS machine. On-Off DC pulse voltage and current creates spark discharge and Joule heat points (Figure 17) between the powder particles. The surfaces of the particles begins to melt as a local high temperature state of up to 10,000 ℃ is developed in the gap between the surfaces of the particles. The plasticised particles form "necks" around the area of contact. The uniaxial force plays an important role to limit the particle growth, promotes the removal of pores and enhances diffusion. The entire process from powder to finished compact material is completed quickly, with high uniformity and without changing the particle characteristics [66,67,68].

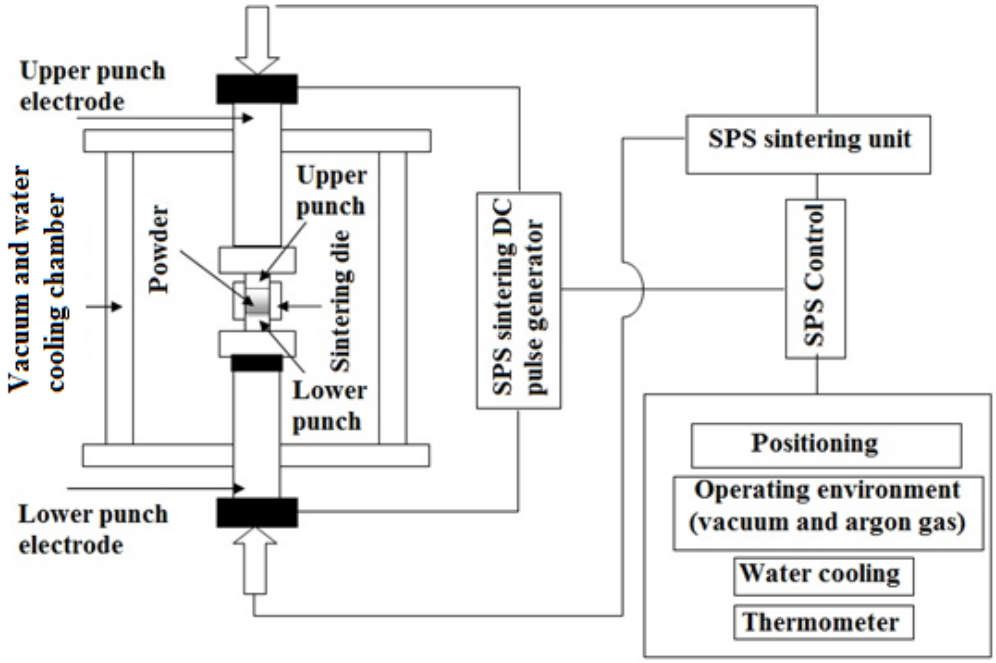

Figure 16: Schematic of a spark plasma sintering machine

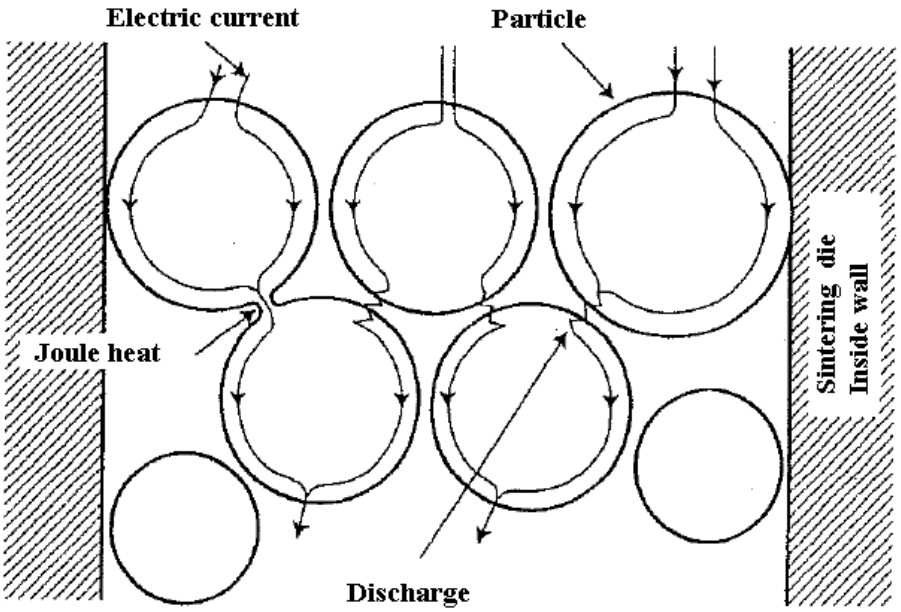

Figure 17: Current flow through powder particles [68]

The main advantage of using SPS for the preparation of a grain refiner is due to the ability to homogeneously disperse 3 μm SiC particles in an aluminum matrix. Addition of SiC particles on such scale is normally not feasible, due to their flotation upon addition to liquid Mg. However, when the SPS prepared master alloy was added into the molten magnesium alloy for grain refinement, the aluminum melted and allowed the SiC particles to homogeneously distribute throughout the molten magnesium. These SiC particles were hoped to provide heterogeneous nuclei sites. Additionally, the SPS method was used in order to combine compounds which would normally be difficult to sinter using traditional methods.

3 Experimental Procedure

This chapter provides a brief discussion of the procedures that have been followed in casting experiments, sample preparation and sample observation under optical and scanning electron microscope, X-ray energy dispersive spectroscopy and thermal analysis using differential scanning calorimetry. The procedures of measuring Rockwell hardness, area percentage β-$Mg_{17}Al_{12}$ phase and porosity, solidus and liquidus temperature and area under the curve of solidus and liquidus peak are also discussed.

3.1 Preparation of Al-SiC master alloy

Al-SiC master alloy discs of 20 mm diameter and 4 mm thick were prepared by spark plasma sintering process. The SPS processing was completed by Professor Mathieu Brochu at McGill University. 50 wt. % SiC powder of 3 to 10 μm and 50 wt. % pure Al were introduced in a graphite die of the SPS machine (Model 10-3 made by "Thermal Technology LLC"). As shown in Figure 18, 3 to 10 μm SiC particles were retained in the Al-SiC master alloy.

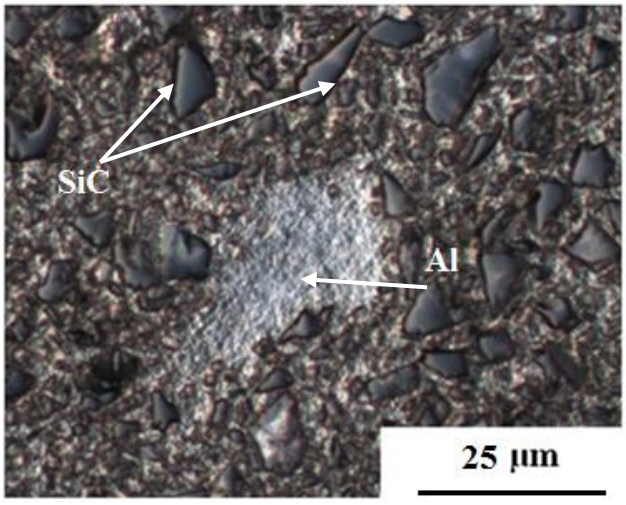

Figure 18: Optical micrograph of a SPS processed Al-SiC master alloy

3.2 Grain refinement of AZ91E magnesium alloy

Casting trials with AZ91E alloy were conducted using the gravity permanent mould casting process. This casting process involved three steps, which are described below:

Step 1: Material and tools preheating

i. **Preheating of graphite moulds**

Graphite moulds of 3.4 cm inner diameter and 6 cm height were preheated to 650 °C on top of an electric resistance furnace. This preheating was done to remove moisture and to slow down casting solidification.

ii. **Preheating of alloy**

Approximately 500g of AZ91E alloy magnesium alloy was preheated to 150 °C. Table 10 shows the chemical composition (wt.%) of the AZ91E alloy used, as provided by the ingot manufacturer.

Table 10: Chemical composition of AZ91E alloy used in this research

Element	Al	Zn	Mn	Si	Cu	Fe	Be	Other	Mg
Composition (wt.%)	8.7	0.53	0.23	0.05	0.006	0.003	0.0012	0.3	Balance

iii. **Preheating of melting tools**

The skim spoons, master alloy and stir rods were preheated to 250 °C on top of the electric resistance furnace.

Step 2: Melting and addition of grain refiner

The preheated AZ91E magnesium alloy was melted in a low carbon steel crucible at 750 °C in an electric resistance melting furnace under a CO_2 cover gas (0.283 m^3/ hr). 0.1 wt. % Al-SiC master alloy was added into the molten AZ91E alloy at a temperature of 740 °C -750 °C. Then, the melt was stirred for 30 seconds with the preheated rod to ensure homogeneous distribution of

Al-SiC master alloy and left to activate for 5 min. The same procedure was followed for 0.2, 0.5 and 1 wt. % Al-SiC addition.

Step 3: Metal pouring

Before taking out the steel crucible from the melting furnace, the CO_2 flow rate was increased to 0.425 m^3/ hr. Then, the steel crucible with molten metal was taken out from the furnace, skimmed and allowed to cool to the pouring temperature of 720 °C. Three preheated graphite crucibles were taken out from the electric preheating furnace and the melt was poured into these three graphite crucibles. The solidifying melt was covered to avoid oxidation. The castings were cooled at a cooling rate of 1 °C/s until cooling to room temperature. After solidification, the castings were removed from the mould and labelled.

Three repeat experiments were performed for each grain refinement addition level. Further, three base metals AZ91E alloys without any grain refiner were also made in order to study the effect of grain refiner addition on the alloy grain size. From the three repeats, two samples were prepared for metallography and analyzed. These samples are labelled as Trial 1 and Trial 2.

3.3 Metallography sample preparation

A standard polishing procedure was followed for optical microscope, scanning electron microscope (SEM) and energy dispersive spectroscope (XEDS) work.

i. As shown in Figure 19 the samples were cut at 4.5 cm height from the bottom by a hacksaw. A SiC abrasive belt of 80 grit was used to obtain a flat surface. Then, 320, 400 and 600 grit SiC abrasive papers were used successively for manual polishing. Samples were rinsed thoroughly between polishing on successive SiC abrasive papers to avoid scratches. After completing grinding with SiC papers, the samples were polished with 1/0, 2/0, 3/0 and 4/0 size emery papers. Water was used to clean the samples prior to polishing on the next grit.

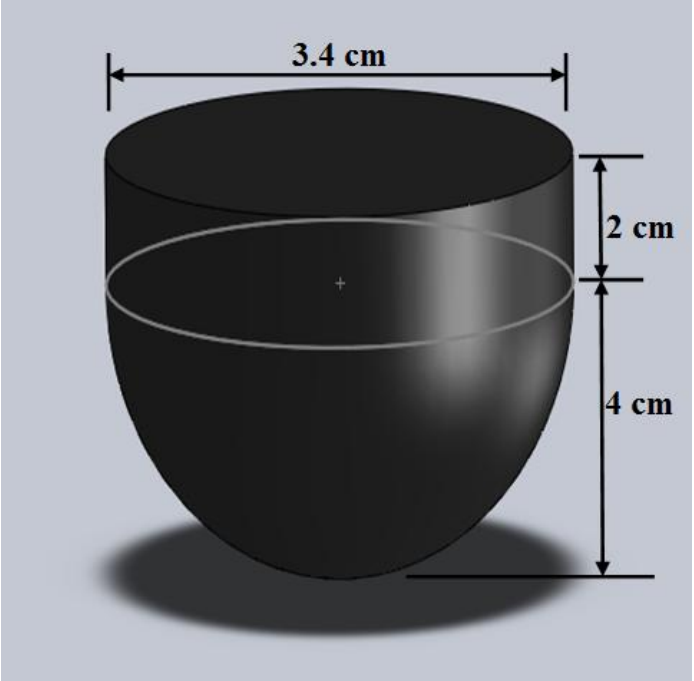

Figure 19: Dimensions of as-cast specimens

ii. Final polishing was done using a "Mark V Lab" disk polisher with an intermediate-nap cloth. 9, 3 and 1 µm diamond pastes were used. New polishing cloth was used for each size of diamond paste. The samples were polished until all scratches appeared uniform and uni-directional. Ethanol was used to wash the samples between individual polishing stages. Wheel speed of 120 rpm was maintained throughout. Two types of etchants were used for microstructure enhancement, as listed in Table 11.

Table 11: Metallographic etchants for AZ91E alloy

Etchant	Composition	Duration	Purpose
1	1ml acetic acid 50 ml distilled water 150 ml ethanol	4 min	To reveal grain structure
2 (Glycol)	1ml HNO_3 24ml distilled water 75 ml ethylene glycol	15 s	To reveal intermetallic compounds

3.4 Optical microscopy

A Carl Zeiss Axio Observer inverted microscope was used for all optical microscopy tasks. The microscope had four magnification lenses: 5x, 10x, 50x and 150x. The eyepiece of the microscope provided additional 10x magnification, giving a total of 50x, 100x, 500x and 1500x magnification. Micrographs were taken using bright field (BF), dark field (DF) and differential interference contrast (DIC) mode. Table 12 summarizes the combination of mode and magnification lens used for specific tasks.

Table 12: Microscope set-up for analysis

Mode	Lens	Purpose
DF	5X	Measurement of grain sizes
BF	50X	Measurement of area percentage of porosity
BF	10X	Measurement of area percentage of Intermetallic compounds

An Omnimet softare was used for image analysis. Before taking any measurement, the software was calibrated using standard ruler provided by manufacturer.

As shown in Figure 20, the horizontal width of grains was measured randomly using the parallel distance option. Figure 21 illustrates the two regions: interior and wall regions of the casting. All grains were measured inside the interior region of the samples. The number of grains which were considered for the grain size measurement of each alloy composition is listed in Table 13.

Table 13: Number of grains measured for casting trial 1 and trial 2

Wt.% Al-SiC	Number of grains measured	
	Casting Trial 1	Casting Trial 2
0	500	500
0.1	500	500
0.2	282	282
0.5	350	350
1	400	400

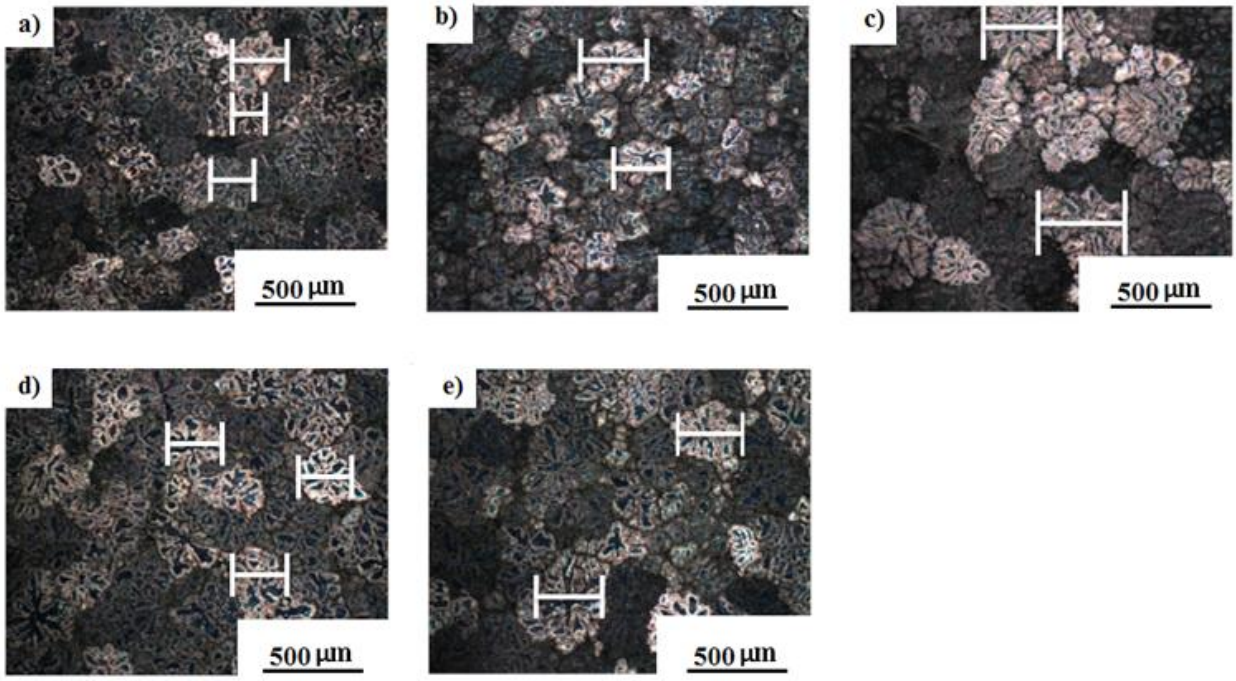

Figure 20: Example of grain size measurement in AZ91E alloy: a) Without Al-SiC; b) 0.1 wt.% Al-SiC; c) 0.2 wt.% Al-SiC; d) 0.5 wt.% Al-SiC; e) 1 wt.% Al-SiC

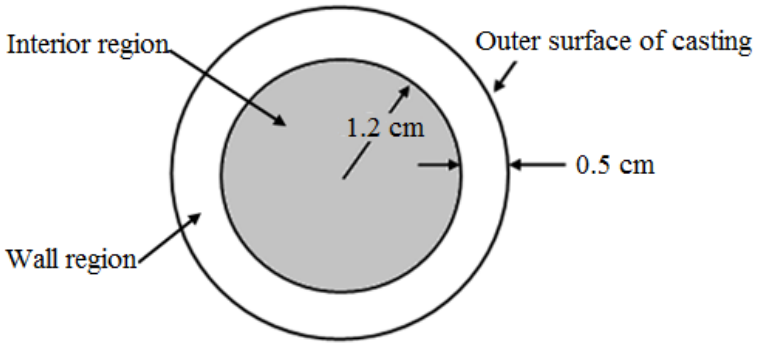

Figure 21: Sample regions for grain size and hardness measurements

In order to calculate the volume fraction of $Mg_{17}Al_{12}$ phase and porosity of studied alloys, the cross sectional area of the studied alloys was observed to measure the area fraction of β-$Mg_{17}Al_{12}$ phase and porosity. For simplicity it was assumed that the area fraction of porosity was proportional to the volume fraction of porosity.

As shown in Figure 22 and Figure 23, mean area percentage of β-$Mg_{17}Al_{12}$ phase and porosity were measured using color contrast routine analysis. At least 20 random fields were analyzed in different regions of the studied alloys for both β-$Mg_{17}Al_{12}$ phase and porosity measurement in Trial 1 and Trial 2.

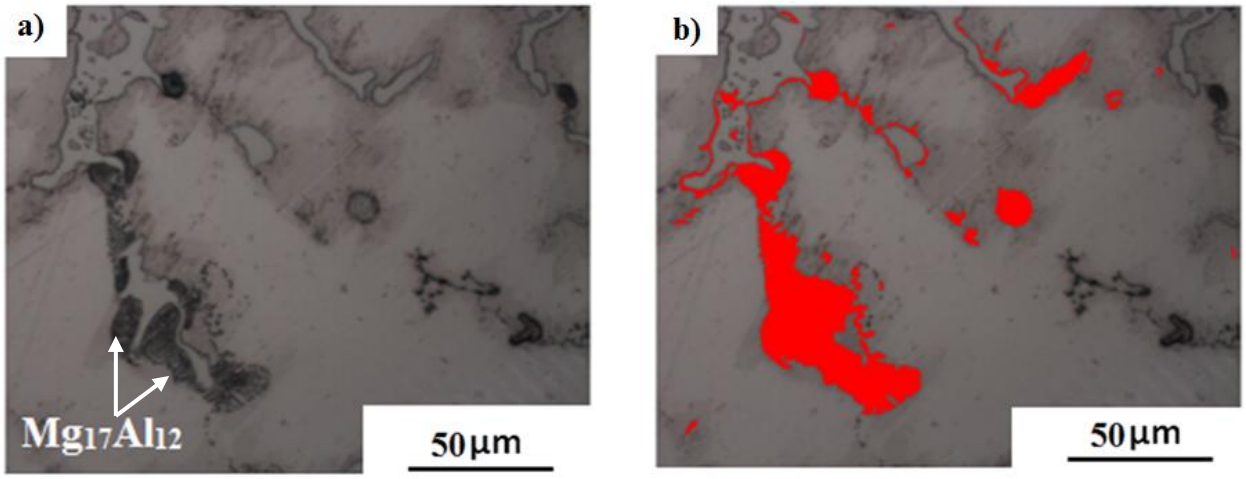

Figure 22: Optical micrograph: a) Intermetallic compound ($Mg_{17}Al_{12}$); b) routine analysis for measurement of area percentage of $Mg_{17}Al_{12}$

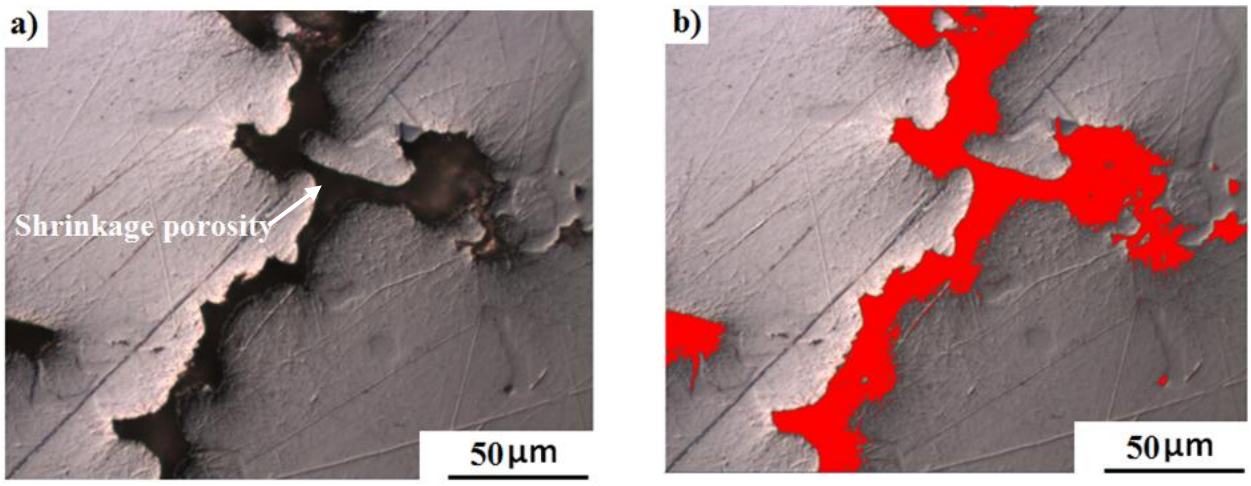

Figure 23: Optical micrograph: a) Porosity; b) routine analysis for area percentage of porosity

Paired *t*-tests were performed in order to determine whether the replications (i.e., Trial 1 and Trial 2) were statistically equivalent in their effect on mean grain size, mean area percentage of β-$Mg_{17}Al_{12}$ phase and porosity, respectively.

3.5 Scanning electron microscope and energy dispersive spectroscopy

A "TESCAN Mira" scanning electron microscope (SEM) equipped with an "Oxford" energy dispersive spectroscope (XEDS) was used for microstructure investigation. Before doing any compositional analysis of studied alloys, the XEDS was calibrated with pure copper. Both SEM and XEDS were operated at an accelerating voltage of 20keV. 20 mm working distance was maintained for XEDS work. All the SEM images were taken using secondary electrons (SE) for better morphology of interested particles.

3.6 Rockwell hardness testing

A Wilson Rockwell hardness tester was used for hardness measurement of studied alloys. The hardness measurements were taken using B scale, where a 1/16 inch ball was used with 100 kg force. The hardness tester was calibrated before starting the testing of studied alloys. The hardness tester was calibrated using a standard hardness calibration block. Two regions: i) interior region and ii) wall region were selected for hardness measurement of studied alloys, as shown in Figure 21. In each region, 10 random measurements were obtained. A minimum distance equivalent to 3 times the diameter of the indenter was maintained between two consecutive testing locations.

3.7 Differential scanning calorimetry

A "NETZSCH STA 449" DSC was used for determining the solidus and liquidus temperature of all studied alloys and enthalpy of liquidus reaction of selected AZ91E alloys treated with Al-SiC. Lowest (0.1 wt.%) and highest (1 wt.%) Al-SiC content alloys were selected for enthalpy measurement in order to determine the effect of Al-SiC on the enthalpy of transition during

liquidus reaction. Due to experimental challenges (e.g., metal oxidation, shortage of nitrogen gas and furnace malfunction) only two alloy compositions were selected for enthalpy measurement. However, all the alloy compositions were observed for determining the solidus and liquidus temperature. Initial temperature for the DSC measurement was set at 30 °C. The experimental alloys were heated to 675.5 °C at a heating rate of 20 °C/min. The alloys were heated to 675.5 °C to ensure 100% liquid state of these alloys. After reaching its liquid state, the studied alloys were cooled down to room temperature at a rate 20 °C/min, which is the highest cooling rate in this DSC. "NETZSCH Proteus Thermal Analysis" software was used to evaluate the DSC curve. Figure 24 shows a screen shot of the software for evaluation of the DSC curve. There are two sets of peaks, one set of peaks for heating and the other for cooling. The first peak (peak # 1) corresponds to solidus temperature and second peak (peak # 2) corresponds to the liquidus temperature. The phase transformation temperatures were determined by averaging the two corresponding peak temperature in heating and cooling curve. As shown in Figure 24, enthalpy of transition during liquidus reaction was determined from the area under the liquidus curve. The two end points (shown by two parallel lines) of the liquidus curve were determined in such a way that the line between these two points followed the baseline DSC curve.

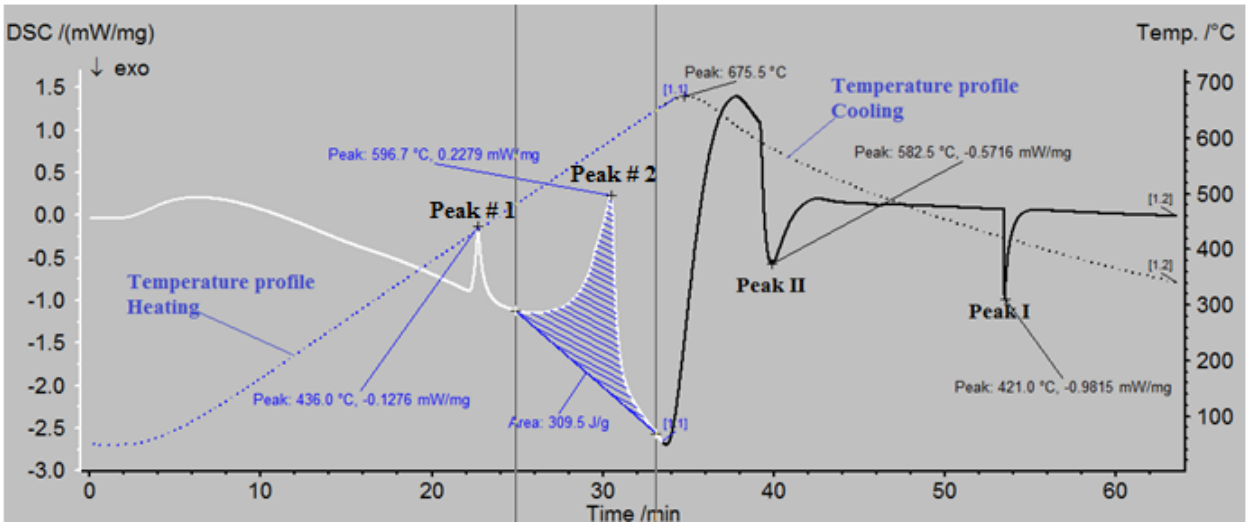

Figure 24: A screen shot from "NETZSCH Proteus Thermal Analysis" software

3.8 Possible sources of error

During the experimental procedure some instrumental and measurement error was expected. The limits on these errors are summarized in the following table. Many of these errors are also included in graphs and plots of results, as appropriate.

Table 14: Possible source of error and error value

Source of error	Value
Accuracy of temperature measurement in DSC	±1.5 to ± 1.7 K
Accuracy of enthalpy measurement in DSC	± 3%
Grain size measurement in Omnimet software	± 5 to ± 9.3 µm
β-phase measurement Omnimet software	± 0.9 to ± 1.4 %
Porosity measurement Omnimet software	± 0.4 to ± 0.7 %
Elemental composition measurement XEDS	± 0.1 wt%

4 Results and Discussion

4.1 Effect of Al-SiC master alloy on the structure of AZ91E alloy

4.1.1 Effect of Al-SiC on average grain size

A summary of the measurements of the mean grain size for each sample is shown in Table 15. Based on the statistical analysis (paired *t*-test) it can be concluded that the mean grain size of two repeats (Trial 1 and Trial 2) was the same (detailed calculation is presented in Appendix A).

Table 15: Mean grain size of grain refined alloys

Wt.% Al-SiC	Mean grain size (μm)		
	Trial 1	Trial 2	Grand average
0	230.6 ± 5.3	224.3 ± 4.7	227.5 ± 5.0
0.1	201.6 ± 5.2	193.3 ± 4.6	197.5 ± 5.0
0.2	367.9 ± 11.8	353.8 ± 9.3	360.9 ± 10.5
0.5	321.1 ± 8.3	331.6 ± 7.3	326.3 ± 7.8
1	302.8 ± 7.1	290.2 ± 5.7	296.5 ± 6 .4

Based on Table 15, single factor ANOVA analysis was performed (details in Appendix B) and concluded that varying the amount of Al-SiC grain refiner had a statistically significant effect on the mean grain size. The final mean grain size of the grain refined AZ91E alloy is shown in Figure 25. Error bars in Figure 25 represent the 95% confidence intervals for each alloy composition.

As shown in Figure 25, the final mean grain size of the unrefined alloy was 227.5 μm. The grain size decreased to 197.5 μm with the addition of 0.1 wt.% Al-SiC. Further addition of Al-SiC increased the mean grain size. With the addition of 0.2 wt.% Al-SiC, the grain size increased to 360.9 μm, while the addition of 0.5 and 1 wt.% Al-SiC increased the grain size to 326.3 and 296.5 μm, respectively. Macro photographs of the grain refined alloys are shown in Figure 26.

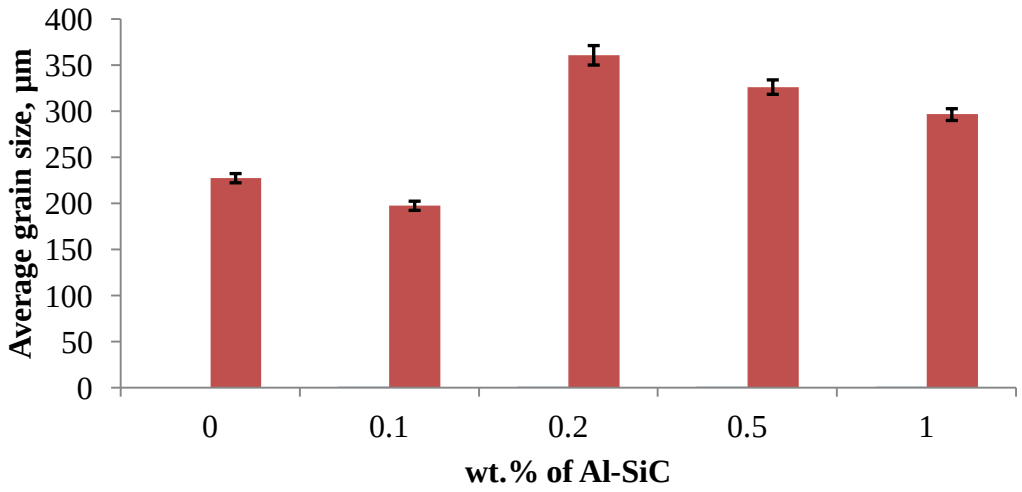

Figure 25: Final mean grain size of AZ91E alloy at various wt.% of Al-SiC

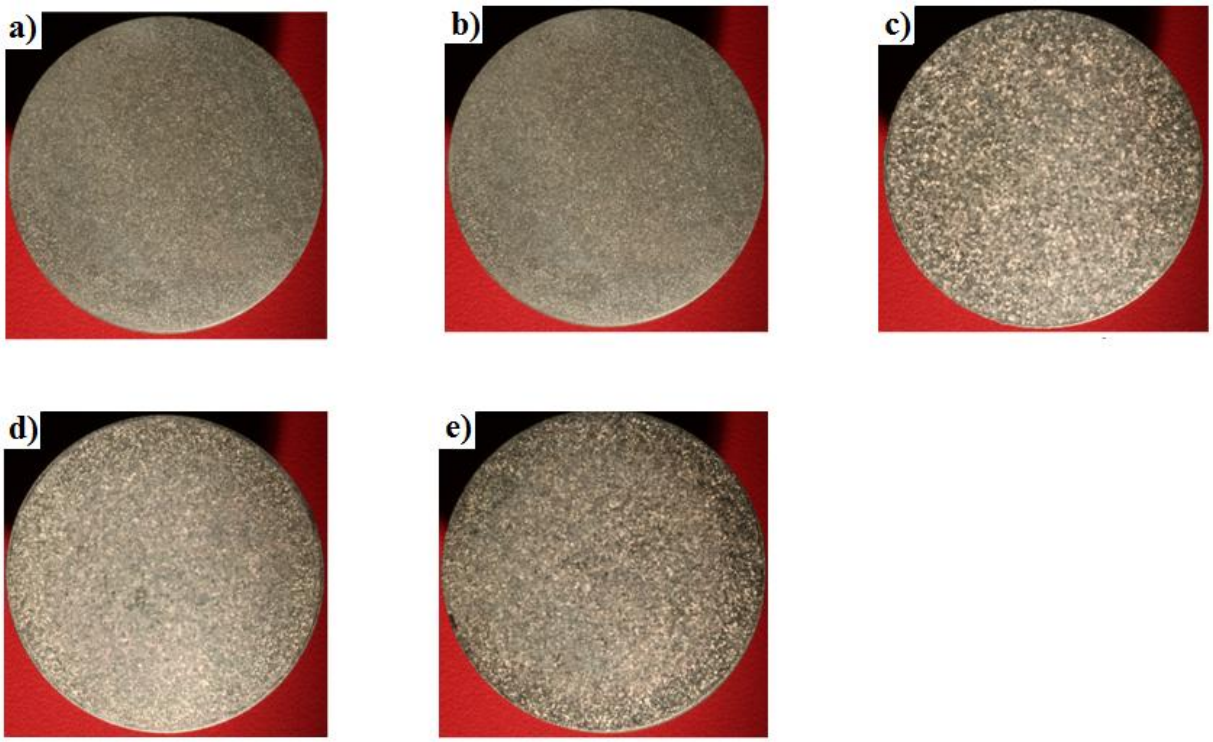

Figure 26: As-cast grain structure of AZ91E alloys after 4 min etching: a) Without Al- SiC; b) 0.1 wt.% Al-SiC; c) 0.2 wt.% Al-SiC; d) 0.5 wt.% Al-SiC; e) 1 wt.% Al-SiC. The diameter of each sample is 3.4 cm.

As shown in the literature review in Table 9, typical grain size of Mg-Al alloys (e.g., Mg-9 wt.% Al, AZ91 and AZ91E) is expected to vary from 130 to 490 μm without the addition of any grain refiner. In the current research, the grain size of unrefined AZ91E alloy was also found within the grain size limit (130 to 490 μm) of past investigations [15,17,49,61]. It is also recognized that the grain size depends on the exact alloy composition and casting process (e.g., preheating temperature of the mold). As the measured grain size of AZ91E alloy in the current research was similar to that of past investigations, it can be concluded that the experimental procedure of the current research is comparable to industrial practice, especially for permanent mold and sand casting applications.

As shown in the literature review in Table 9, increasing the addition level (wt.%) of SiC tends to reduce the gain size of Mg-Al alloys [15,17,18,63]. However, only exception was found by Easton et al. [15], when SiC and Mn were added to Mg-Al alloys with more than 2 wt.% Al; In the presence of Mn, the grain size increased with the introduction of SiC. Easton et al. [15] concluded that addition of Mn inhibited the grain refining effect of SiC. In the current research, addition of Al-SiC exceeding 0.1 wt.% to the AZ91E alloy also resulted in grain coarsening. The mechanisms of grain coarsening and refining of the current research will be discussed discussed based on SEM analysis in Section 4.2. As will be apparent, the current research supports Easton's et al. observation and further suggests that presence of complex Al-Mn intermetallics interfered with the grain refining efficiency of SiC particles.

4.1.2 Effect of Al-SiC on β-$Mg_{17}Al_{12}$ phase

The size, shape and distribution of the β-$Mg_{17}Al_{12}$ phase influences the hardness and corrosion resistance of the alloy. The morphology of β- phase was usually in the form of a lamellar eutectic forming near the interdendritic regions, as shown by a representative micrograph in Figure 27. A summary of mean area percentage of β- phase for each addition level of grain refiner is shown in Table 16. From the paired *t*-test, it was concluded that there was no statistical difference in the mean area percentage of β- phase between the repeat casting conditions of Trial 1 and Trial 2 (detailed calculation is presented in Appendix C).

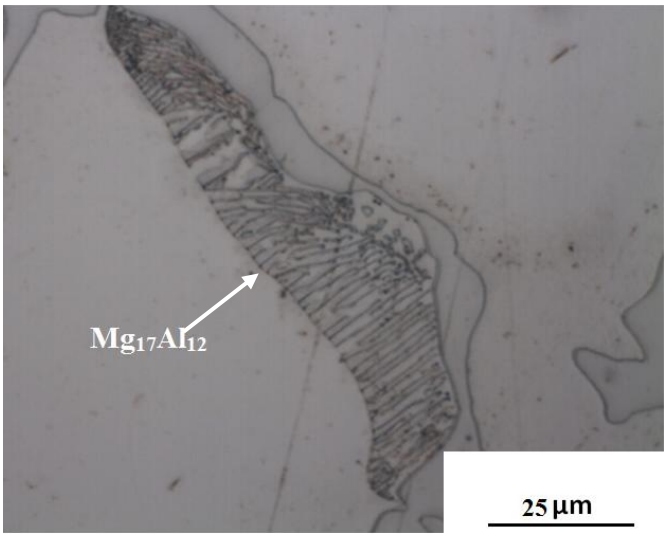

Figure 27: β-$Mg_{17}Al_{12}$ phase in AZ91E alloy with 1 wt.% Al-SiC

Table 16: Mean area percentage of β-$Mg_{17}Al_{12}$ phase of grain refined alloys

wt.% Al-SiC	Mean area % β phase (%)		
	Trial 1	Trial 2	Grand average
0	5.4 ± 1.0	5.4 ± 0.9	5.4 ± 1
0.1	5.4 ± 0.9	5.5 ± 1.2	5.4 ± 1.1
0.2	5.2 ± 1.1	5.3 ± 1.2	5.2 ± 1.2
0.5	6.2 ± 1.4	6.3 ± 1.1	6.2 ± 1.3
1	6.7 ± 1.2	6.5 ± 1.3	6.6 ± 1.3

Based on Table 16, single factor ANOVA analysis was performed (details in Appendix C) and concluded that varying the amount of Al-SiC grain refiner had a statistically significant effect on the mean area percentage of the β-phase. The final mean area percentage of β-phase of the grain refined AZ91E alloy is shown in Figure 28. Error bars in Figure 28 represent the 95% confidence intervals for each alloy composition.

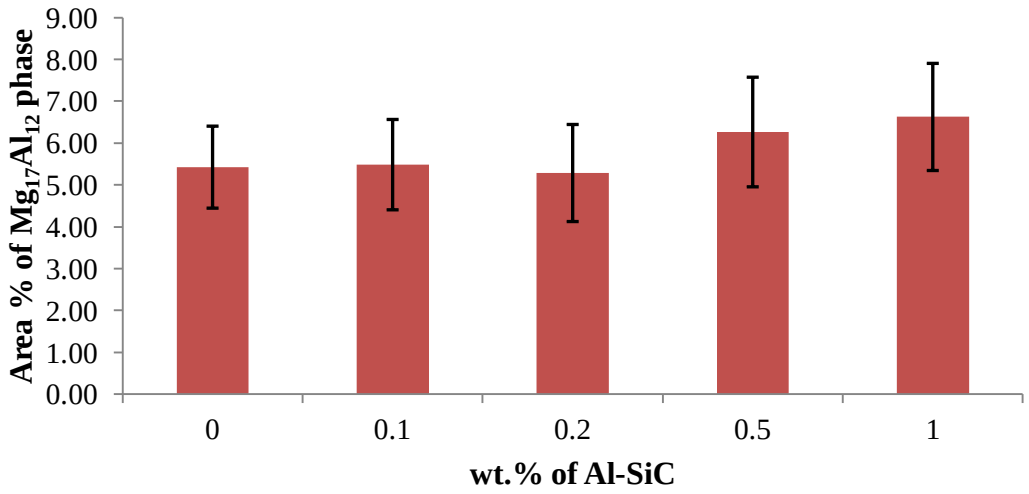

Figure 28: Final mean area percentage of β-$Mg_{17}Al_{12}$ phase for the studied alloy composition

As shown in Figure 28, increasing the wt.% of Al-SiC increased the amount of the β- phase. The highest mean area percentage of β-phase was found with the addition of 1 wt.% Al-SiC. As discussed in the literature review during solidification of AZ91E alloy, Al originating from the master alloy (Al-SiC) as well as from the super saturated solid solution was rejected towards the interdendritic region. According to the Mg-Al binary phase diagram (Figure 2), the maximum solubility of Al in α-Mg is 12 wt.% at a temperature of 437 °C. For higher solute concentrations, Al forms the eutectic β- $Mg_{17}Al_{12}$ phase. As a result, the total volume fraction of the β- phase in the alloy was seen to depend on the amount of aluminum in the system and appeared to increase with increasing amount of master alloy addition.

The increased amount of β-phase may potentially improve the room temperature properties of the new alloy. However, it is known that for high-temperature applications β-phase is a contributing factor for the poor creep performance of aluminum-containing Mg alloys.

The increasing amount of β-phase would likely have also a beneficial effect on the castability of the alloy. It is well established that eutectic alloys have superior castability, since these alloys do not experience semi-solid state (i.e., liquid transforms directly to solid solution). Consequently,

addition of the Al-SiC master alloy would increase the alloy composition towards the Mg-Al eutectic point. Consequently, the alloy samples with high levels of β-phase would be expected to be easily castable. A detailed experimental study (e.g., using a fluidity spiral) would be necessary to quantify this effect.

4.1.3 Effect of Al-SiC on hardness

It was expected that the hardness would increase with a decrease in the alloy's grain size. The mechanism for increasing hardness with the decreasing grain size has been discussed in Section 2.9. The results of macro-hardness measurement in the interior and wall region of the studied alloys are plotted in Figure 29. Error bars in Figure 29 represent the 95% confidence interval.

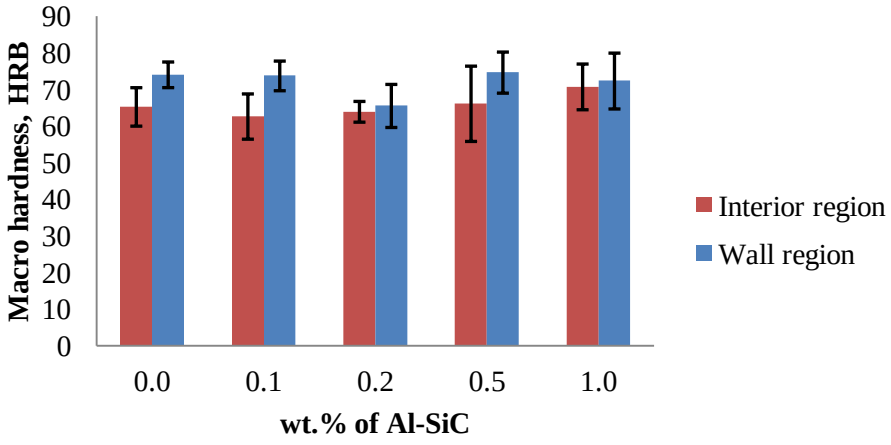

Figure 29: Average hardness of grain refined alloys

The results suggest that hardness in the wall region was higher than in interior region for each casting trial. The grain size variation between interior region and wall region was due to the difference in the alloy's cooling rate. During solidification of the studied alloys, the cooling rate in the wall region was much higher than interior region due to the excellent contact between liquid metal and the mold wall. The high cooling rate locally contributed to additional grain refinement of the alloy.

As shown in Figure 29, adding Al-SiC had no significant influence on the interior and wall hardness of the novel alloys. As the grain size became larger at higher wt.% of Al-SiC (0.2 to 1 wt.%), it was expected the hardness would decrease. However, as proposed in the previous section, the volume fraction of the hard and brittle β-phase in the grain refined alloy increased with increasing amount of Al-SiC. As the β-phase is harder than α-Mg, the size, shape and morphology of β-phase had significant influence on hardness. As a result, the softening due to grain size increase was likely counteracted by increased precipitation of β-phase, causing the hardness to remain unchanged.

4.1.4 Effect of Al-SiC on porosity

Porosity is an unwanted defect in castings. Past study suggested that either dissolved gas or solidification shrinkage causes the formation of microporosity in castings [45]. In the current research, all the porosities were found in the interdendritic regions of the studied alloys, suggesting that the porosity was caused by solidification shrinkage. The micrographs of interdendritic porosity are shown in Figure 30 for three alloy compositions. A summary of the mean area percentage of porosity for each addition level of grain refiner is shown in Table 17. From the paired *t*-test, it was concluded that there was no statistical difference in the mean area percentage of porosity between the repeat casting conditions of Trial 1 and Trial 2 (detailed calculation is presented in Appendix E).

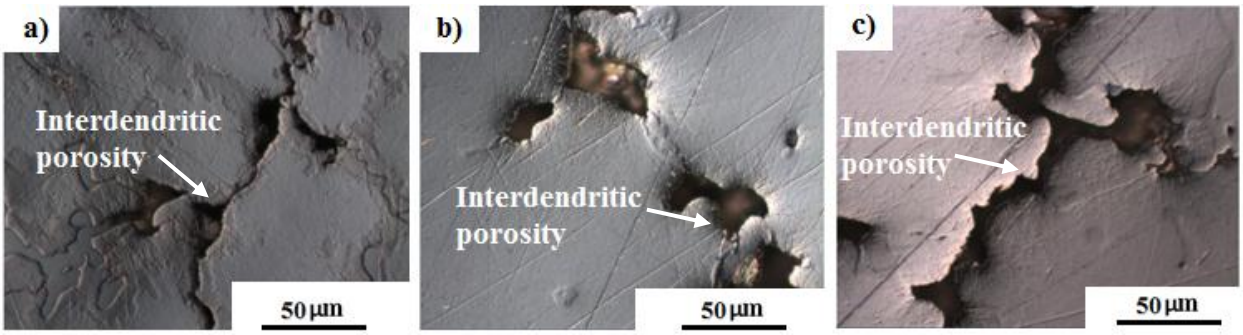

Figure 30: Interdendritc porosity AZ91E alloys: a) Without Al- SiC; b) 0.1 wt.% Al-SiC; c) 0.2 wt.% Al-SiC

Table 17: Mean area percentage of interdendritic porosity of grain refined alloys

wt.% Al-SiC	Mean area % of porosity		
	Trial 1	Trial 2	Grand average
0	2.0 ± 0.5	1.8 ± 0.5	1.9 ± 0.5
0.1	1.8 ± 0.4	1.9 ± 0.5	1.9 ± 0.5
0.2	3.1 ± 0.6	3.0 ± 0.5	3.0 ± 0.6
0.5	3.0 ± 0.4	2.9 ± 0.3	2.9 ± 0.4
1	2.8 ± 0.7	2.8 ± 0.5	2.8 ± 0.6

Based on Table 16, single factor ANOVA analysis was performed (details in Appendix E) and concluded that varying the amount of Al-SiC grain refiner had a statistically significant effect on the mean area percentage of porosity. The final mean area percentage of porosity of the grain refined AZ91E alloy is shown in Figure 31. Error bars in Figure 31 represent the 95% confidence interval.

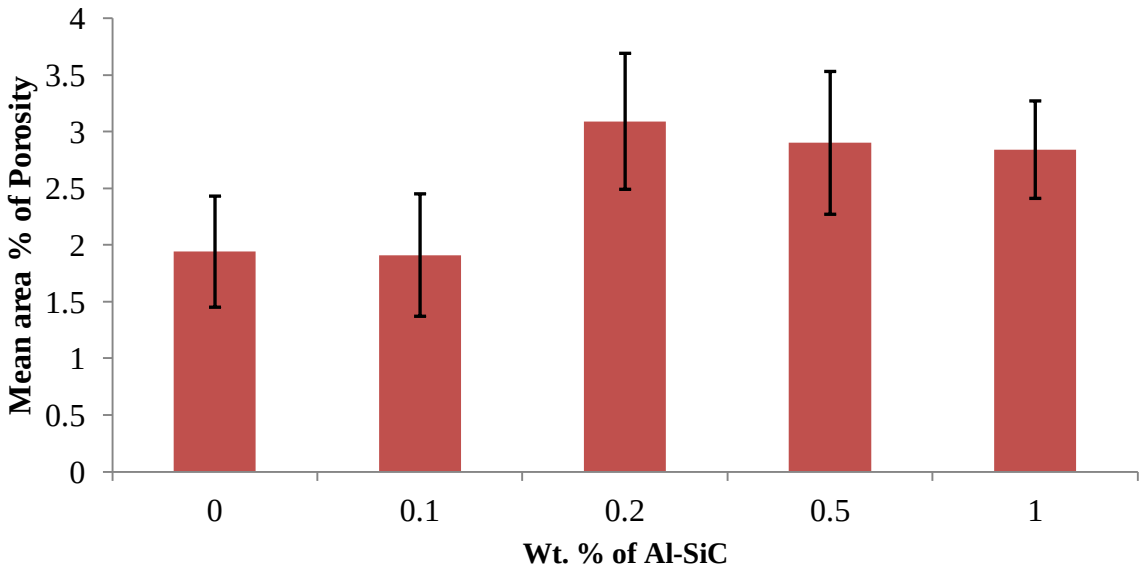

Figure 31: Mean area percentage of interdendritic porosity in AZ91E alloy and grain refined alloys

According to the Mg-Al phase diagram (Figure 2), a higher concentration of aluminum in the Mg-Al alloys results in a larger freezing range. As discussed in Section 4.1.2, the aluminum

concentration in the interdendritic region of grain refined alloys increased with increasing amount of Al-SiC. As a result, the freezing range also increased in the interdendritic region with the increased amount of Al-SiC. Consequently, the interdendritic regions remained in the semi-solid region for a longer period of time. It is established [69], that feeding of semi-solid material is significantly more difficult than feeding of pure metal or a eutectic alloy. Consequently, materials in semi-solid state often exhibit higher levels of shrinkage porosity.

In addition to the increasing freezing range with increasing Al-SiC content, the addition of the grain refiner also caused an increase of grain size (see Figure 25). The trend observed with porosity measurements closely follows that of grain size measurements, suggesting that as the grain size decreased (for 0.1 wt.% Al-SiC) the interdendritic network became more homogeneous. As a result, feeding of the shrinking alloy was relatively easy and the volume of shrinkage porosity decreased. In contrast, as the grain size increased with increasing Al-SiC additions (more than 0.1 wt.% Al-SiC) the interdendritic network became more fragmented as a result of the larger grain size. Consequently, feeding of the interdendritic regions was difficult and the shrinkage porosity formed.

4.1.5 Effect of Al-SiC on solidus and liquidus temperature and enthalpy of liquidus reaction

The solidus, T_S, and liquidus, T_L, temperatures of the base alloy and grain refined AZ91E alloy are provided in Table 18. According to Avedesian and Baker [3], the equilibrium solidus and liquidus temperatures of the AZ91E alloy without any treatment are 468 °C and 598 °C. However, as shown in Table 18, the solidus and liquidus temperatures of the AZ91E alloy without any treatment were 429.1 °C and 588.9 °C, respectively. The difference in the solidus and the liquidus temperature of AZ91E alloy in the current research compared that of equilibrium condition were possibly due to the difference in cooling rate. In the current research, DSC measurements were carried out at the cooling rate of 20 °C/min, which was much higher than the equilibrium conditions used for phase diagram calculation.

Table 18: Solidus and liquidus temperatures and enthalpy of liquidus reaction of selected alloys

Adition level, wt.%		Solidus, tepmerature, °C	Liquidus temperature, °C	Ethalpy of liquidus reaction J/g (area under peak # 2, endothermic)
0	Heating	432.0	593.8	
	Cooling	426.3	584.0	
	Average	429.1	588.9	
0.1	Heating	436.0	597.9	309.5
	Cooling	421.9	580.7	
	Average	428.5	589.3	
0.2	Heating	433.9	594.4	
	Cooling	421.4	581.0	
	Average	427.6	587.7	
0.5	Heating	431.3	590.7	
	Cooling	426.0	582.4	
	Average	428.6	586.5	
1	Heating	439.3	596.7	198.9
	Cooling	421.9	582.5	
	Average	430.6	589.6	

It was found that the addition of Al-SiC had negligible influence on the solidus and liquidus temperature of the studied alloys. The fraction of solid, f_S, was determined using Equation 12 [70]. The fraction of solid, f_S, curves of the experimental alloys within the freezing range (T_s-T_L) are shown in Figure 32.

$$f_S = \frac{T_L - T + \frac{2}{\pi}(T_S - T_L)\left\{1 - Cos\left[\frac{\pi(T - T_L)}{2(T_S - T_L)}\right]\right\}}{(T_L - T_S)\left(1 - \frac{2}{\pi}\right)} \quad (12)$$

where,

T= Temperature of interest within the freezing range, $(T_S - T_L)$

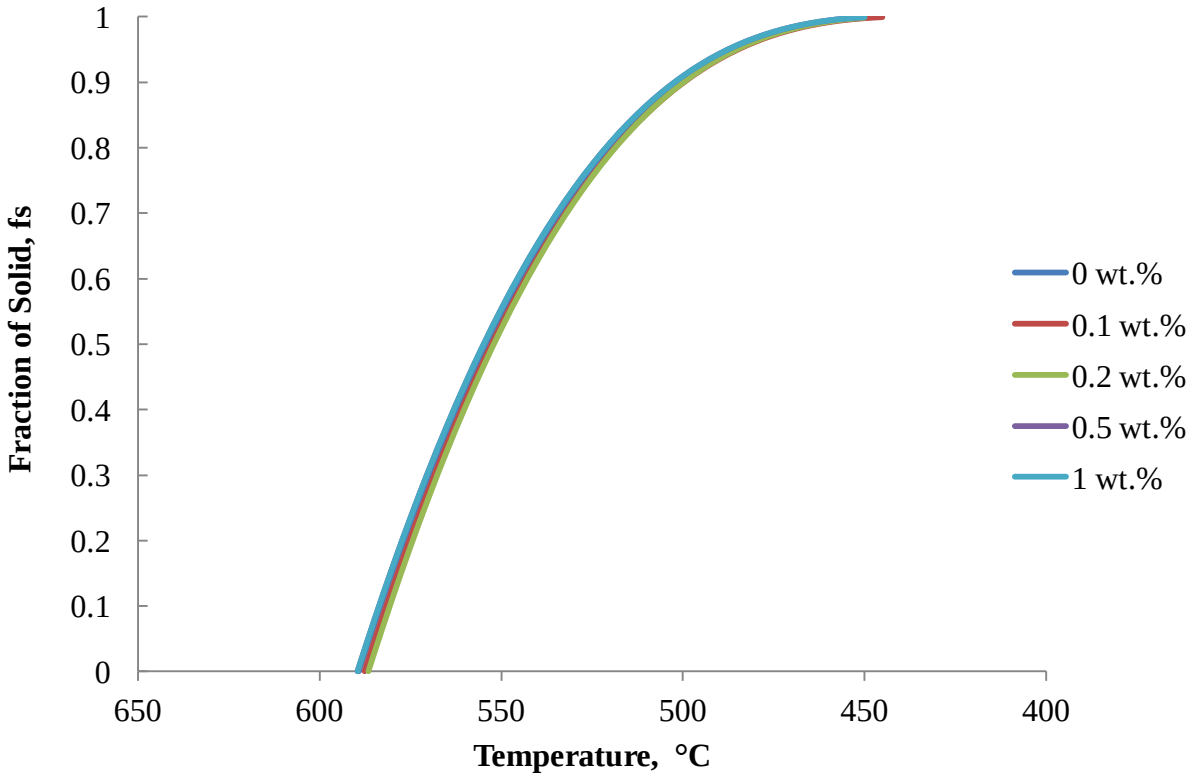

Figure 32: Fraction of solid versus temperature

According to Equation 12, the fraction of solid of studied alloys for any temperature of interest, T, depends on the freezing range,$(T_S - T_L)$. As the solidus and liquidus temperatures were almost same for each alloy composition, there was no significant difference in the development of fraction of solid of the studied alloys. This observation suggests that the grain refinement effect observed for 0.1 wt.% Al-SiC was likely not the result of the cooling rate effect. Instead, the reduction of grain size was possibly related to the microstructural refinement by heterogeneous nucleation. This hypothesis is supported by quantitative evaluation of the enthalpy of nucleation using DSC.

As shown in the DSC curves of Figure 33 and Figure 34, the area under the liquidus curve (peak # 2, endothermic) represents the enthalpy of liquidus reaction. This enthalpy depends on the number of grains present during the initial stage of casting solidification. As shown in Table 18, the enthalpy of liquidus reaction was higher with the addition of 0.1 wt.% Al-SiC compared to

that of 1 wt.% Al-SiC. Higher enthalpy of liquidus reaction indicated that a greater number of grains were present in the grain refined alloy at the liquidus temperature.

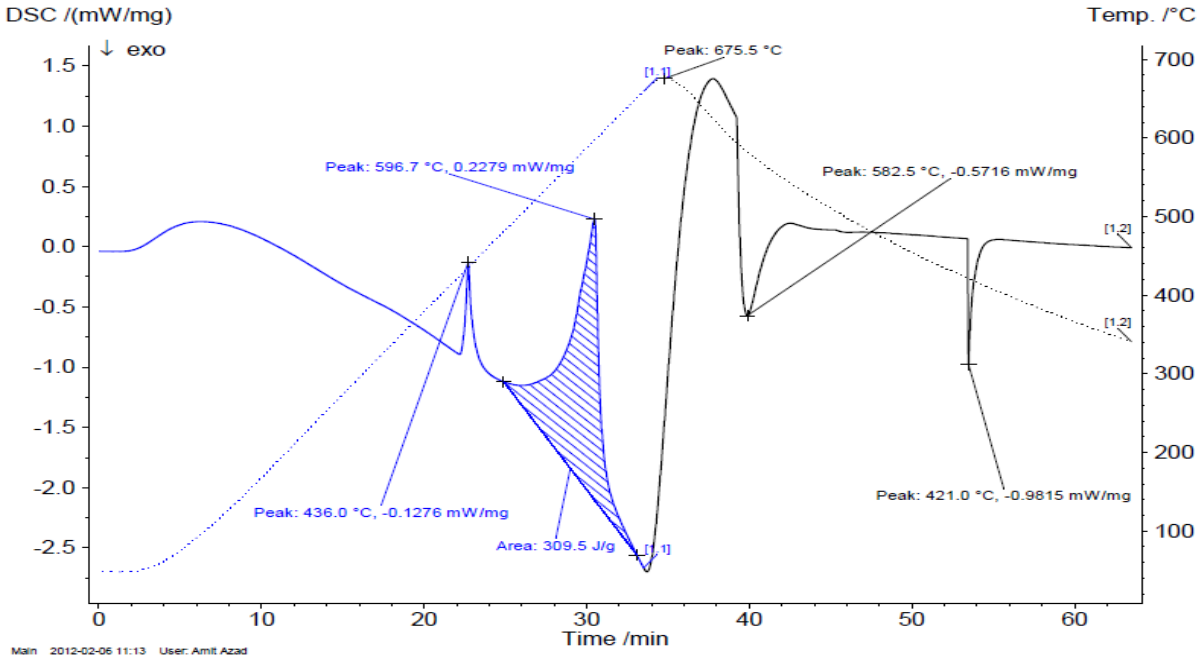

Figure 33: DSC curve of AZ91E alloy with the addition of 0.1 wt.% Al-SiC

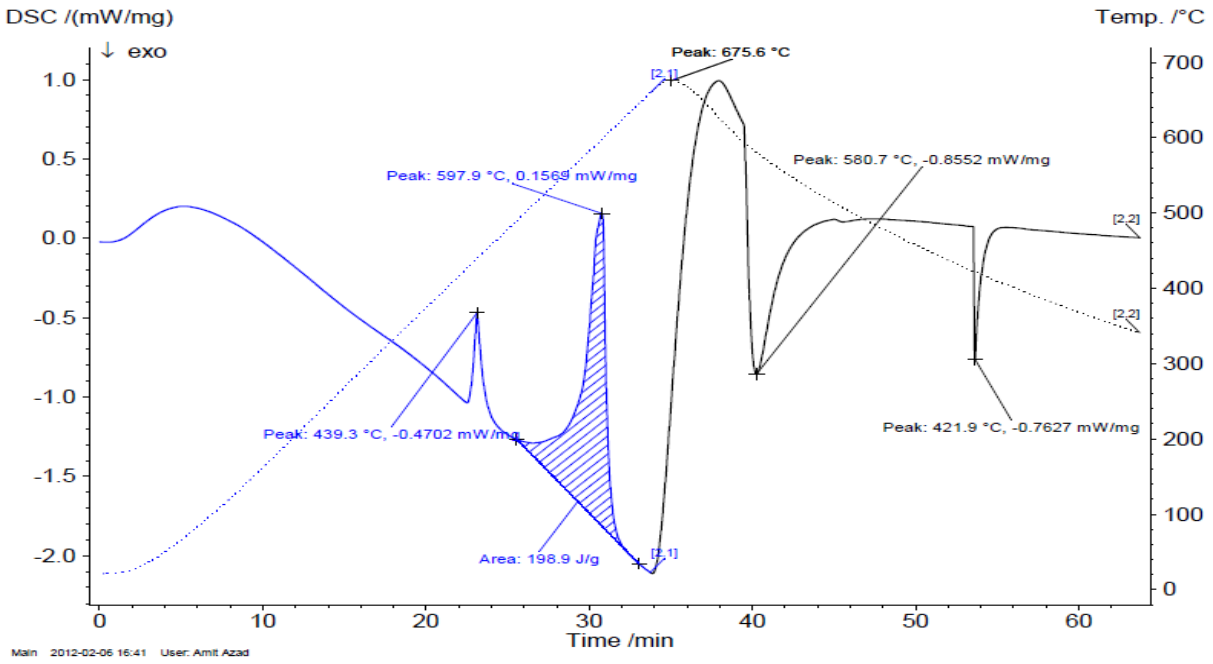

Figure 34: DSC curve of AZ91E alloy with the addition of 1 wt.% Al-SiC

4.2 Microstructure analysis of Al-SiC master alloy and grain refined alloys

4.2.1 Microstructure of Al-SiC master alloy

A representative micrograph of the Al-SiC grain refiner master alloy is shown in Figure 35. The result of chemical analysis on the features indicated in Figure 35 is provided in Table 19. According to Table 19, Feature # 1, 2 and 3 in Figure 35 contained Si and C with the average ratio of Si:C of 1.67, where the average wt.% of C was 37.18%. As shown in the binary phase diagram of Si-C in Figure 36, 37.18 wt.% C corresponds to the SiC particle stoichiometry. As a result, it can be concluded that the Feature # 1, 2 and 3 were the SiC particles and the size of the SiC particles varied from 3 to 10 µm**.** Feature # 4 and 5 in Figure 35 contained Al, with trace of Si and C. Thus, it is possible that Si and C have diffused from the SiC particles into the Al matrix during SPS processing. However, due to the thermal stability of SiC, the matrix was maintained mainly as Al.

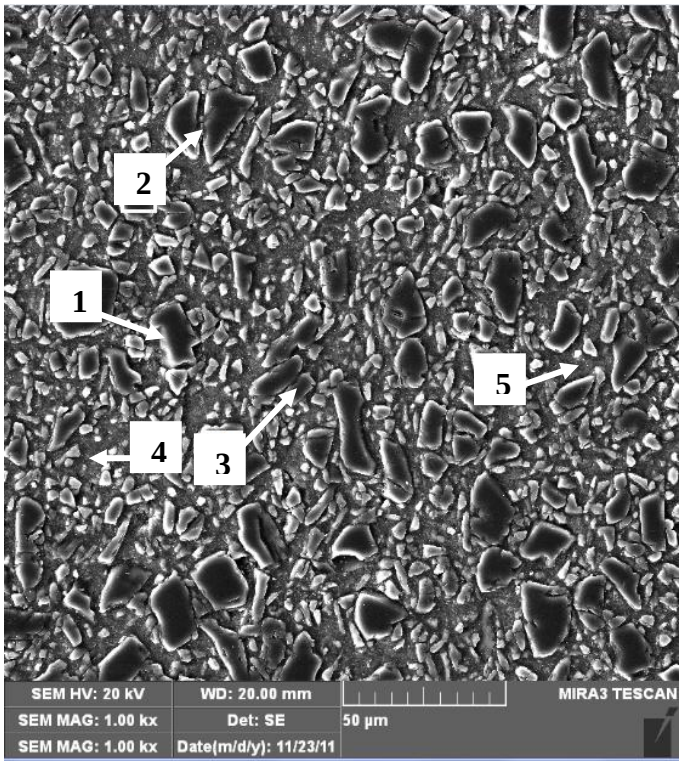

Figure 35: Microstructure of Al-SiC master alloy

Table 19: XEDS analysis of Al-SiC master alloy

	wt.%			
Feature	**C**	**Al**	**Si**	**Total**
1	36.8	0.4	62.8	100
2	36.3	0.8	62.9	100
3	38.4	0.6	60.0	100
4	9.5	90.1	0.4	100
5	8.0	89.5	2.5	100

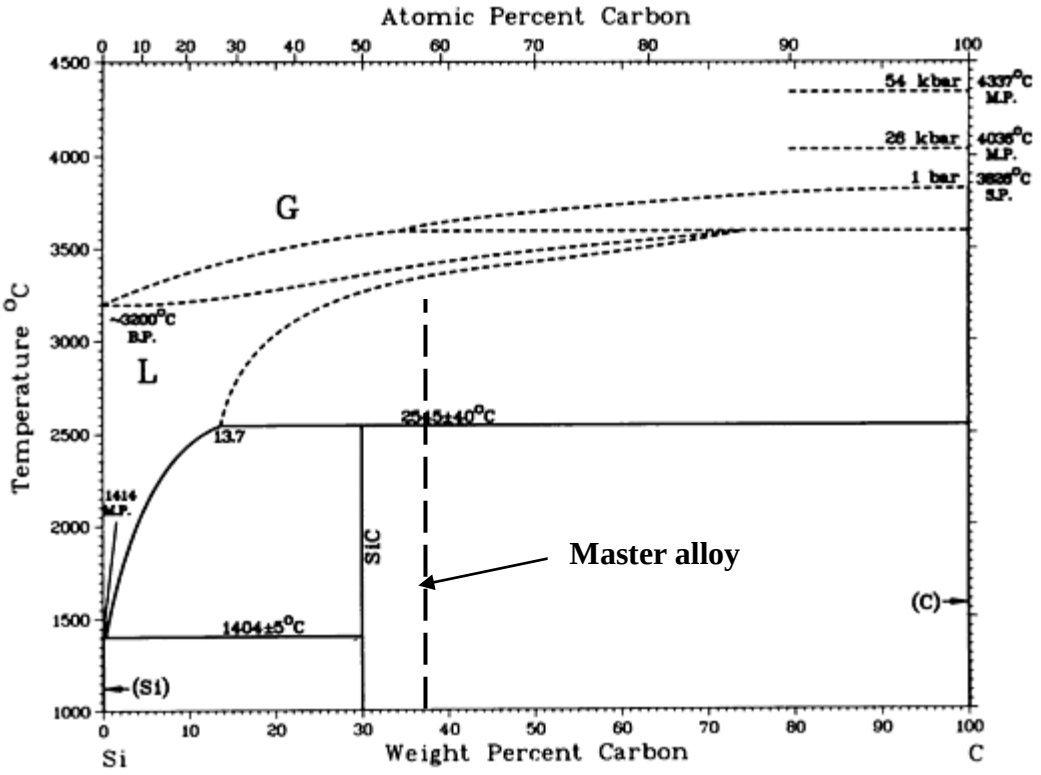

Figure 36: Si-C equilibrium binary phase diagram [30]

4.2.2 Microstructure of grain-refined AZ91E alloys

X-ray XEDS maps were obtained to study the distribution of elements in the AZ91E alloy treated with Al-SiC. Figure 37a, shows a secondary electron (SE) image of a grain of AZ91E alloy with 0.1 wt.% Al-SiC. As shown in Figure 37 b, lower concentration of Mg was found in the grain boundary (interdendritic region) compared to that of inside the grain. Because of the higher concentration of aluminum at the grain boundary of Figure 37c, it can be concluded that the aluminum was rejected by the α-Mg dendrite during solidification. According to Figure 37d, Si was found in only two locations of the interdendritic region. The Si rich regions had the same shape as SiC particles seen in the Al-SiC master alloy (e.g., Figure 35). As a result, the Si rich regions in the grain boundaries were assumed to be Si rich particles originating from the Al-SiC

master alloy. As shown in Figure 37e, Zn was uniformly distributed in the α-Mg, since Zn forms a solid solution with Mg [30]. Possible presence of localized oxide inclusions was found along the grain boundary. The general microstructure of each alloy composition is illustrated in Figure 38.

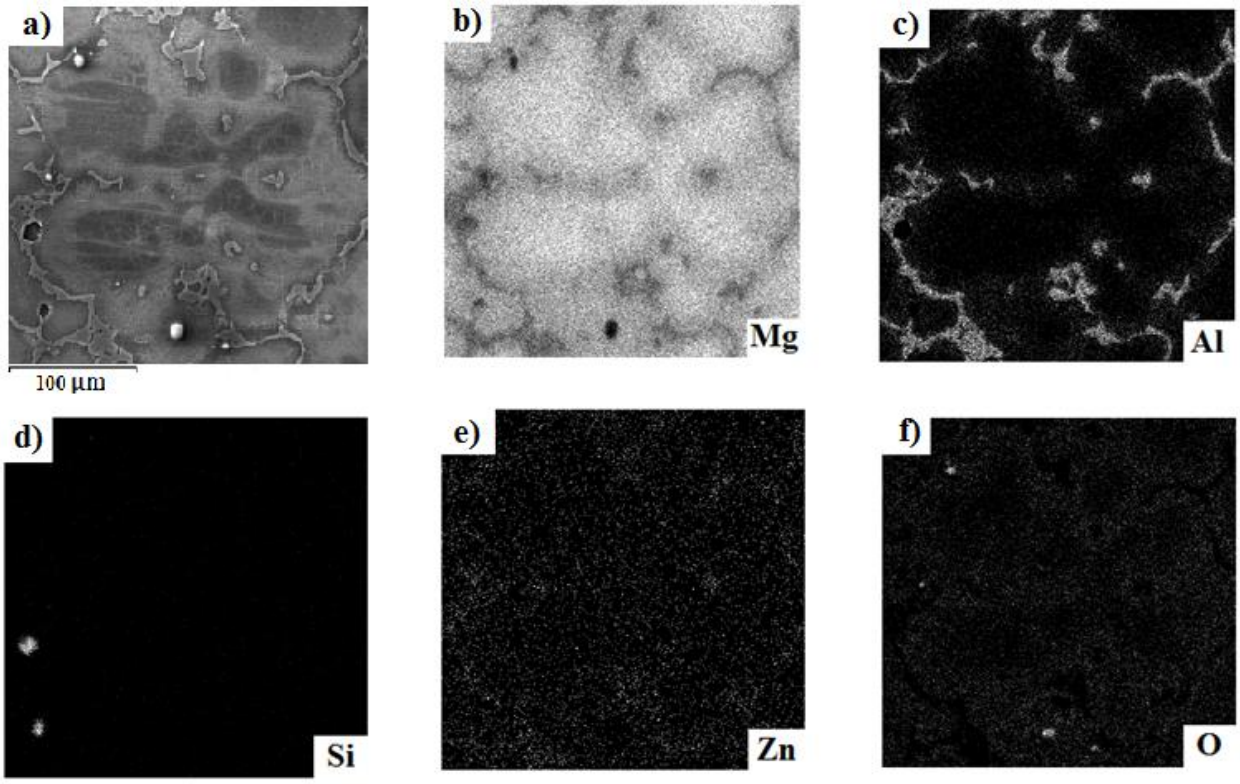

Figure 37: X-ray maps for grain refined (AZ91E+ 0.1 wt.% Al-SiC alloy): a) SEM image; b) Mg; c)Al; d) Si; e) Al; f) Zn

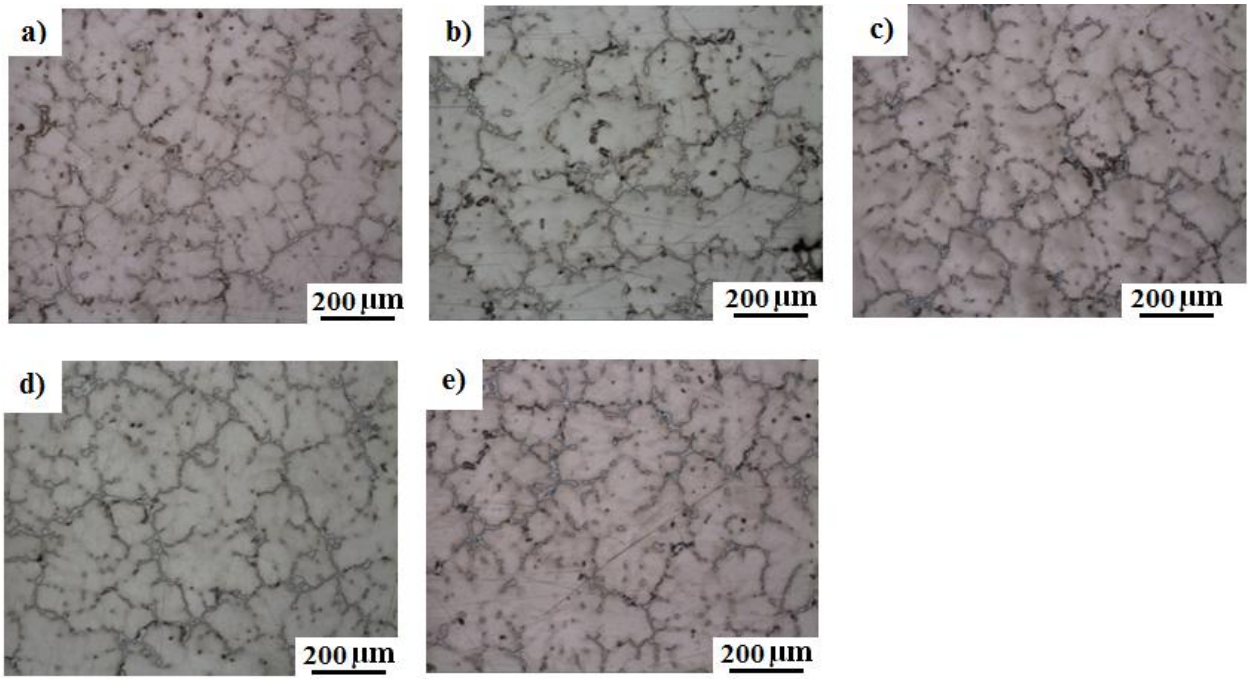

Figure 38: General microstructure of each alloy composition: a) Without Al-SiC; b) 0.1 wt.% Al-SiC; c) 0.2 wt.% Al-SiC; d) 0.5 wt.% Al-SiC; e) 1 wt.% Al-SiC

An XEDS analysis was conducted in the interdendritic region of Figure 39. Table 20 provides the chemical composition (wt.%) of the features in Figure 39. The results in Table 20 suggested that Feature # 1 in Figure 39 was a void previously filled with a SiC particle which was likely removed during sample polishing. Feature # 2 in Figure 39 was found to be a SiC particle embedded at the grain boundary. Figure 40 also shows the morphology of a SiC paticle embedded in the interdendritic region.

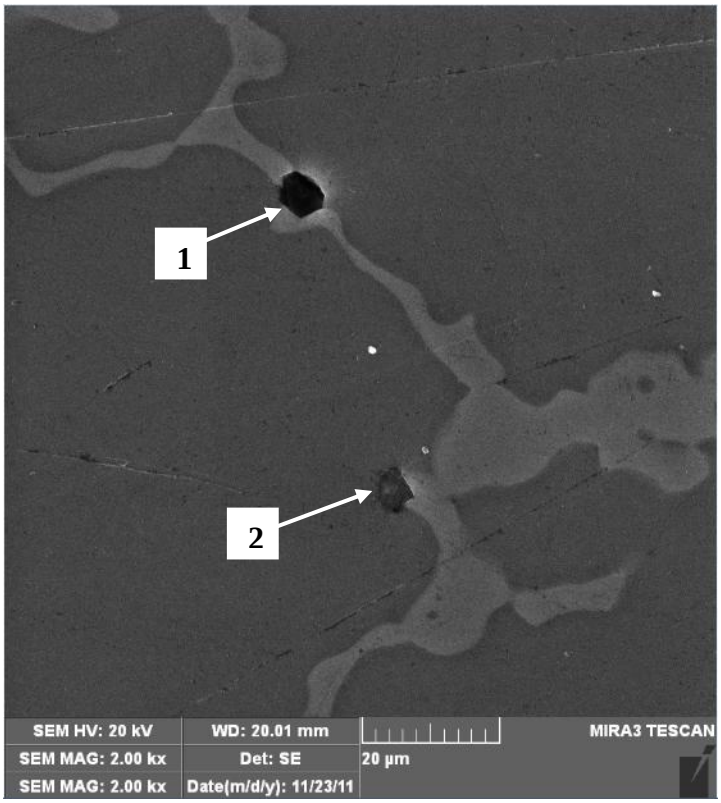

Figure 39: SE image of interdendritic region of AZ91E alloy with 0.1 wt.% Al-SiC

Table 20: XEDS analysis of features in Figure 39

	wt.%			
Feature	**C**	**Mg**	**Al**	**Si**
1	6.9	77.3	4.9	10.9
2	11.1	65.7		23.1

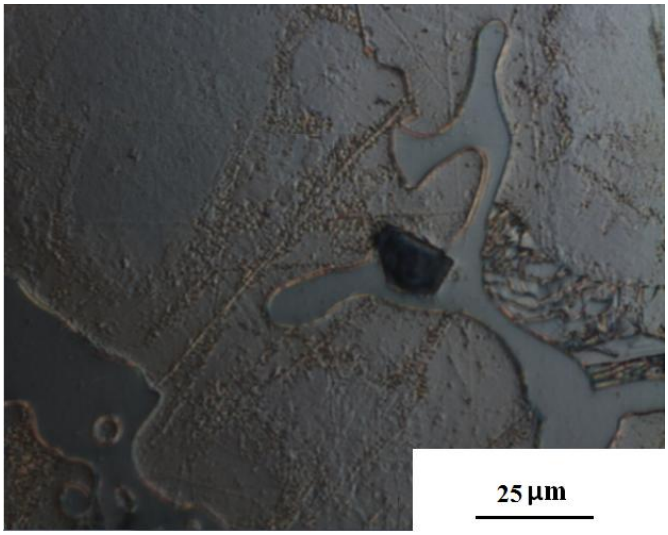

Figure 40: Optical micrograph of interdendritic region of AZ91E alloy with 0.1 wt.% Al-SiC

4.2.3 Grain refinement mechanisms

As suggested by the literature review, both heterogeneous nucleation and growth restriction of grains may possibly influence the grain growth in Mg-Al alloys refined by SiC.

4.2.3.1 Heterogeneous nucleation

SEM micrographs of AZ91E alloy with 0.1 wt.% Al-SiC are shown in Figure 41 and Figure 42. The XEDS chemical analysis of features indicated in these figures is presented in Table 21 and Table 22, respectively. According to the XEDS results, all the features in Figure 41 and the Feature # 1, 2, 3 and 5 in Figure 42 were mainly Al-Mn particles. These particles are commonly present in the AZ91E alloy. The presence of Mg was attributed to the signal originating from the matrix and the wt.% of C and Si was very low. In order to determine the stoichiometry of the Al-Mn particles, a binary alloy system of Al and Mn was considered. The reduced average compositions of Al and Mn for the features in Figure 41 and the Feature #1, 2, 3 and 5 in Figure 42 were 37.4 wt.% Al and 62.6 wt.% Mn. According to the Al-Mn phase diagram, Figure 43, at

any temperature below 900 °C, the composition of the particles was in the γ_2-phase. The crystal structure of the γ_2-phase was described as cubic (bcc or fcc) or rhombohedral [30].

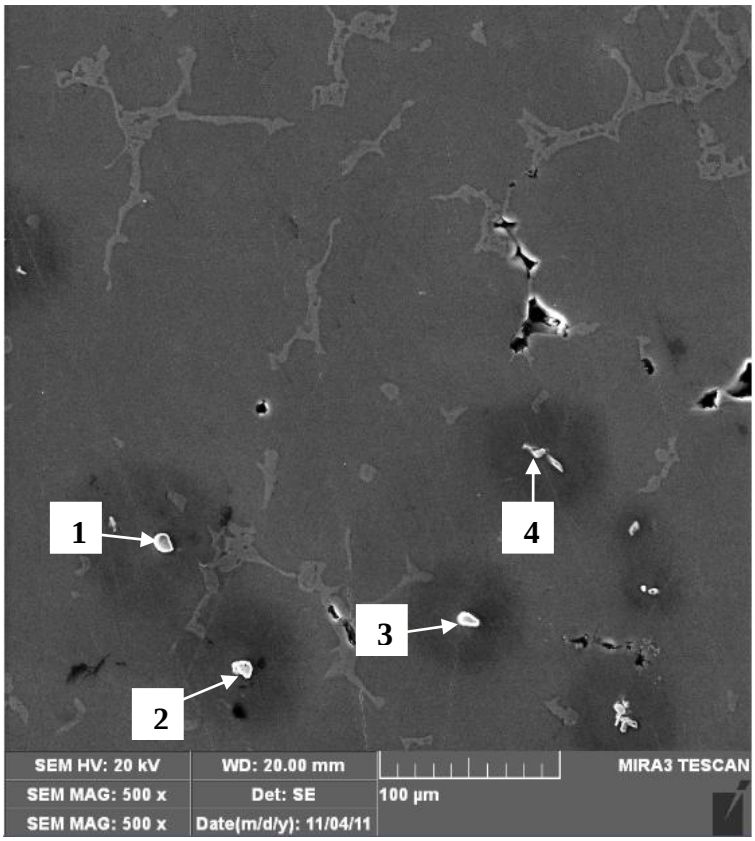

Figure 41: Microstructure of AZ91E alloy with 0.1wt.% Al-SiC for location A

Table 21: XEDS analysis of features in Figure 41

Feature	wt.%					at.%				
	Mn	Al	Mg	C	Si	Mn	Al	Mg	C	Si
1	51.5	28.1	16.4	3.2	0.8	32.4	46.4	13.3	6.8	1.1
2	53.0	29.2	14.8	2.1	0.9	26.9	55.3	11.5	5.3	0.9
3	49.7	32.7	13.1	3.7	0.8	19.1	59.4	16.4	4.1	0.9
4	52.0	33.8	10.2	3.7	0.9	24.6	57.9	11.3	5.2	0.9

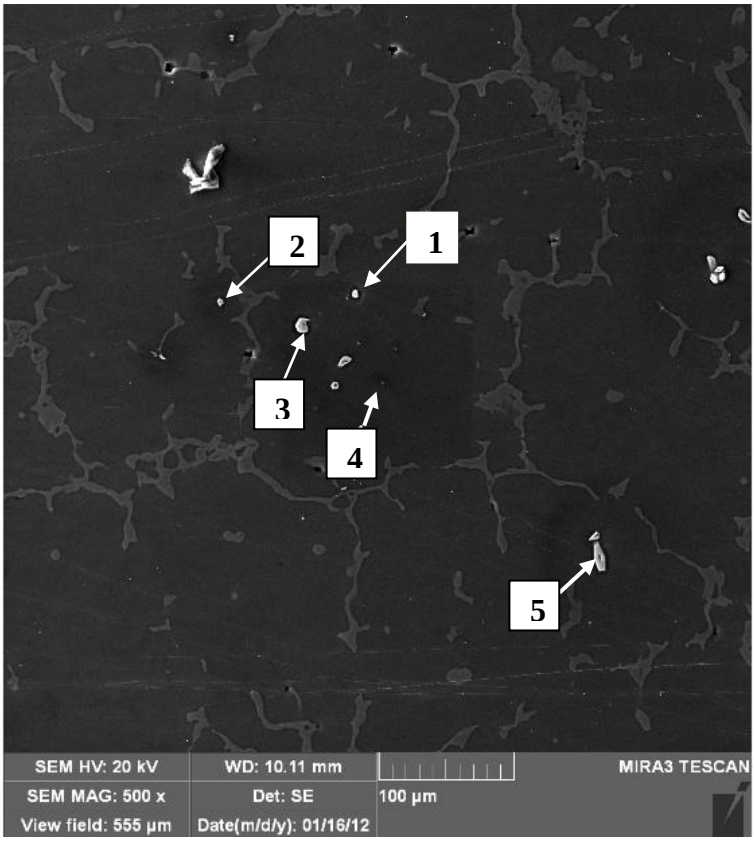

Figure 42: Microstructure of AZ91E alloy with 0.1wt.% Al-SiC for location B

Table 22: XEDS analysis of features in Figure 42

Feature	wt.%					at.%				
	Mn	Al	Mg	C	Si	Mn	Al	Mg	C	Si
1	53.2	33.2	9.5	3.3	0.9	33.5	49.1	11.4	4.98	0.1
2	60.7	32.3	3.4	2.8	0.9	35.1	45.9	14.2	3.69	1.0
3	50.3	30.8	15.6	2.7	0.6	32.1	51.3	10.5	5.39	0.8
4			39.4	60.5				73.9	26.14	
5	50.2	30.9	14.7	3.4	0.8	22.2	55.3	15.2	6.39	0.9

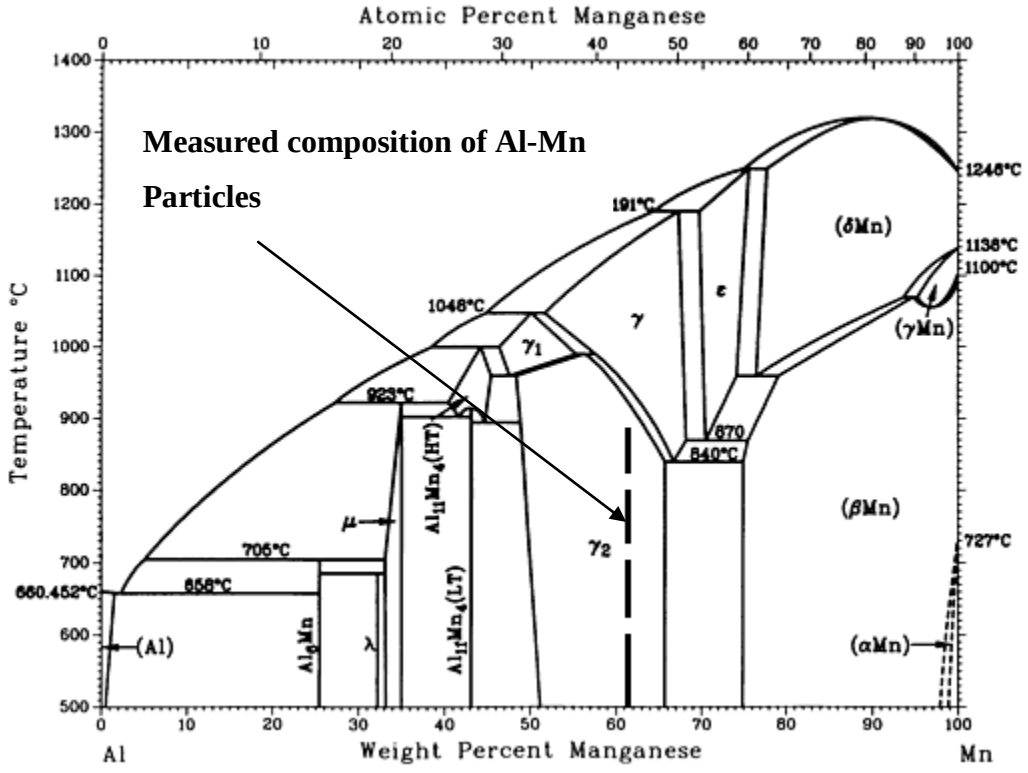

Figure 43: Al-Mn binary phase diagram [30]

Because of dissimilarity in the crystal structure between γ_2-phase and α-Mg (HCP structure). The intermetallic compound of γ_2-phase was unlikely an effective nucleating substrate. As a result, the grain structure was examined to seek any potential nucleating particle in the grain interior. As shown in Table 22 (Feature # 4), a new intermetallic compound of Mg-C was discovered near the middle of a grain (particle 4, Figure 42) of the studied alloy treated with 0.1 wt.% Al-SiC. Several other Mg-C particles were also seen in Figure 44. Table 23 provides the XEDS results for the particles indicated in Figure 44. The Mg and C had an average composition of 32.64 at.% Mg and 67.4 at.% C. According to Mg-C phase diagram, Figure 45 at any temperature below 1000 °C, the Mg-C alloy system (32.64 at.% Mg and 67.4 at.% C) lies in the magnesium carbide region. As a result, it can be concluded that the intermetallic compound was magnesium carbide. A higher magnification of the MgC (particle 1- Figure 44) is shown in Figure 46.

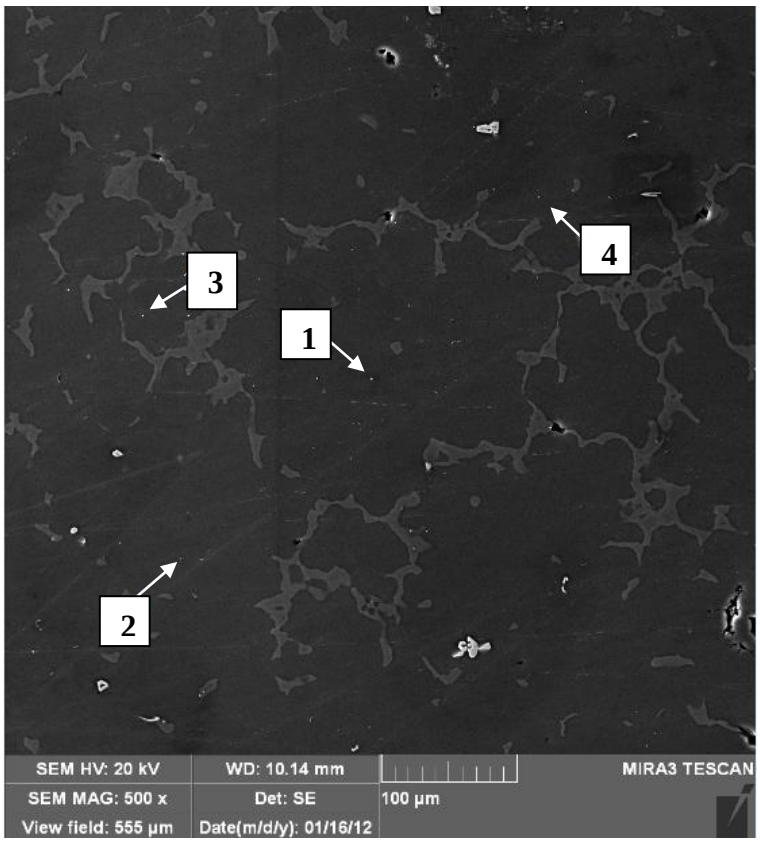

Figure 44: Microstructure of AZ91E alloy with 0.1wt.% Al-SiC, showing heterogeneous nuclei substrates

Table 23: XEDS analysis of features in Figure 46

Feature	wt.%		at.%	
	C	Mg	C	Mg
1	55.7	45.3	60.7	39.2
2	56.9	43.1	60.5	39.4
3	56.9	43.1	72.8	27.1
4	60.3	39.7	75.4	24.6

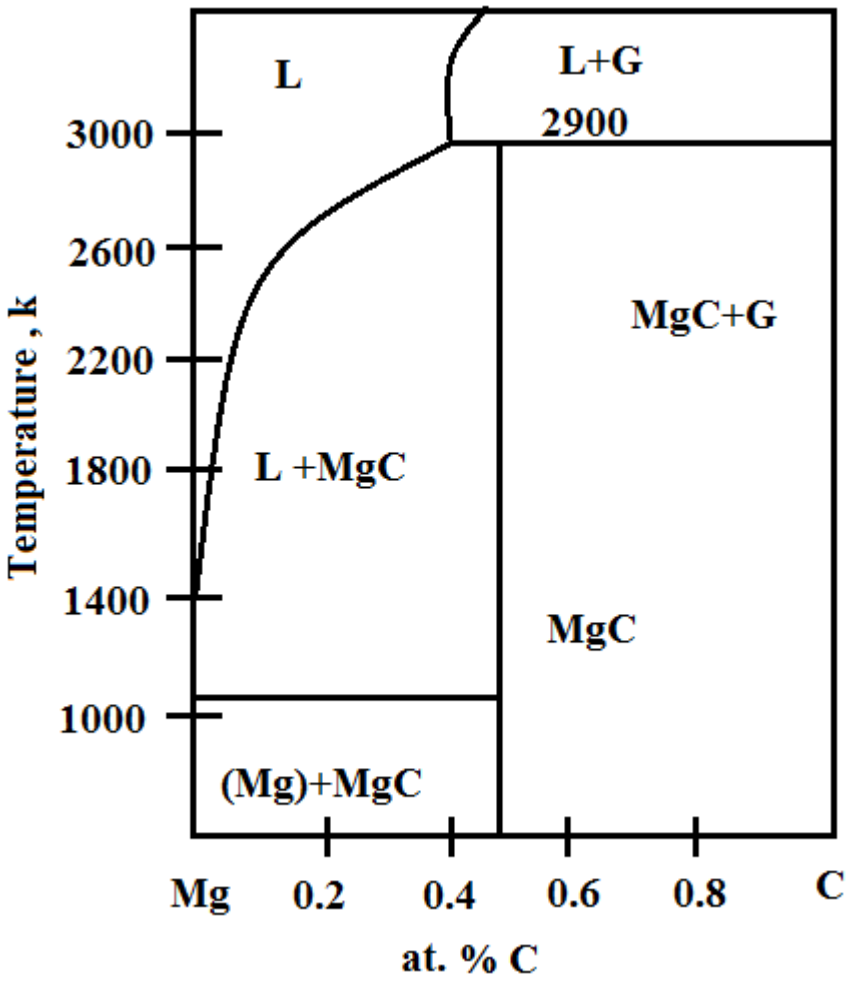

Figure 45: Mg-C binary phase diagram [71]

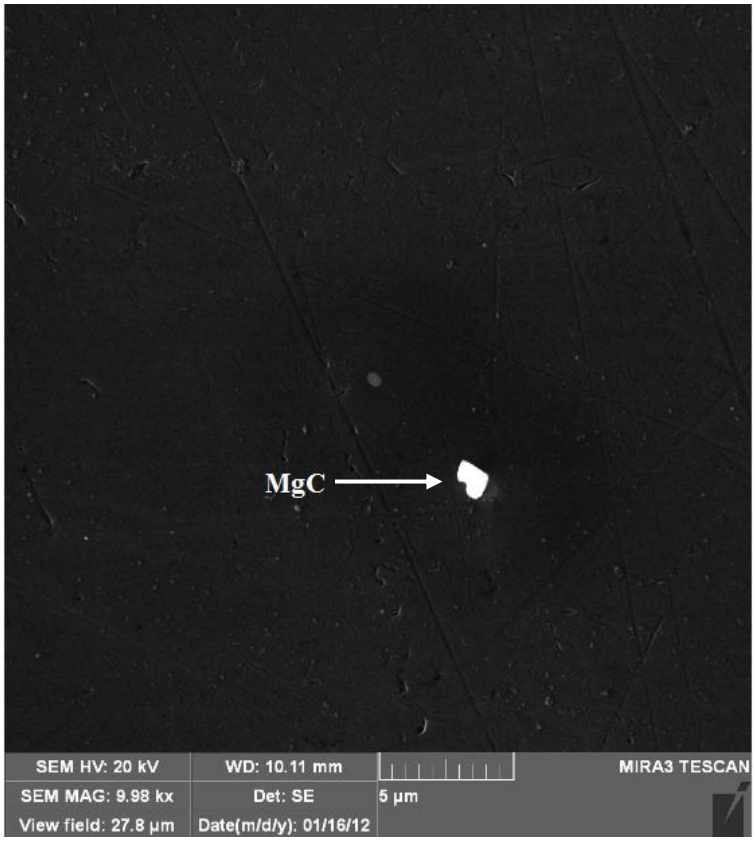

Figure 46: MgC (particle 1- Figure 44) at higher magnification

The crystal structure of MgC is tetragonal and lattice parameters are a= 0.486 nm c= 0.567 nm [72]. The hexagonal close packed α-Mg has good wetability with the tetragonal MgC, because of the similarity in lattice parameter c (Mg, c= 0.521). The good wetability of MgC and α-Mg decreased the wetting angle, θ. As a result, the MgC possibly acted as effective nucleus for α-Mg grains and enabled heterogeneous nucleation. Because of these active heterogeneous nuclei, a greater number of grains formed with the addition of 0.1 wt.% Al-SiC into the AZ91E alloy.

According to the XEDS results in Table 21 and Table 22, a lower concentration of C and Si were found in the Al-Mn intermetallic compound. The presence of Si and C in the Al-Mn particles indicated that some SiC particles reacted with α-Mg at the early stage of solidification formed MgC as suggested by Equation 13.

$$SiC + Mg = MgC + Si \qquad (13)$$

4.2.3.2 Growth restriction effect

As shown in Figure 37c, aluminum was rejected to the interdendritic region during solidification. As discussed in Section 2.8.1.3 (Chapter 2) the growth restriction effect can be quantified by the growth restriction factor (GRF). According to Table 7, the GRF of Al is 4.32 for Mg-1wt.% Al alloy. As a result, increasing the Al concentration via addition of Al-SiC master alloy may have enhanced the growth restriction effect.

An XEDS line analysis was conducted from point A to point B within a representative interdendritic region, as shown in Figure 47. The line was drawn from a center of one grain to the center of neighbouring grain. As shown in Figure 48, concentration of Al increased in the interdendritic region whereas concentration of Mg decreased. As a result, when the two neighbouring grains were growing, the high concentration of Al in the interdendritic region caused eutectic solidification and formed α-Mg and β-phase. Upon reaching the Al concentration of 33 wt.%, the phase composition was β-phase only. As shown in Figure 27, β-phase had a lamellar structure. As a result, the formation of β-phase restricted the α-Mg grain to growth in forward direction and forced the grain to grow in transverse or lateral direction. When the grain started to grow in transverse direction, it slowed down the total grain growth in the natural growth direction.

.

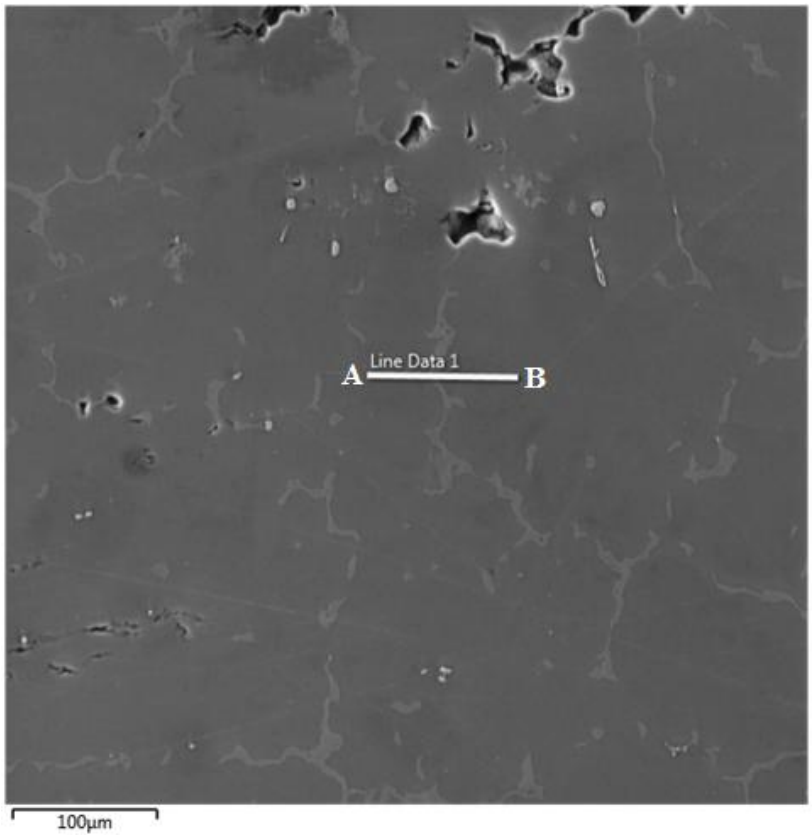

Figure 47: XEDS line scan for AZ91E alloy with 0.1 wt.% Al-SiC

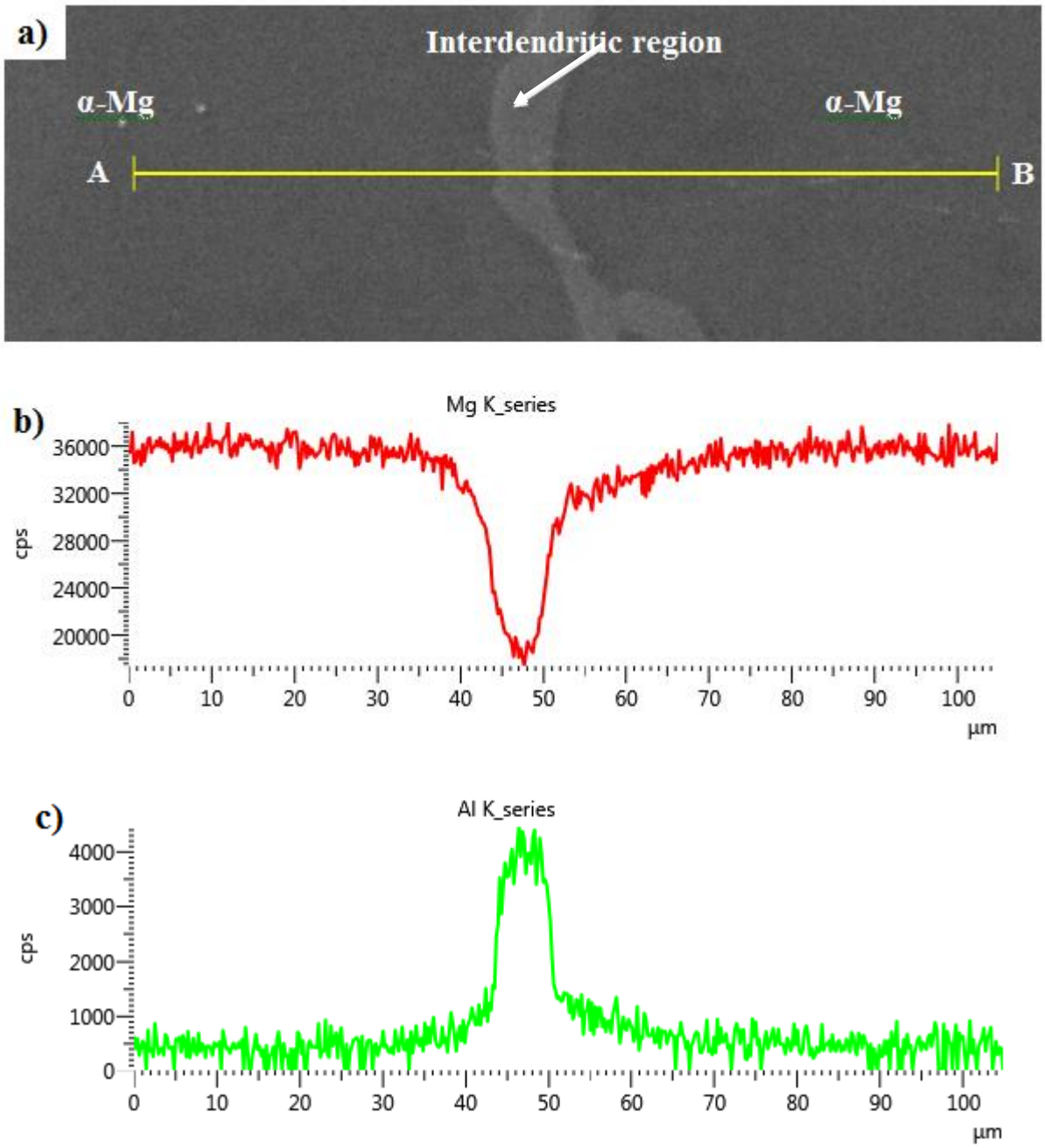

Figure 48: XEDS line scan, showing the comparison of Al and Mg concentration along the line AB

4.2.4 Grain coarsening mechanism

It was expected that increasing levels of Al-SiC would promote additional grain refinement, because of the presence of more heterogeneous nuclei (MgC). However, as shown in Figure 25, increasing the wt.% of Al-SiC above the 0.1 wt.% level increased the grain size.

Ineffective nucleant substrate such as $AlCMn_3$ intermetallic compound was possibly formed with the increased amount of Al-SiC exceeding 0.1 wt.% Al-SiC. $AlCMn_3$ has poor wetability with α-Mg due to its FCC crystal structure [73]. Direct reaction of Al, C and Mn or C and Al-Mn particle could possibly form $AlCMn_3$. As shown in the Al-Mn-C ternary phase diagram, Figure 49, $AlCMn_3$ forms with 60 at.% Al, 20 at.% Mn and 20 at.% C. Formation of $AlCMn_3$ compounds would inhibit formation of MgC heterogeneous nucleant substrates. To verify this theory, XEDS analysis on Al-C-Mn particles was carried out.

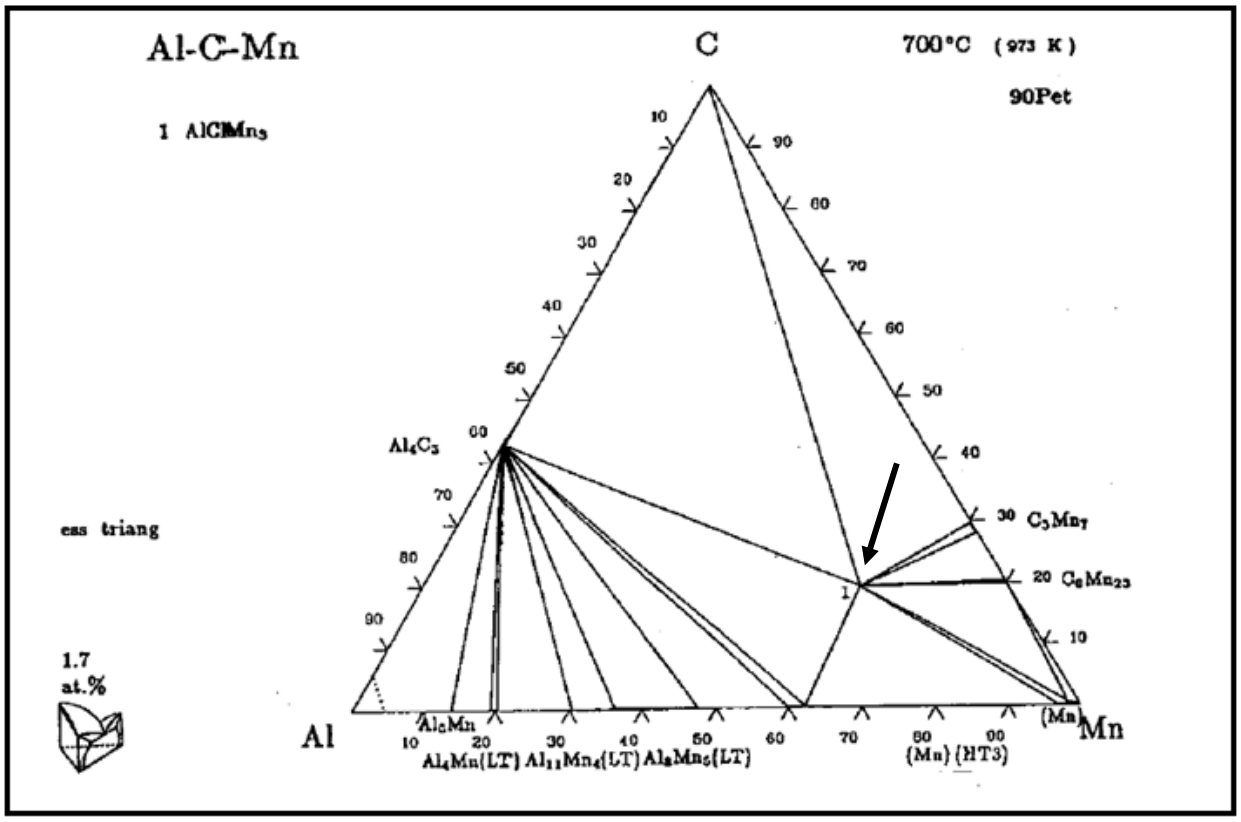

Figure 49: Al-Mn-C ternary phase diagram [74]

The XEDS results (at.%) of features in Figure 41 and Feature # 1, 2, 3 and 5 in Figure 42 are provided in Table 21 and Table 22, respectively. These results are for the 0.1 wt.% Al-SiC alloy. The reduced chemical compositions (at.%) of features in Figure 41 and the Feature # 1, 2, 3 and 5 in Figure 42 are provided in Table 24 and Table 25. The at.% of Al and Mn in are very close to that of Al and Mn in $AlCMn_3$ intermetallic compound. However, at.% of C was possibly not high enough to form $AlCMn_3$. As a result, it is suggested that at this addition level of Al-SiC the grain refiner could not provide sufficient C to form $AlCMn_3$ intermetallic compound.

Table 24: Reduced chemical composition of particles in Figure 41

	at.%		
Feature	**C**	**Al**	**Mn**
1	7.9	54.2	37.9
2	6.0	63.2	30.8
3	5.0	71.9	23.1
4	6.0	66.0	28.0

Table 25: Reduced chemical composition of particles in Figure 42

	at.%		
Feature	**C**	**Al**	**Mn**
1	6.7	56.0	38.3
2	4.3	54.2	41.4
3	6.1	57.2	41.4
5	7.6	65.9	26.5

SEM micrographs of AZ91E alloy with 1 wt.% Al-SiC are shown in Figure 50. The XEDS chemical analysis of features indicated in Figure 50 is presented Table 26. The average at.% of C, Al and Mn in the features in Figure 50 was found 18.42, 46.30 and 35.26 at.%, respectively. Though the at.% of Al was slightly lower and Mn was slightly higher than the composition of Al and Mn in $AlCMn_3$ intermetallic compound, the amount of carbon in these particles nearly tripled. Thus it is believed that with increasing level of Al-SiC addition, the possibility to form $AlCMn_3$ intermetallic compound increased. Formation of $AlCMn_3$ intermetallic compound

possibly decreased the possibility to form MgC heterogeneous nuclei sites, which resulted in grain coarsening. Easton et at. [15] suggested the formation of ineffective nuclei of $AlCMn_3$ intermetallic causes poisoning the grain refinement.

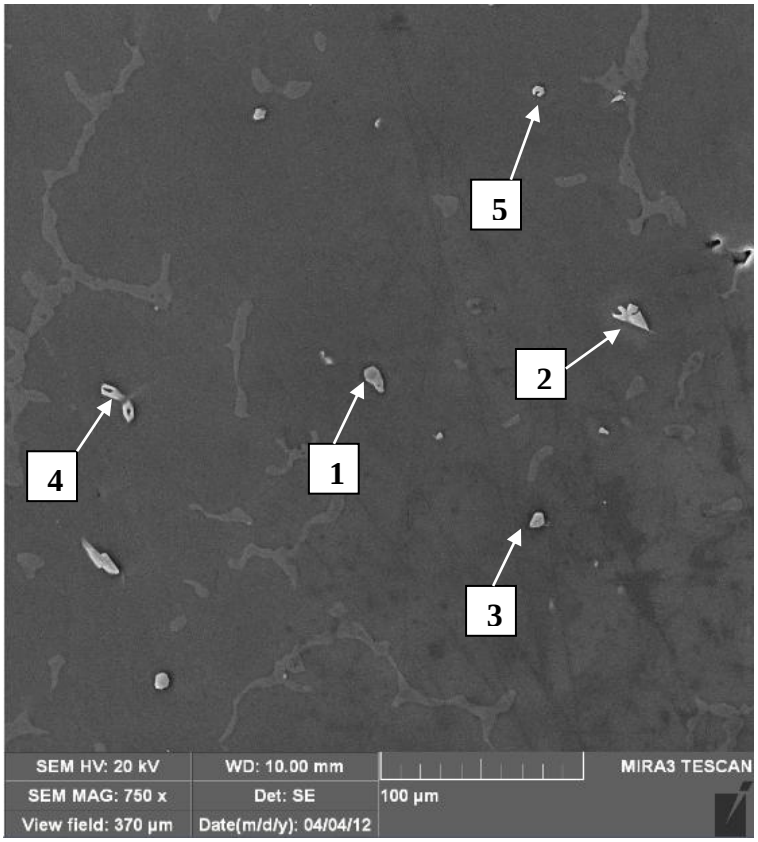

Figure 50: Microstructure of AZ91E alloy with 1 wt.% Al-SiC

Table 26: XEDS analysis of features in Figure 50

	at.%		
Feature	**C**	**Al**	**Mn**
1	20.2	44.8	35.0
2	19.2	45.6	35.2
3	18.3	47.5	34.2
4	16.3	46.9	36.8
5	18.0	46.8	35.1

5 Conclusions

1. The maximum grain refining efficiency of the novel Al-SiC master alloy was found at the 0.1 wt.% Al-SiC addition level, when mean grain size was reduced to 197.5 ± 4.9 μm from 227.5 ± 5.0 μm. Further addition of the grain refiner (exceeding 0.1 wt.%) resulted in poisoning effect, as the mean grain size increased to 360.9 ± 10.6 μm with the addition of 0.2 wt.% Al-SiC.

2. The SiC particles did not act as the heterogeneous nuclei sites. These particles were pushed to interdendritic regions by α-Mg during dendritic solidification. However, some of the SiC particles reacted with α-Mg and formed MgC nuclei.

3. The grain refinement mechanism was related to heterogeneous nucleation by MgC. The mechanism of formation of heterogeneous nuclei sites was further supported by DSC measurements, as the enthalpy of liquidus reaction of studied alloy with 0.1 wt.% Al-SiC was higher compared to that of an alloy with 1 wt.% Al-SiC.

4. The grain coarsening mechanism was due to the formation of ineffective nuclei $AlCMn_3$. Formation of $AlCMn_3$ has decreased the probability to form effective nuclei substrate of MgC.

5. It was found that increasing the addition level of Al-SiC had an effect on β-phase and porosity. The highest mean area percentage of β-phase was found with the addition of 1 wt.% Al-SiC. This corresponded well with the increasing amount of Al in the refined alloy.

6. The porosities were found as interdendritic shrinkage porosity. The lowest mean area percentage of porosity was found with the addition of 0.1 wt.% Al-SiC, which agreed with the finest alloy grain size.

7. Increasing the addition level of Al-SiC to AZ91E alloy had no influence on hardness.

5.1 Future work

This research provided a fundamental background on the grain refinement of AZ91E alloy with the addition of Al-SiC master alloy. The main focus of this research was reducing the grain size and understanding the mechanism of grain refinement and coarsening. Several investigations should be performed to further expand on this work. For example:

1. As the grain coarsening mechanism was not fully understood with the increased amount of Al-SiC, a Transmission Electron Microscopy (TEM) analysis can be carried out on studied alloys in order to find out the exact crystal structure and lattice parameters of any new intermetallic compounds.

2. As the lowest and highest grain size were achieved at 0.1 wt.% and 0.2 wt.% Al-SiC respectively, it is of interest to investigate whether further reduction or increase in grain size is possible with the addition of Al-SiC between 0 to 0.2 wt.% Al-SiC master alloy.

3. As this research only focused on the addition of Al-SiC master alloy to AZ91E subject to a constant cooling rate, it is of interest to investigate the effect of cooling rate effect on grain size, while maintain the amount of Al-SiC master alloy addition constant.

Bibliography

1. Kulekci, M. K., "Magnesium and its alloys applications in automotive industry", The International Journal of Advanced Manufacturing Technology, Vol. 39, No. 9, pp. 851-865.
2. Davis, J. R., ASM Handbooks Online, & ASM International Handbook Committee, Metals handbook, ASM International, Materials Park, OH, 1998.
3. Avedesian, M. M., Baker, H. and ASM International Handbook Committee, Magnesium and magnesium alloys, ASM International, Materials Park, OH, 1999.
4. Magnesium Elektron, Elektron AZ91E, Datasheet: 456, http://www.magnesiumelektron.com/data/downloads/DS456AZ9.PDF, September 2011.
5. Aust, K. T., Hanneman, R. E., Niessen, P. and Westbrook, J. H., "Solute induced hardening near grain boundaries in zone refined metals", Acta Metallurgica, Vol. 16, No. 3, 1968, pp. 291-302.
6. Song, G., and Atrens, A. (1999). "Corrosion mechanisms of magnesium alloys", Advanced Engineering Materials, Vol. 1, No. 1, 1999, pp. 11-33.
7. Song, G., Bowles, A, L. and StJohn, D.H., "Corrosion resistance of aged die cast magnesium alloy AZ91D", Materials Science and Engineering A, Vol. 366, 2004, pp.74–86.
8. Metz, S.A. and Flemings, M.C., A fundamental study of hot tearing, AFS Transactions, 1970, Vol. 78, 1970.
9. Gruzleski, J.E., Microstructure development during metal casting, American Foundary Society, Inv., Des Plaines, IL, 2000.
10. Emley, E. F., Principles of magnesium technology, Pergamon Press, New York, 1966.
11. Lee, Y. C., Dahle, A. K. and StJohn, D. H., "The role of solute in grain refinement of magnesium", Metallurgical and Materials Transaction A, Vol. 31A, No. 11, 2000, pp. 2895-2906.
12. StJohn, D. H., Qian, M., Easton, M. A., Cao, P. and Hildebrand, Z., "Grain refinement of magnesium alloys", Metallurgical and Materials Transaction A, Vol. 36, No. 7, 2005, pp. 1669-1679.

13. Jin,Q., Eom, J.P., Lim, S. G., Park, W. W. and You, B.S., "Grain refining mechanism of a carbon addition method in a Mg–Al magnesium alloy", Scripta Materialia, Vol. 49, No. 11, 2003, pp. 1129–1132.
14. Du, J., Hua, M. and Li, W. F., " Effects of Mn addition and addition sequence on carbon inoculation of Mg-3%Al alloy", Advanced Materials Research, Vol. 430-432, 2012, pp. 681-686.
15. Easton, M. A., Schiffl, A., Yao, J. Y. and Kaufmannc, H., "Grain refinement of Mg–Al(–Mn) alloys by SiC additions", Scripta Materialia, Vol. 55, No. 4, 2006, pp. 379–382.
16. Lu, L.,Dahle,A.K. and StJohn, D. H., "Grain refinement efficiency and mechanism of aluminium carbide in Mg–Al alloys", Scripta Materialia, Vol. 53, No. 5, 2005, pp. 517–522.
17. Liu, Y., Liu, X. and Xiufang, B., "Grain refinement of Mg–Al alloys with Al_4C_3–SiC/Al master alloy", Materials Letters, Vol. 58, No. 7-8, 2004, pp. 1282– 1287.
18. Huang,Y., Kainer, K. U. and Hort, N., "Mechanism of grain refinement of Mg–Al alloys by SiC inoculation", Scripta Materialia,Vol. 64, No. 8, 2011, 793–796.
19. Friedrich, H. and Mordike, B. L., Magnesium technology: metallurgy, design data, automotive applications, Springer Berlin Heidelberg Springer, Berlin, Heidelberg, 2006.
20. International magnesium association, http://www.intlmag.org/statistics.html, July 2011.
21. ASM Handbooks Online and ASM international handbook commitee, Properties and selection: nonferrous alloys and special-purpose materials, ASM international, United States, Vol. 2, 1990.
22. Calister, W. D., Material science and engineering an introduction, John Wiley& Sons, 2007.
23. Mordike, B. L. and Ebert, T., "MagnesiumProperties-applications-potential", Materials Science and Engineering A- Structural Materials Properties Microstructure and Processing, Vol. 302, No.1 2001, pp. 37–45
24. Sugimoto, S., "Applications of Magnesium Alloys to Automobile Parts," in Proceedings of the International Magnesium Conference, 1996, pp. 38.
25. Environment Canada, http://www.ec.gc.cac.ca, December 2011.
26. Eliezer, D., Aghion, E. and Froes, F. H., "Magnesium science, technology and applications", Advanced Performance Materials, Vol. 5, 1998, pp. 201-212.

27. Magnesium Electron, http://www.magnesium-elektron.com/markets-applications-summary.asp, July 2011.
28. Polmear, I. J.,"Magnesium alloys and application," Materials Science and Technology, Vol. 10, No.1, 1994, pp. 1-16
29. Zhang, L., Cao, Z.Y., Liu, Y.B., Su, G.H. and Cheng, L.R., "Effect of Al content on the microstructures and mechanical properties of Mg–Al alloys", Materials Science and Engineering A, Vol. 508, No. 1, 2009, pp. 129–133
30. Baker, H., ASM Handbooks Online, & ASM International Staff, ASM handbook: alloy phase diagrams, A S M International, Materials Park, 1992.
31. Matuoka, S., Oguri, M. and Mukai, T., "Mechanical properties and extrudability of Magnesium alloys", in proceedings of the 41st Annual Meeting, JSME Hokuriten Shinetsu Branch, 2004, pp. 215–216.
32. Sajuri, Z. B., Miyashita, Y., Hosokai, Y. and Mutoh, Y. , "Effects of Mn content and texture on fatigue properties of as-cast and extruded AZ61 magnesium alloys", International Journal of Mechanical Sciences, Vol. 48, No. 2, 2006, pp. 198-209.
33. Beer, S., Frommeyer, G. and Schmid, E, in Proceedings of Conference on Magnesium alloys and their applications, Oberursel, DGM, 1992, pp. 317–324.
34. Lu, Y. Z., Wang, Q. D., Zeng, X. Q., Ding, W. J. and Zhu, Y. P., "Effects of silicon on microstructure, fluidity, mechanical properties and fracture behaviour of Mg-6Aln alloy", Material Science and Technology, Vol. 17, No. 2, 2001, pp. 207-214
35. Brooks, C. R., Heat treatment, structure, and properties of nonferrous alloys, American Society for Metals, Metals Park, Ohio, 1982.
36. Reikher, A. and Barkhudarov, M.R., Casting: an analytical approach, Springer, London, 2007.
37. Mechanical Design and Mechanical Eengineering, http://www.mdme.info/MEMmods/MEM30007A/processing/processing.html, July 2011.
38. Umemoto, M., Guo, Z. H. and Tamura, I., " Effect of cooling rate on grain size of ferrite in a carbon steel", Materials Science and Technology, Vol. 3, No. 4, April 1987 , pp. 249-255.
39. Metz, S. A. and Flemings, M. C., "A Fundamental Study of Hot Tearing", AFS Transactions, Vol. 78, 1970, pp.453-460.

40. Lu, L., Dahle, A.K. and StJohn, D.H., "Heterogeneous nucleation of Mg–Al alloys", Scripta Materialia, Vol. 54, No. 12, 2006, pp.2197–2201.
41. Greer,A. L., Bunn,A. M., Tronche, A., Evans, P. V. and Bristow, D. J. "Modelling of inoculation of metallic melts: application to grain refinement of aluminium by Al–Ti–B", Acta Materialia, Vol. 48, No. 11, 2000, pp. 2823-2835
42. Matter, University of Liverpool, http://www.matter.org.uk/matscicdrom/manual/nu.html, August, 2011.
43. Backerud, L., Chai, G. and Tamminen, J., Solidification Characteristics of Aluminium Alloys, Foundry Alloys, AFS/Skanaluminium, Vol. 2, 1990, p. 13
44. Easton, M. and StJohn, D., "Grain Refinement of Aluminum Alloys: Part I. The Nucleant and Solute Paradigms—A Review of the Literature", Metallergical Materials Transactions A, Vol. 30, No. 6, 1999, pp. 1613-1633.
45. Dahle, A. K., Lee, Y.C., Nave, M.D., Schaffer, P.L. and StJohn, D.H., "Development of the as-cast microstructure in magnesium-aluminum alloys", Journal of Light Metals , Vol. 1, No.1, 2001, pp. 61-72.
46. Maxwell, I. and Hellawell, A.,"A simple model for grain refinement during solidification. Acta Metallurgica, Vol. 23, No. 2, 1975, pp. 229-237.
47. Qian, M., StJohn, D. H. and Frost, M. T "Characteristic zirconium-rich coring structures in Mg–Zr alloys",Scripta Materialia, vol. 46, No. 9, 2002, pp. 649-654.
48. Cao, P., Qian, M. and StJohn, D. H., "Effect of iron on grain refinement of high-purity Mg–Al alloys", Scripta Materialia, Vol. 51, No. 2, 2004, pp. 125–129.
49. Kim, Y. M.,Yim, C. D. and You, B.S., "Grain refining mechanism in Mg–Al base alloys with carbon addition", Scripta Materialia, Vol. 52, No.8, 2007, pp.691-694.
50. Qian, M. and Cao, P., "Discussions on grain refinement of magnesium alloys by carbon inoculation", Scripta Materialia, Vol. 57, No. 5, 2004, pp. 415–419.
51. Pan, Y., Liu, X. and Yang, H., "Role of C and Fe in grain refinement of an AZ63B magnesium alloy by Al-C master alloy, Journal of Materials Science Technology, Vol. 21, No. 6, 2005, pp.822-826.

52. Wang, Y., Zeng, X. and Ding, W., "Effect of Al–4Ti–5B master alloy on the grain refinement of AZ31 magnesium alloy", Scripta Materialia, Vol. 54, No. 2, 2006, pp. 269–273.
53. Han, G., Liu, X. and Ding, H., "Grain refinement of AZ31 magnesium alloy by new Al-Ti-C master alloys" Transactions of Nonferrous Metals Society of China, Vol. 19, No. 5, 2009, pp. 1057-1064.
54. Motegi, T., "Grain-refining mechanisms of superheat-treatment of and carbon addition to Mg–Al–Zn alloys", Materials Science & Engineering A, Vol. 413–414, 2005, pp. 408–411.
55. Gunther, R., Hartig, C. and Bormann, R., "Grain refinement of AZ31 by (SiC)P: Theoretical calculation and experiment" , Acta Materialia, Vol. 54, No. 20, 2006, pp. 5591-5597.
56. Ma, Y. T., Zhang, X. G. and Hao, H., "Effect of CaC2 particulates concentration on microstructure and tensile properties of elemental magnesium", Transaction of Nonferrous Metals Society of China, Vol. 18, 2008, pp. 283-287.
57. Shijun, Z., Wenxian, L. and Kun, Y., "The grain refinement processes of magnesium alloys", Foundry (China), Vol. 50, No.7 2001, pp. 373– 375.
58. Motegi, T., Yano, E., Tamura, Y. and Sato, E., "Clarification of grain refining mechanisms of superheat-treated Mg-Al-Zn alloy castings", Materials Science Forum, Vol. 350-351, 2000, pp.191-198.
59. Luo, A., "Heterogeneous nucleation and grain refinement in cast Mg (AZ91) SiCp metal matrix composites", Canadian Metallurgical Quarterly, Vol. 35 No. 10, 1996, pp. 375– 383.
60. Cai,Y., Taplin, D. , Tan, M.J. and Zhou, W., "Nucleation phenomenon in SiC particulate reinforced magnesium composite", Scripta Materialia, Vol. 41, No. 9, 1999, pp. 967– 971.
61. Motegi, T., "Grain-refining mechanisms of superheat-treatment of and carbon addition to Mg–Al–Zn alloys", Materials Science & Engineering A, Vol. 413, 2005, 408-411
62. Fan,T., Shi, Z., Zhang, D., et al., "The interfacial reaction characteristics in SiC/Al composite above liquidus during remelting", Materials Science and Engineering A Structural Materials Properties Microstructure and processing, Vol. 257, No.2, 1998, pp. 281– 286.
63. Schiffl, A. and Easton, M. A., " Influence of SiC particles on the grain refinement of an Mg-Al alloy", Material Science Forum, Vol. 618-619, 2009, pp. 445-448.

64. Yang, M., Pan, F., Cheng, R. and Tang, A., Effect of Mg–10Sr master alloy on grain refinement of AZ31 magnesium alloy, Materials Science and Engineering A, Vol. 491, 2008, pp. 440–445
65. Elsayed, A., Ravindran and Murty, B.S., "Effect of Al-Ti-B based master alloys on grain refinement and hot tearing susceptibility of AZ91E magnesium alloy", Material Science Forum, Vol. 690, 2011, pp.351-354.
66. Aalund, R., "Spark plasma sintering", Thermal Technology LLC, Elgin, III, 2008.
67. Hungrıa,T., Galy, J. and Castro, A., "Spark plasma Sintering as a useful technique to the nanostructuration of piezo-ferroelectric materials", Advanced Engineering Materials, Vol. 11, N0. 8, 2009, pp. 615-631.
68. Tokita, M., "Mechanism of spark plasma sintering", In Proceedings of The International Symposium on Microwave, Plasma and Thermochemcial Processing of Advanced Materials, JWRI, Osaka Universities Japan, 1997, pp. 69–76.
69. Campbell, J., Castings, Elsevier, 2001.
70. Bichler, L., "Phenomenological studies of hot tearing during solidification of magnesium alloys", PhD Thesis, Ryerson University, 2009.
71. Kocherzhinski, Y.and Kulik, O. , Equilibrium phase diagrams and manufacture of synthetic diamonds, Powder Metallurgy and Metal Ceramics, 1996, Vol. 35, No. 7-8, pp. 470-483
72. Bredig, M. A., "The crystal structure of magnesium carbide", Journal of the American Chemical Society, Vol. 65, No.8, 1943, pp 1482–1483.
73. Villers, P. and Calvert, L.D., Pearson's handbook of crystallographic data for intermetallic phases, 2nd ed., ASM International, Materials Park, OH, 1991, p. 5366.
74. Villers, P., Prince, A. and Okamoto, H., Handbook of TernaryPhase Diagrams, ASM International, Materials Park,OH, 1995, p. 2881.

Appendices

Appendix A: Paired *t*-test on mean grain size

Null hypothesis, $H_o = \mu_1 = \mu_2$

Alternative hypothesis, $H_1 = \mu_1 \neq \mu_2$

Assuming, Significance level, α =5%

Decision Criteria (two tail) $|t_{stat}| > t_{crit}$ two tail, Reject H_o

Where μ_1 and μ_2 are the mean grain size of Trial 1 and Trial 2.

Table 27: Paired *t*-test of AZ91E alloy without Al-SiC

Particular	Trial 1	Trial 2
Mean (μm)	230.63	224.35
Variance	3682.66	2864.29
Observations	500.00	500.00
Degree of freedom	499.00	
t Stat	1.78	
t Critical two-tail	1.96	

Table 28: Paired *t*-test of AZ91E + 0.1 wt.% Al-SiC

Particular	Trial 1	Trial 2
Mean (μm)	201.63	195.40
Variance	3646.38	2837.93
Observations	500.00	500.00
Degree of freedom	499.00	
t Stat	1.73	
t Critical two-tail	1.96	

Table 29: Paired *t*-test of AZ91E + 0.2 wt.% Al-SiC

Particular	Trial 1	Trial 2
Mean (μm)	368.03	353.87
Variance	10329.99	6375.97
Observations	282.00	282.00
Degree of freedom	281.00	
t Stat	1.86	
t Critical two-tail	1.97	

Table 30: Paired *t*-test of AZ91E + 0.5 wt.% Al-SiC

Particular	Trial 1	Trial 2
Mean (μm)	321.10	331.67
Variance	6402.48	5012.17
Observations	350.00	350.00
Degree of freedom	349.00	
t Stat	-1.80	
t Critical two-tail	1.97	

Table 31: Paired *t*-test of AZ91E + 1 wt.% Al-SiC

Particular	Trial 1	Trial 2
Mean (μm)	302.85	295.25
Variance	5315.60	3461.88
Observations	400.00	400.00
Degree of freedom	399.00	
t Stat	1.60	
t Critical two-tail	1.97	

According to the five paired t-tests, the absolute t_{stat} values of five t -tests are less than the respective values. Which violate the condition for rejecting null hypothesis, H_o. Which means null hypothesis, H_o cannot be rejected. As a result, it can be concluded that the mean grain size of two repeats (Trial 1 and Trial 2) are same.

Appendix B: Single factor ANOVA on mean grain size

Normality, constant variance and independence assumption for ANOVA were checked and found that the assumption was right. Hypothesises, decision criteria and assumption of single factor ANOVA are mentioned below:

Null hypothesis, H_o: $\mu_1 = \mu_2 = \mu_3 = \mu_4 = \mu_5$

μ_1, μ_2, μ_3, μ_4 and μ_5 are the mean grain size of AZ91E alloy without Al-SiC, with 0.1 wt.% Al-SiC, 0.2 wt.% Al-SiC, 0.5 wt.% Al-SiC and 1 wt.% Al-SiC respectively.

Alternative hypothesis, H_1: At least one mean is different

Assuming, α =5%

Decision Criteria (to tail) $F > F_{crit}$, Reject H_o.

According to Table 32, the F value of between groups (level of grain refiner) is greater than the F_{crit}. Thus, the null hypothesis, H_o can be rejected. As a result it can be concluded that different level of Al-SiC has an effect on mean grain sizes.

Table 32: Single factor ANOVA on mean grain size

Source of Variation	*SS*	*df*	*MS*	*F*	*P-value*	*F crit*
Between Groups	37039.3681	4	9259.84202	160.6793	1.82E-05	5.192168
Within Groups	288.1467	5	57.62934			
Total	37327.5148	9				

Appendix C: Paired *t*-test on mean area percentage of β-phase

Table 33: Paired t -test on mean area percentage of β-phase of base alloy

Particular	Trial 1	Trial 2
Mean	5.42	5.45
Variance	3.9	3.85
Observations	20	20.00
Degree of Freedom	19	
t Stat	-1.43	
t Critical two-tail	2.09	

Table 34: Paired t -test on mean area percentage of β-phase of AZ91E + 0.1 wt.% Al-SiC

Particular	Trial 1	Trial 2
Mean	5.47	5.52
Variance	3.90	3.96
Observations	20.00	20.00
Degree of Freedom	19.00	
t Stat	-1.37	
t Critical two-tail	2.09	

Table 35: Paired t -test on mean area percentage of β-phase of AZ91E + 0.2 wt.% Al-SiC

Particular	Trial 1	Trial 2
Mean	5.28	5.31
Variance	3.90	3.71
Observations	20.00	20.00
Degree of Freedom	19.00	
t Stat	-1.33	
t Critical two-tail	2.09	

Table 36: Paired t -test on mean area percentage of β-phase of AZ91E + 0.5 wt.% Al-SiC

Particular	Trial 1	Trial 2
Mean	6.25	6.30
Variance	4.85	4.97
Observations	20.00	20.00
Degree of Freedom	19.00	
t Stat	-1.41	
t Critical two-tail	2.09	

Table 37: Paired t -test on mean area percentage of β-phase of AZ91E + 1 wt.% Al-SiC

Particular	Trial 1	Trial 2
Mean	6.72	6.55
Variance	10.20	10.13
Observations	20.00	20.00
Degree of Freedom	19.00	
t Stat	2.00	
t Critical two-tail	2.09	

According to the five paired t-tests, the absolute t_{stat} values of five t -tests are less than the respective values. Which violate the condition for rejecting null hypothesis, H_o. Which means null hypothesis, H_o cannot be rejected. As a result, it can be concluded that the mean area percentage of β-phase of two repeats (Trial 1 and Trial 2) were same.

Appendix D: Single factor ANOVA on mean area percentage of β-phase

Normality, constant variance and independence assumption for ANOVA were checked and found that the assumption was right. Hypothesises, decision criteria and assumption of single factor ANOVA are mentioned below:

Null hypothesis, H_o: $\mu_1 = \mu_2 = \mu_3 = \mu_4 = \mu_5$

μ_1, μ_2, μ_3, μ_4 and μ_5 are the mean area percentage of β-phase of AZ91E alloy without Al-SiC, with 0.1 wt.% Al-SiC, 0.2 wt.% Al-SiC, 0.5 wt.% Al-SiC and 1 wt.% Al-SiC respectively.

Alternative hypothesis, H_1: At least one mean is different

Assuming, α =5%

Decision Criteria (to tail) $F > F_{crit}$, Reject H_o.

According to Table 38, the F value of between groups (level of grain refiner) is greater than the F_{crit}. Thus, the null hypothesis H_o can be rejected. As a result it can be concluded that different level of Al-SiC has an effect on mean area percentage of β-phase.

Table 38: Single factor ANOVA on mean area percentage of β-phase

Source of Variation	*SS*	*df*	*MS*	*F*	*P-value*	*F crit*
Between Groups	2.73736	4	0.68434	35.94223	0.000707	5.192168
Within Groups	0.0952	5	0.01904			
Total	2.83256	9				

Appendix E: Paired *t*-test on mean area percentage of porosity

Table 39: Paired *t*-test on mean area percentage of porosity of base alloy

Particular	Trial 1	Trial 2
Mean	2.05	1.84
Variance	2.15	1.28
Observations	20.00	20.00
Degree of freedom	19.00	
t Stat	1.01	
t Critical two-tail	2.09	

Table 40: Paired *t*-test on mean area percentage of porosity of AZ91E + 0.1 wt.% Al-SiC

Particular	Trial 1	Trial 2
Mean	1.89	1.93
Variance	1.73	1.96
Observations	20.00	20.00
Degree of freedom	19.00	
t Stat	-1	
t Critical two-tail	2.09302	

Table 41: Paired *t*-test on mean area percentage of porosity of AZ91E + 0.2 wt.% Al-SiC

Particular	Trial 1	Trial 2
Mean	3.18	3.00
Variance	1.31	1.55
Observations	20.00	20.00
Degree of freedom	19.00	
t Stat	1.81	
t Critical two-tail	2.09	

Table 42: Paired *t*-test on mean area percentage of porosity of AZ91E + 0.5 wt.% Al-SiC

Particular	Trial 1	Trial 2
Mean	3.05	2.92
Variance	0.53	0.64
Observations	20.00	20.00
Degree of freedom	19.00	
t Stat	2.02	
t Critical two-tail	2.09	

Table 43: Paired *t*-test on mean area percentage of porosity of AZ91E + 1 wt.% Al-SiC

Particular	Trial 1	Trial 2
Mean	2.82	2.87
Variance	4.27	4.24
Observations	20.00	20.00
Degree of freedom	19.00	
t Stat	-1.43	
t Critical two-tail	2.09	

According to the five paired *t*-tests, the absolute t_{stat} values of five *t*-tests are less than the respective values. Which violate the condition for rejecting null hypothesis, H_o. Which means null hypothesis, H_o cannot be rejected. As a result, it can be concluded that the mean area percentage of porosity of two repeats (Trial 1 and Trial 2) were same.

Appendix F: Single factor ANOVA on mean area percentage of porosity

Normality, constant variance and independence assumption for ANOVA were checked and found that the assumption was right. Hypothesises, decision criteria and assumption of single factor ANOVA are mentioned below:

Null hypothesis, H_o: $\mu_1 = \mu_2 = \mu_3 = \mu_4 = \mu_5$

μ_1, μ_2, μ_3, μ_4 and μ_5 are the mean area percentage of porosity of AZ91E alloy without Al-SiC, with 0.1 wt.% Al-SiC, 0.2 wt.% Al-SiC, 0.5 wt.% Al-SiC and 1 wt.% Al-SiC respectively.

Alternative hypothesis, H_1: At least one mean is different

Assuming, α =5%

Decision Criteria (to tail) $F > F_{crit}$, Reject H_o.

According to Table 44, the F value of between groups (level of grain refiner) is greater than the F_{crit}. Thus, the null hypothesis H_o can be rejected. As a result it can be concluded that different level of Al-SiC has an effect on mean area percentage of porosity.

Table 44: Single factor ANOVA on mean area percentage of porosity

Source of Variation	*SS*	*df*	*MS*	*F*	*P-value*	*F crit*
Between Groups	2.38449	4	0.596123	25.29963	0.001627	5.192168
Within Groups	0.117813	5	0.023563			
Total	2.502303	9				